UNIVERSITY OF CALIFORNIA
RIVERSIDE

Biomimetic Designs for Impact-Resistant Composite Materials Inspired by the Heavily Armored Mantis Shrimp

A Dissertation submitted in partial satisfaction
of the requirements for the degree of

Doctor of Philosophy

in

Materials Science and Engineering

by

Nicholas Andrew Yaraghi

June 2018

Dissertation Committee:
Prof. David Kisailus, Chairperson
Prof. Pablo Zavattieri
Prof. Suveen Mathaudhu

The Dissertation of Nicholas Andrew Yaraghi is approved:

Committee Chairperson

University of California, Riverside

Acknowledgements

This research was conducted with Government support under and awarded by DoD, Air Force Office of Scientific Research, National Defense Science and Engineering Graduate (NDSEG) Fellowship, 32 CFR 168a. I would also like to acknowledge financial support from the Air Force Office of Scientific Research, Multi-University Research Initiative (AFOSR-FA9550-15-1-0009), AFOSR Grant FA9550-12-1-0245, AFOSR DURIP Grant W911NF-16-1-0208 for the MIRA SEM, and AFOSR DURIP Grant FA9550-10-1-0322 for the nanoindenter. Work contained in this document has appeared in previously published articles, featured in *Advanced Materials* (1) and *Annual Review of Physical Chemistry* (2).

I would like to first thank my advisor, Professor David Kisailus, for accepting me into his research group and giving me the opportunity to work in his lab. I am thankful to have had the chance to work on the many exciting and impactful projects related to the mantis shrimp. During my time at UCR, Dr. Kisailus gave me countless opportunities to perform research at world-class facilities, attend domestic and international conferences, and interact with a wide range of academic and industrial leaders, and for that, I am incredibly grateful. I would also like to thank Dr. Kisailus for constantly pushing me to take on new challenges, break out of my comfort zone, and realize my full potential as a researcher. Although, at times, I felt stressed and frustrated, I would not have accomplished all that I have today were it not for his constant motivation and support.

I want to next thank my many lab-mates over the years, specifically Steven Herrera, Chris Salinas, Parawee Pumwongpitak, Jesus Rivera, Thomas Dugger, Ramya Mohan, and

Luz Cruz. Grad school would not have been possible without you and I am so thankful to have had such an awesome support team over the years. Your friendship means more to me than you will know.

To all my collaborators and teachers through the years, especially Lessa Grunenfelder, Pablo Zavattieri, Richard Wuhrer, Krassimir Bozhilov, Mathias Rommelfanger, Thomas Yong Han, and Suveen Mathaudhu, I have learned so much from each of you and I sincerely thank you for all your guidance and mentorship. To my high school chemistry teacher, Spencer Lake, you helped initiate my curiosity and passion for science and I will be forever grateful.

Finally, I want to thank my family for their constant love and support. Mom, were it not for you encouraging me to take the trip out to California to visit UCR in the first place, I wouldn't be where I am today. Thank you. Mom, Dad, Alex, and Jenn, I know that the last five years, especially with me living on the other side of the country, have not been easy, but I appreciate your patience and look forward to the very exciting times ahead!

ABSTRACT OF THE DISSERTATION

Biomimetic Designs for Impact-Resistant Composite Materials
Inspired by the Heavily Armored Mantis Shrimp

By

Nicholas Andrew Yaraghi

Doctor of Philosophy, Graduate Program in Materials Science and Engineering
University of California, Riverside, June 2018
Prof. David Kisailus, Chairperson

Biologically mineralized composites offer inspiration for the design of next generation structural materials due to their environmentally friendly synthesis, low density, and combination of high stiffness and toughness, currently unmatched by engineering technologies. Such properties are the result of hierarchical structuring and well-defined compositional and mechanical gradients afforded by the organism's ability to control the self-assembly and nucleation and growth of organic and inorganic materials, respectively. Here, we investigate structure-mechanical property relationships of two incredibly damage-tolerant and impact-resistant bio-composite materials: the mantis shrimp dactyl club and telson, which resist catastrophic failure from repeated high-energy impacts and cavitation from one of the fastest striking events observed in nature. We identify numerous multi-length scale architectural designs that play key roles in imparting stiffness, compliance as well as delocalizing stress and enhancing toughness. These design cues are

then translated and implemented into biomimetic composite materials that are fabricated using traditional fiber-reinforced composites processing as well as advanced direct ink write additive manufacturing. The ability for these biomimetic composites to demonstrate enhanced damage-tolerance over traditional designs is then assessed through mechanical testing. Such findings may prove useful for the on-going design and fabrication of lightweight structural materials possessing improved damage-tolerance.

Table of Contents

List of Figures

Chapter 1: Introduction

The design and fabrication of materials possessing desired mechanical, optical, thermal, and electrical properties has long been a critical goal in the field of materials science and engineering (15; 16). Recently, there has been a growing demand in a wide range of industries (i.e., aerospace, transportation, infrastructure, defense) for new classes of high performance structural materials that are not only durable, possessing strength and toughness (damage-tolerance), but also lightweight (15-17). In the transportation sector, this demand has largely been brought on by an accelerating impetus to combat the adverse effects of global warming, through the light-weighting of vehicles to improve fuel economy and reduce CO_2 emissions (18; 19). In the military and defense sectors, reduced weight of personal and vehicle armor systems translates to increased mobility and decreased fatigue on the wearer, leading to improved performance (20; 21).

Granted improvements are made to the light-weighting of these structural components, the materials still need to be mechanically robust enough to fulfill their function. However, designing and manufacturing materials that are concurrently stiff, tough, and lightweight has been a long-standing challenge in the field of materials science and engineering. It is important to make the distinction: strength refers to the maximum amount of stress a material can withstand before failing or plastically deforming whereas toughness is the measure of the total amount of energy a material can absorb before failing. Traditionally, the properties of strength and toughness are mutually exclusive, meaning materials either have high strength or high toughness, but not both (3). For example, ceramic materials conventionally possess high compressive strength, yet lack the ductility

to resist fracture under tensile and bending loads. This is a recurring issue in some commercially available personal armors which feature ceramic plates that may crack if dropped and fail catastrophically only after a few impacts from projectiles, rendering them useless, and requiring replacement. On the contrary, many traditional polymer fibers have high extensibility giving them sufficient toughness but lack high strength. For example, armor vests featuring Kevlar or high-density polyethylene fibers are effective at stopping low caliber bullets from handguns (i.e., NIJ complaint Type IIA – IIIA), but cannot effectively provide protection against higher energy rounds, such as those from rifles (22). Modern structural engineering materials such as steels and other metal alloys have made some progress in overcoming the strength-toughness barriers; however, their higher density can limit their use in lightweight applications. An Ashby diagram showing typical

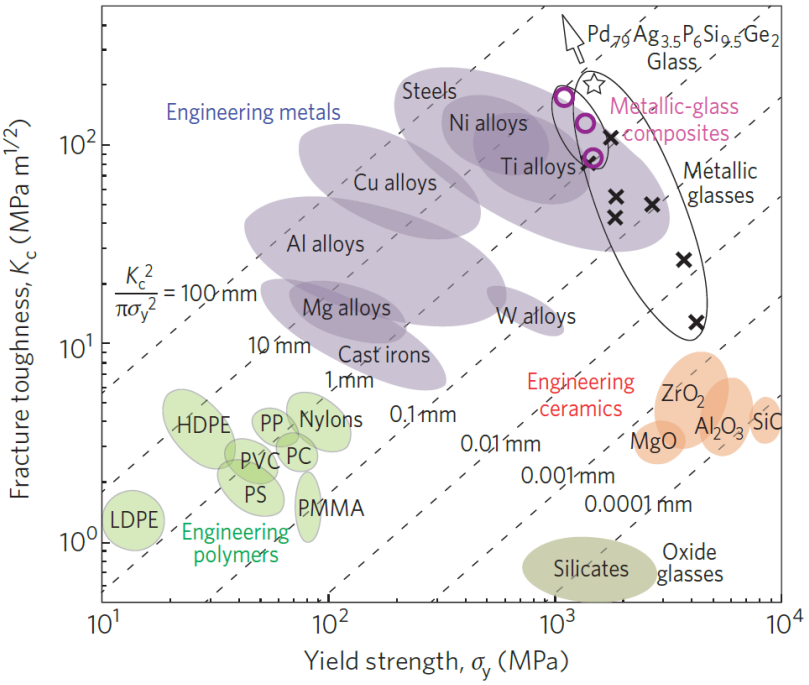

Figure 1.1. Ashby diagram showing fracture toughness-yield strength relationships for various engineering materials. Figure adapted from reference (3).

strength-toughness relationships for a variety of polymer, ceramic, and metal engineering materials is shown in Figure 1.1.

Composites, which combine multiple materials such as high strength fibers and tough polymer resins, are an attractive candidate for producing lightweight, strong, and tough components. Fiber reinforced composites, specifically those featuring carbon fiber, are finding more and more use in high performance structural applications such as in aircraft (e.g., Boeing 787), wind turbine blades, electric vehicles, and sporting equipment, due to their high strength-weight ratios (specific strength). Boeing's 787 Dreamliner, which entered commercial service in 2011, was the first airliner to feature an airframe constructed primarily of composite materials (50% by weight) (4). The replacement of metals such as aluminum with carbon laminate and carbon sandwich composite materials resulted in a lighter aircraft with a 20 percent improvement in fuel efficiency as compared to the previous Boeing 767 (Figure 1.2 A) (4). Carbon fiber reinforced polymer (CFRP) materials which were also conventionally limited to low-volume high performance supercars, like the McLaren F1 and Koenigsegg Agera, and competitive motorsport vehicles (e.g., Formula One cars), are now being implemented into consumer full-production vehicles like the BMW i3 (Figure 1.2 B) (23). SpaceX's 40-foot wide fuel tank for its Interplanetary Transport System (ITS), which will hold cryogenic liquid oxygen propellant and operate under extreme conditions of temperature and pressure, was constructed using CFRP material (Figure 1.2 C) (6).

Ceramic matrix composites, which feature ceramic fibers, such as silicon carbide, embedded in a ceramic matrix, are also being implemented as lightweight structural

materials for applications that demand extreme thermal resistance in addition to strength and fracture toughness. For example, the brake discs used in Formula One cars, which experience service temperatures up to 1000 °C and extreme abrasive stresses, feature carbon/carbon composite materials that are composed of carbon fibers embedded in a graphite matrix (Figure 1.2 D) (24). Concurrently, development of new turbofan engines such as the General Electric GE9X, which will power the Boeing 777X, will feature carbon- and glass-fiber composite fan blades as well as a composite fan case to reduce weight and improve fuel efficiency (8). Ceramic matrix composite materials will also be used in nozzle and shroud components of the engine (8).

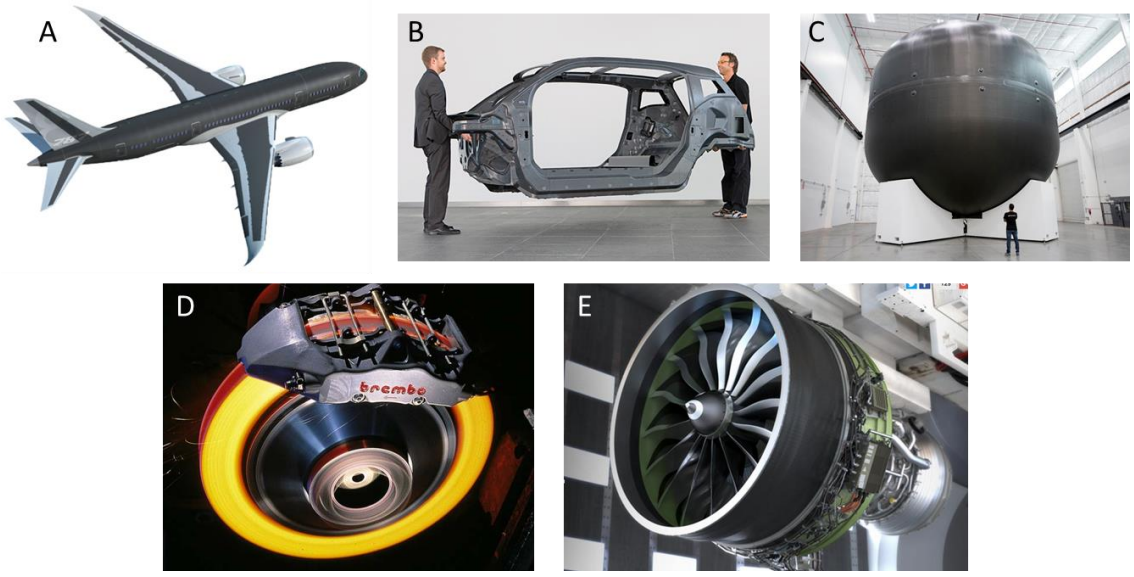

Figure 1.2. Examples of composite materials used in current and future aerospace and automotive structures. (A) Schematic of Boeing 787 Dreamliner highlighting use of CRFP laminates in the fuselage, wings, and tail. (B) BMW i3 passenger cell composed of CRFP. (C) CFRP liquid oxygen fuel tank for SpaceX's ITS rocket. (D) Formula One brake disc featuring carbon/carbon composite. (E) General Electric GE9X turbofan aircraft engine featuring CFRP fan blades and case as well as ceramic matrix composite nozzles and shrouds. Panel *A* adapted from Reference (4); panel *B* adapted from Reference (5); panel *C* adapted from Reference (6); panel *D* adapted from Reference (7); panel *E* adapted from Reference (8).

The composite materials market has grown significantly and expects continued growth into the next few decades across numerous industries, such as transportation, marine, wind energy, aerospace/defense, and consumer goods. According to a 2014 market review by the Carbon Composites e.V., which is an association of companies and research institutes in Germany, Austria and Switzerland focusing on fiber reinforced composites, global consumption of carbon fiber grew by a total of 47.6 percent from 2008 to 2013 (Figure 1.3), with an annual growth rate of approximately 8.1 percent (9). In addition, a long-term annual growth rate of approximately 9 percent can be expected (9). Nearly all carbon fiber manufactured is used in combination with a matrix material to form composites and thus the expected growth trends for carbon composites are similar to those of carbon fiber (9). A report by McKinsey & Company published in 2012 suggests that, over the next two decades, the market for high-strength steel, aluminum, and carbon fiber, replacing traditional steel within the automotive, aviation, and wind industries will reach €300 billion , with carbon fiber showing the highest growth at almost 20 percent per year (25). While aerospace and wind energy currently dominate the use of composites, the automotive industry is forecasted to show the largest growth, due to increased global pressure on original equipment manufacturers to meet CO_2 emissions targets in order to avoid harsh financial penalties (25). The percent composition of lightweight materials (i.e., glass fiber, carbon fiber, plastics, magnesium, aluminum, and high-strength steel) in structures, which is currently dominated by aviation at 80 percent, will see a massive increase in the automotive sector, from 30 percent to 70 percent by 2030 (25).

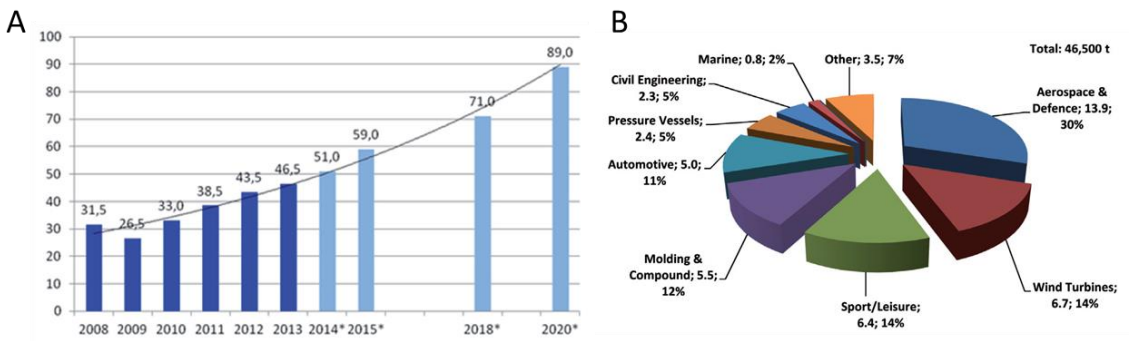

Figure 1.3. (A) Global demand for carbon fiber in thousand metric tons (*estimate). (B) Global carbon fiber demand by industry in thousand metric tons for 2013. Panels *A*, *B* reproduced from Reference (9).

Despite the projected increase in future use of composites, the high cost of these materials currently limits their widespread use. Although carbon fiber is 50 percent lighter than traditional steel and 16 percent lighter than aluminum, part costs are approximately 5 times higher than steel and 4 times higher than aluminum (25). Large-scale use of carbon composites, especially in the automotive sector, will depend on the industry's ability to reduce the cost of these materials (9). These prohibitive costs have been attributed to demanding process by which the constituent materials, (i.e., carbon fiber), are manufactured. More broadly, conventional processes for synthesizing a wide range of structural engineering materials like steels, concretes, and composites exhibit numerous drawbacks. They are often labor-intensive, require conditions of high temperature and/or pressure (which can be highly energy demanding and costly), and often rely upon the use of harsh or environmentally unfriendly (acidic, basic, toxic) chemicals and components (15; 16). For example, the production of carbon fiber involves the initial wet spinning of polyacrylonitrile dissolved in a polar solvent such as sodium thiocyanate, nitric acid, or

dimethylacetamide, which are toxic/corrosive, followed by stabilization in air at 200-300°C for 30-120 minutes, carbonization at 1000-3000°C, and finally surface treatment using a variety of additional liquid and gaseous chemicals (26; 27). Growing global environmental, economic, and energy-related concerns will demand new manufacturing techniques and synthetic processing routes that are sustainable, energy-efficient, and low-cost.

When thinking about sustainable and energy-efficient means of producing materials, there is no better source of inspiration than the natural world. Nature provides an excellent inspiration for the design and fabrication of next-generation structural as well as multifunctional materials because, for hundreds of millions of years, nature has evolved efficient strategies for synthesizing a diverse range of materials. These materials exhibit exceptional mechanical, thermal, and optical properties while also incorporating multifunctionality, such as adapting, sensing, and self-repair (28-32). Organisms rely upon these structures for a diverse range of functions such as structural support, feeding, and defense against predators. Such diversity in material properties and functions is remarkable, considering the limited set of constituent elements and building-block materials nature has at its disposal.

Biological materials, which typically exist as composite structures, can be divided into nonmineralized (typically soft) and mineralized (hard) tissues. Both contain organic components, typically soft biopolymers such as proteins (e.g., collagen, keratin, and elastin) or polysaccharides including chitin, cellulose, hemicellulose, and lignin (29-32). Whereas nonmineralized tissues typically derive their strength from intermolecular

bonding, such as hydrogen bonding or covalent cross-linking of polymer chains, biomineralized tissues additionally incorporate stiff inorganic crystals to achieve their strength. The most common inorganic components, which are of either amorphous or crystalline form, include calcium carbonate, calcium phosphate, silicon dioxide, and even iron oxide (30-32).

Although the soft biopolymer and stiff biologically mineralized ceramic constituents are not inherently strong or tough, respectively, the resultant biological composites are both (29-32). This can be attributed to the precise manner in which they are hierarchically assembled from the bottom up, yielding complex yet well-defined structures at the nano-, micro-, and macro-scales. An Ashby diagram showing this unconventional combination of properties is shown below in Figure 1.4.

A notable example, which has been the gold standard in the biological materials literature, is nacre, a bio-composite structure found within the inner layer of many mollusk shells (Figure 1.5 A) (33-43). Nacre is composed of 95% calcium carbonate, in the form of aragonite, and 5% organic material (β-chitin polysaccharide, fibroin silk-like proteins, other acidic proteins) by volume, yet achieves a work of fracture three orders of magnitude higher than that of pure aragonite (44). This enhancement in toughness is attributed to its well-ordered lamellar micro- and nano-structure featuring polygonal aragonite tablets (500 nm thick and 5 – 15 μm in diameter) stacked and separated by thin (20 – 30 nm) sheets of organic material, forming a brick-and-mortar arrangement. The alternating hard/soft interfaces between ceramic tablets and organic matrix allow for stable crack propagation along a tortuous path (extrinsic toughening in the form of crack deflection) thereby

increasing the work of fracture. Viscoplastic deformation of the interlamellar organic sheets also allow for tablet sliding, providing some ductility. Additional strengthening

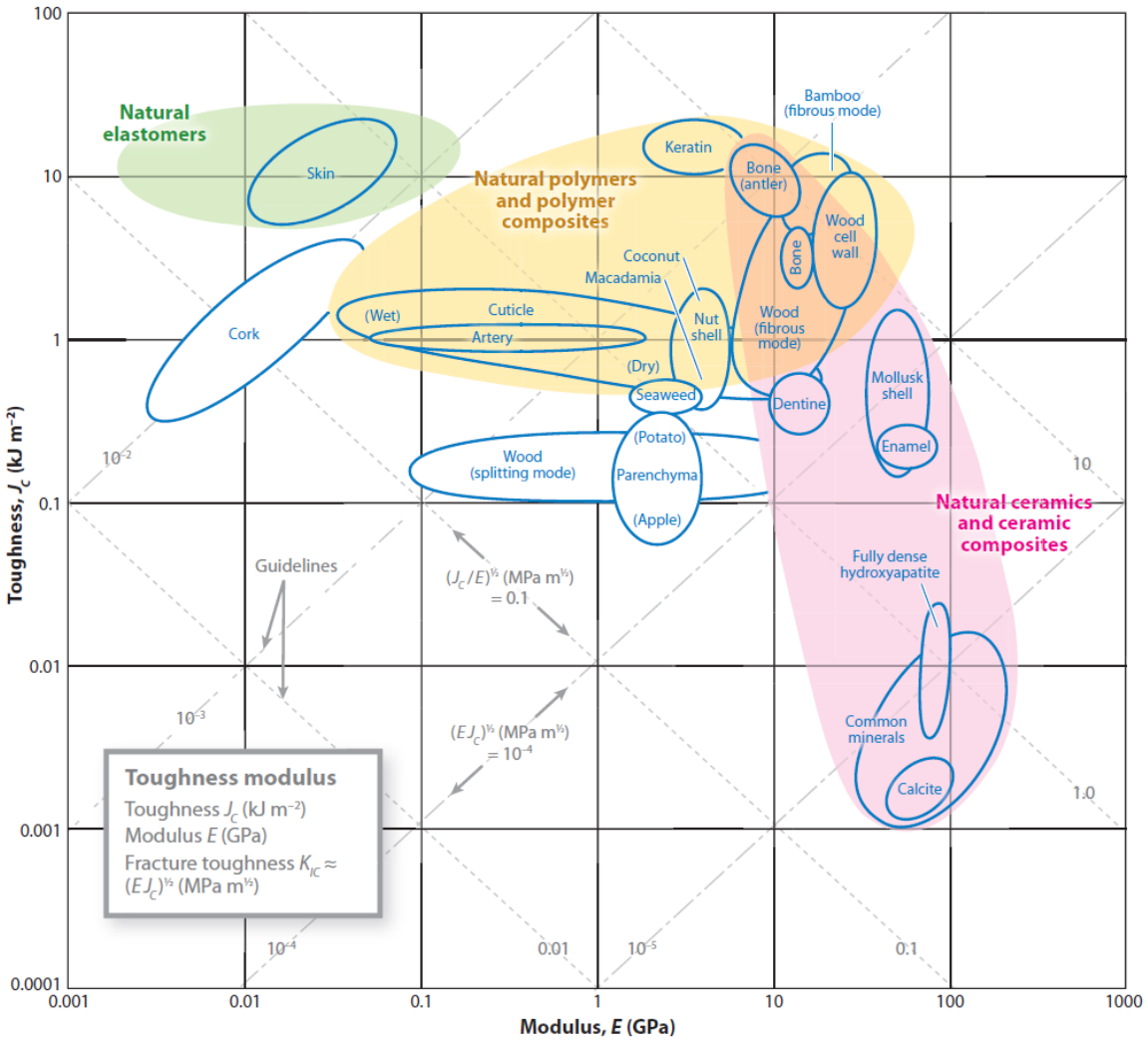

Figure 1.4. Ashby diagram comparing modulus and toughness for various natural materials. Image reproduced from Reference (10).

mechanisms attributed to hierarchical structuring include the resistance to tablet sliding under tensile loading due to mineral nanoasperities on the surface of tablets, mineral bridging between tablet layers, and wavy tablet morphology, providing an interlocking and

strain hardening effect (35-39; 45). It is thus evident that the precise hierarchical structuring of composites can drastically improve their mechanical performance.

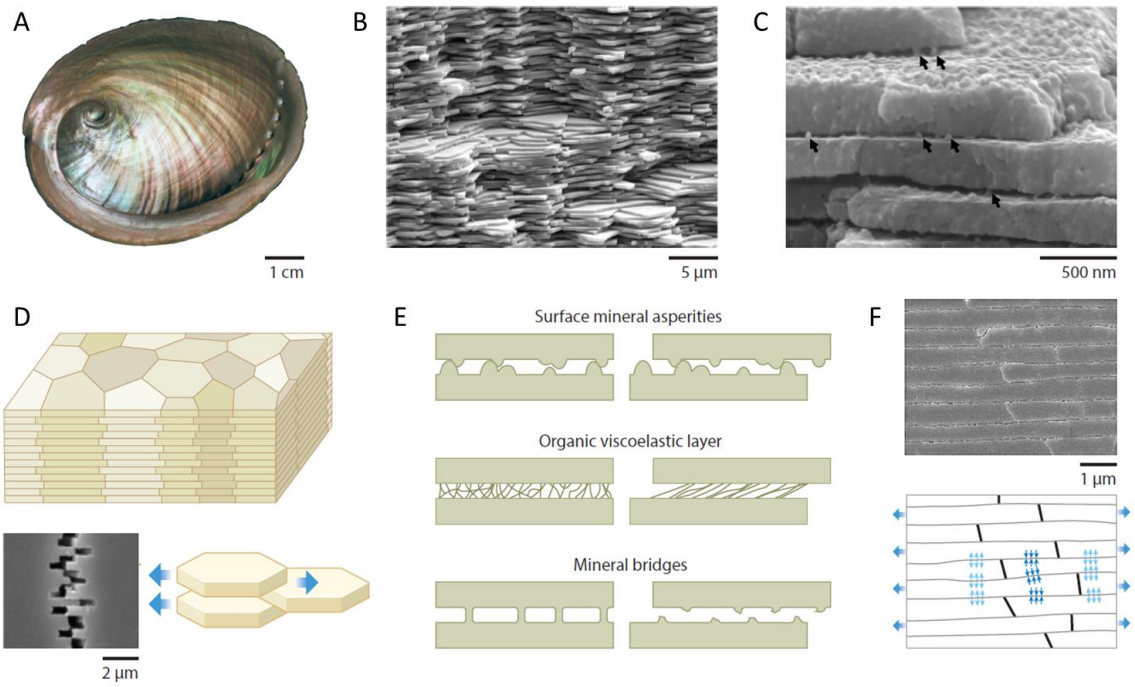

Figure 1.5. Ultrastructure and toughening mechanisms in nacre. (A) Overview of inner iridescent region of shell from the smooth Australian abalone (*Haliotis laevigata*). (B) Scanning electron micrograph (SEM) of fractured cross section of the nacreous layer from *H. laevigata*. (C) High-magnification SEM micrograph showing mineral nanoasperities on the surface of tablets and mineral bridging between tablet layers after deproteination treatment. (D) Schematic of the brick-and-mortar architecture (*top*) and SEM micrograph showing tablet pull-out under tensile loading (*bottom*). (E) Schematic showing different modes of tablet sliding and pull-out. (F) SEM micrograph showing tablet waviness and dovetail-like structure providing resistance to pull-out. Figure reproduced from Reference (2).

While the mechanical properties of biological composites are not inherently impressive as compared to engineering materials, one must consider the limited selection of available building block materials at nature's disposal. Biological structures must be assembled using the lightweight elements available in the surrounding environment (i.e.,

H, C, N, O, F, Na, Mg, Si, P, S, Ca, Fe). On the contrary, today's scientists and engineers have a wide range of synthetic material components (e.g., metal alloys, synthetic polymers) that possess high strength or high toughness. One of the unique aspects of biology is that nature does not have access to and rely upon high temperature/high pressure processing techniques to fabricate its materials. Unlike conventional synthetic materials processing, nature synthesizes its materials under mild conditions: ambient temperature, ambient pressure, and near-neutral pH. Thus, beyond learning from nature about the unique structural designs that yield exceptional mechanical, thermal, or optical properties, much can be learned from studying how nature fabricates its materials. Understanding the parameters that control biological self-assembly of biopolymers and mineralization of inorganic biogenic crystals, with specific phase, crystallinity, orientation, and morphology, can provide new insights into low-energy and efficient processing of materials. For example, in biomineralized tissues, it has become increasingly apparent that biopolymers (proteins, peptides, and polysaccharides) containing specific chemical functionalities actively control the nucleation and growth of biominerals (46-61). The result of this directed synthesis is precise control of inorganic phase, crystallinity, morphology, orientation, and gradients, contributing to the end-material properties.

A perfect example of this control can be found, again, in the nacre system. The self-assembly of the organic matrix and the role of organic macromolecules in controlling the nucleation and growth of aragonitic crystals, has attracted much interest from the biomineralization community (62-65). Although organic polysaccharides and proteins make up only 5% of nacre by volume, these biopolymers play a critical role in the

formation of the well-ordered and crystallographically aligned mineral phase. Nacre growth occurs by the alternate growth and arresting of mineral tablet layers controlled by

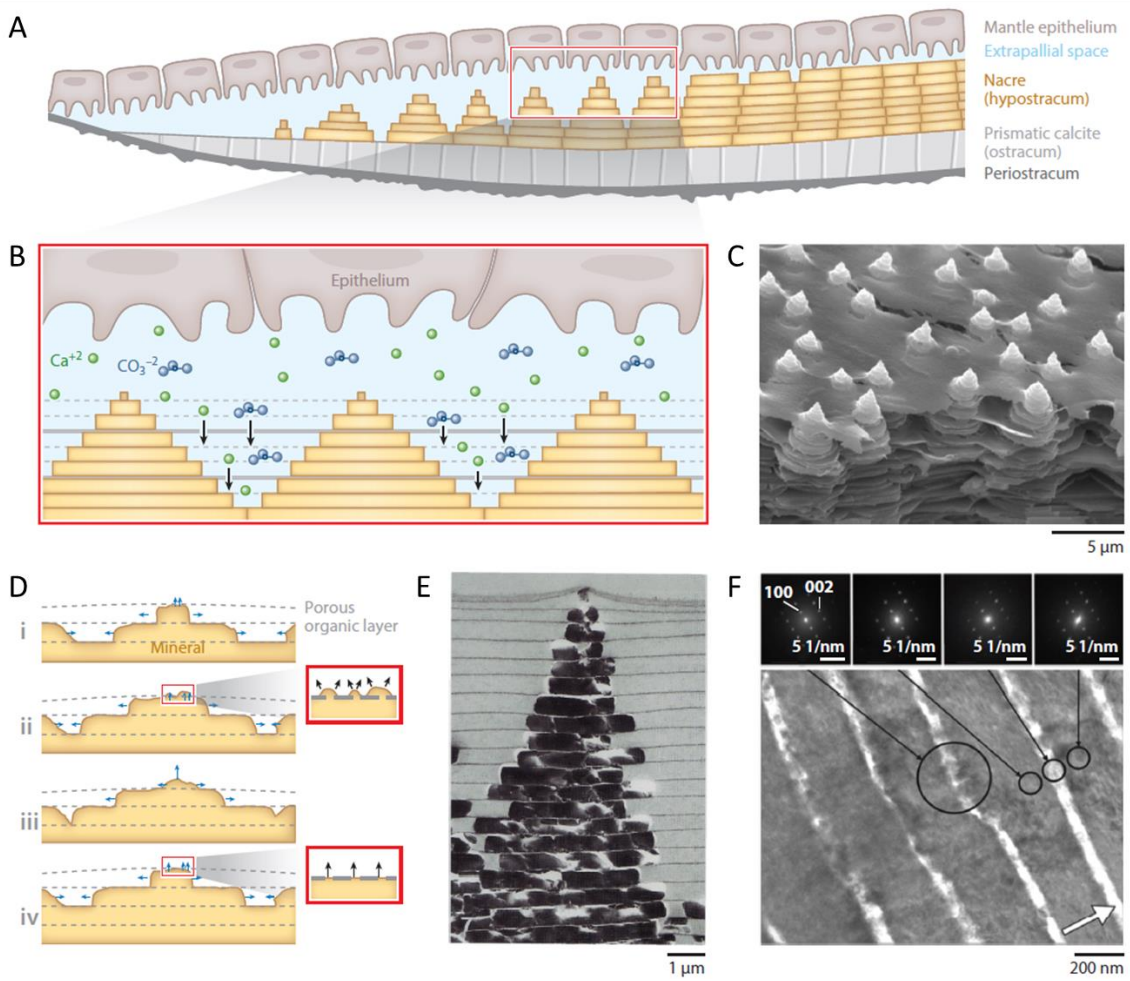

Figure 1.6. Nacre formation mechanism. (A) Schematic of cross section through growing shell of *Haliotis laevigata*. (B) Schematic showing development of nacreous tiles through repeated arrest and growth of $CaCO_3$. (C) Scanning electron microscopy micrograph showing a Christmas-tree pattern of growing nacre tablets. (D) Schematic showing various stages of tablet growth: (*i*) deposition of organic layer arresting tablet growth in the *c* direction; (*ii*) continued lateral growth in the *a*- and *b*-directions with small amount of *c* direction growth into next layer through pores of organic layer; (*iii*) formation of new tablet in adjacent layer with growth in all directions; and (*iv*) *c*-axis growth arrested with deposition of new organic layer. Processes *i*–*iv* are repeated. (E) Transmission electron microscopy (TEM) micrograph showing nacre tablet growth. (F) TEM micrograph of nacreous layers and selected area electron diffraction patterns confirming crystallographic continuity across tablet layers through mineral bridging. Figure reproduced from Reference (2).

the secretion and deposition of interlamellar organic matrix material (Figure 1.6). Heinemann et al. (66) and Nudelman (67) recently provided reviews on the mechanisms of crystal nucleation and growth in nacre. Initially, an organic layer is secreted. Calcium carbonate then nucleates on the surface of this layer and grows in all directions, with the fastest growth along the *c*-axis. Thereafter, a second organic layer is secreted, which arrests mineral growth in the *c*-direction and allows growth to continue in the *a*- and *b*-directions. However, small pores within the organic layer allow the mineral to continue growing in the *c*-direction, through the membrane, and seed the growth of new tablets in the next layer. This process repeats itself, resulting in the characteristic Christmas tree pattern shown in Figure 1.6. The continuation of mineral across tablet layers accounts for the observed mineral bridges that also display crystallographic continuity (Figure 1.6 F). Although the specific mechanism of nucleation and growth of mineral is still under debate, it is generally accepted that acidic proteins containing residues with certain chemical functionalities (e.g., carboxylates, sulfates) adsorbed to the chitinous scaffold are responsible for initiating nucleation and arresting growth of the aragonite tablets (67).

By studying and understanding both the synthesis–structure and structure–property relationships of biological materials, we can gain insight useful for the efficient fabrication of next-generation high-performance structural and multifunctional materials. These ideas are at the heart of biomimetics. Biomimetic materials engineering, which differs from bio-inspired or biomediated materials engineering, focuses on recreating or mimicking the structural design of biological materials or the process by which biological materials are synthesized (2; 68-70). Although it is closely related, we define bio-inspired materials

engineering as taking design cues from natural fabrication processes and applying them to other synthetic systems. An example of bio-inspired processing would be the synthesis of nanostructured oxides that utilize synthetic control parameters exhibited by biological systems (i.e., pH, precursor concentration, organic ligands, etc.) to yield materials with controlled size, shape, and phase. Bio- mediated engineering focuses on implementing or incorporating the inherent biological elements into some other system to take advantage of the properties of that biological material. An example would be utilizing enzymes as a platform to synthesize semiconducting oxide materials (71-74). The field of biomimetics with respect to mimicking the structure of natural materials is vast and has been productive in the past decade (2; 53; 68-70; 75-80). The advent of pre-existing as well as newly developed manufacturing processes, such as advanced additive manufacturing/3D-printing, freeze-casting, layer-by-layer deposition, thermal-spray processing, cholesteric self-assembly, fiber-reinforced composites processing, and magnetically-assisted slip casting, have now made it possible to produce composite materials that closely mimic the complex microstructures observed in the natural world (76; 81-90). Nacre-mimetic structures produced by freeze-casting, for example, achieve similar hierarchical structural features, such as the brick-and-mortar microarchitecture, nano-asperities on the surface of tablets, and mineral bridges, to provide enhanced toughening (85; 91). Moreover, these synthetic structures have demonstrated the potential to exceed the strength and fracture toughness of the natural system (*Haliotis rufescens*), by incorporating materials like alumina, hydroxyapatite, titanium, and silica instead of the biogenic aragonite (85; 91).

Nature provides an exorbitant number of model systems of study for bio-inspiration. When thinking about designs for damage-tolerant structural materials, one class of natural materials that serve as a perfect model for inspiration are those that undergo high-energy impact events. Examples include the beaks of birds, such as the woodpecker, which impact on trees with high accelerations/decelerations, the hooves of equidae, and the antlers and horns of bovids, such as the bighorn sheep, which can withstand repeated impacts up to 3400 N with conspecifics during agnostic interactions (92-96).

One model system of interest when considering damage-tolerant and impact-resistant materials lies in the cuticular (exoskeletal) structures of the stomatopod (Figure 1.7), more colloquially referred to as the mantis shrimp, which is an aggressive marine crustacean. The hammer-like raptorial appendage (dactyl club) and shield-like telson of the species, *Odontodactylus scyllarus*, are two examples of highly impact-resistant and damage-tolerant biological composites, which are used for hunting prey as well as defense against predators and conspecifics, respectively (11; 12; 97-99). The mantis shrimp uses its dactyl clubs to smash through mollusk shells, crab exoskeletons, and other tough mineralized structures of its prey with tremendous force and speed (11; 100). Achieving accelerations over 10,000 *g* and reaching speeds of 23 m/s from rest, the dactyl strike is recognized as one of the fastest and most powerful impacting events observed in nature (11; 100). The club is capable of delivering and subsequently enduring repetitive impact forces up to 1500 N and cavitation stresses without catastrophically failing, demonstrating its utility as an exceptionally damage-tolerant natural material. In fact, several of the shell

structures that the dactyl club breaks through feature the nacreous layers, suggesting that the dactyl contains an even more robust design.

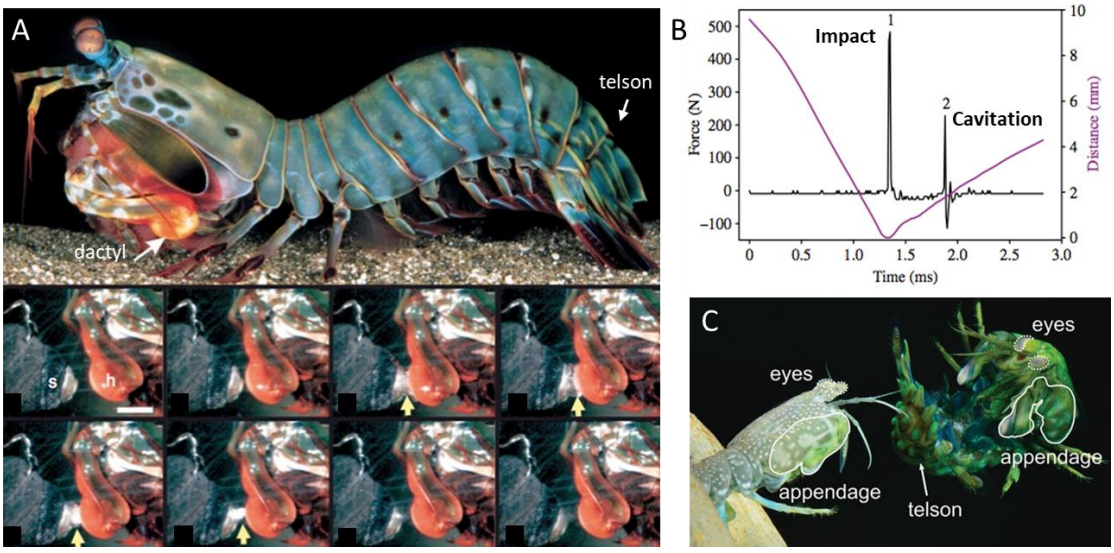

Figure 1.7. Overview of the mantis shrimp dactyl club & telson. (A) The peacock mantis shrimp, *O. scyllarus*, (top) and slow motion video frames of a striking event highlighting cavitation formation at the club surface (bottom). (B) Impact force measurements showing impulses from direct impact and cavitation. (C) Ritualized fighting between two smashing-type mantis shrimp and coiling behavior, demonstrating use of the telson as a shield. Panels *A* and *B* reproduced from Reference (11). Panel *C* reproduced from Reference (12).

In conjunction with the dactyl, *O. scyllarus* also relies on a shield-like segment of exoskeletal armor called the telson, which is located at the terminal segment of its abdomen and is used as a barrier to defend its burrow from predators as well as protect itself during ritualized fighting with other mantis shrimp (12; 99). The telson can withstand direct and repeated dactyl strikes from conspecifics without catastrophically failing, suggesting a similarly impressive damage-tolerant design. Moreover, an interesting evolutionary story exists with respect to the role selective pressures such as environment, selection of habitat

and competition has played on the development of agnostic behavior in stomatopods and the evolution of telson morphologies and structures to necessitate impact-resistance.

Structure-mechanical property relationships have been investigated for a number of impact-resistant biological materials; however, unlike the dactyl club and telson, many of these materials are not subjected to thousands of high strain rate impacts while resisting cavitation. The structure-function relationships have not yet been fully realized for the stomatopod telson and the dactyl club. Also, the mechanical properties rely on ultrastructural features such as mineral crystallinity, phase and orientation, which are controlled during the mineralization process. Studies have examined the role of structural organics and matrix proteins in controlling crystal nucleation and growth in biomineralized tissues (48; 51; 101). Yet, a critical void exists to explain cohabitation of amorphous and oriented crystalline mineral phases within a structure. Investigating the mineralization process in the dactyl club would yield clues towards this process, which may provide insight to the design and synthesis of engineering ceramic-based composites that exhibit enhanced damage-tolerance and resistance to impact. Moreover, little work has been done to fully construct, characterize, and realize the capabilities of biomimetic composite materials inspired by the mantis shrimp and telson for impact-resistance and damage-tolerance.

The goals of this dissertation are thus to present a study of the (1) structure-mechanical property relationships of the stiff and hard outer impact region and impact surface of the mantis shrimp dactyl club, (2) structure-mechanical property relationships and convergent evolutionary designs of the mantis shrimp telson, (3) synthesis-structure

mechanisms (structural development) of the mantis shrimp dactyl club, and (4) biomimetic efforts to fabricate composite materials inspired by the mantis shrimp dactyl club and telson, and evaluate their mechanical performance in response to impact. Investigation of the ultrastructural features, mechanical properties, and mineralization of these materials will provide insight to the controlled synthesis and assembly of organic and inorganic constituents and the effect of multi-length-scale structural features on enhancing strength and toughness. These design guidelines will provide insights to the on-going fabrication of biomimetic composite materials that are strong, tough, lightweight, and efficiently produced.

Chapter 2: Structure-mechanical property relationships of the stomatopod dactyl exocuticle (impact region)

2.1 Background

In 1982, Currey, Nash, and Bonfield conducted the first systematic study of the design of the stomatopod raptorial appendage, with the goal of understanding the features that make it capable of dealing repeated lethal blows while resisting catastrophic failure (102). Using a combination of microhardness measurements, scanning electron microscopy (SEM), and energy dispersive spectroscopy (EDS), the authors uncovered details concerning the mechanical, structural, and compositional features. EDS analysis revealed a heavily calcified cuticle, with increasing P:Ca ratio from the interior of the dactyl towards the outer surface, indicating the replacement of calcium carbonate for calcium phosphate within the exterior (102). Microhardness measurements correlated nearly linearly with the elemental P:Ca trends, showing an increasing hardness moving towards the cuticle surface (102). The helicoidal fibrous architecture of the dactyl, consistent with the microstructures of most arthropod cuticles, was also revealed by SEM analysis of the fractured cross-section (102). More recently, Weaver et al. identified the dactyl club as a multi-regional composite material containing an organic matrix composed of alpha-chitin fibers mineralized by amorphous and crystalline forms of biomineral (13; 14). Mechanical analysis by nanoindentation mapping revealed three distinct domains: a stiff and hard outermost region of the club, which was termed the impact surface, 50 – 70 μm thick with an elastic modulus of 65 – 70 GPa; a bulk exocuticle (impact region), ~500

μm thick with a graded elastic modulus of 60 – 30 GPa, decreasing from the impact surface to the club interior; and a bulk endocuticle (periodic region) with an elastic modulus oscillating between 10 and 25 GPa (13; 14). Synchrotron x-ray micro-diffraction and EDS mapping revealed that the periodic region contains a combination of amorphous calcium carbonate and calcium phosphate, while the impact region features highly textured crystalline hydroxyapatite mineral. One of the main conclusions of this work was that the inner periodic region (Figure 2.1 A, boxed region) functions as the primary energy-absorbing layer (13; 14).

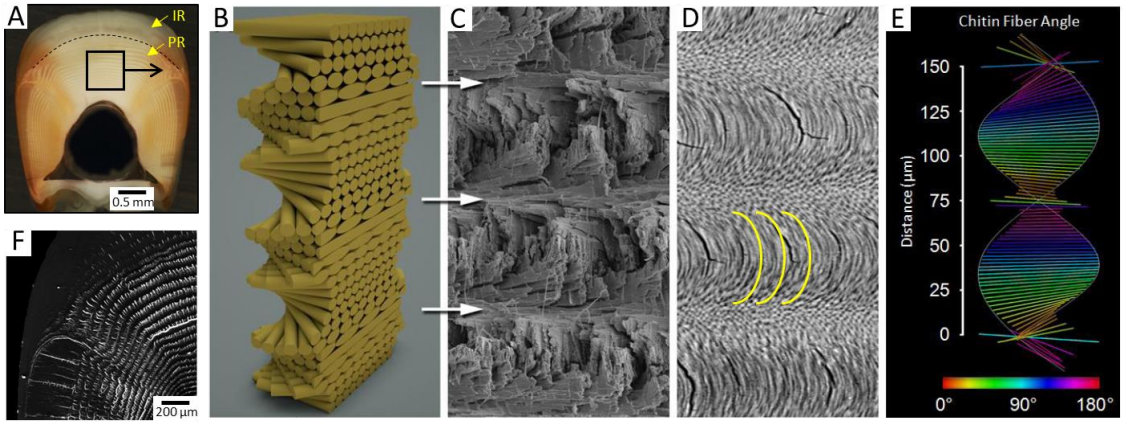

Figure 2.1. Helicoidal (Bouligand) fiber architecture within the dactyl periodic region. (A) Dark field micrograph of transverse cross-section of the dactyl club highlighting its multi-regional design. IR and PR denote impact and periodic regions, respectively. (B) Model and (C) fractured surface of the laminated helicoidal fiber architecture observed within the periodic region. (D) Polished cross-section revealing the nested arc pattern of microcracks. (E) Measurement of the chitin fiber angle for different layers. (F) Nested microcracks within the periodic region highlighting controlled and non-catastrophic fracture. Panels *B, C, D, E, F* reproduced from References (13; 14).

The combination of soft polymeric nanofibers and stiffer amorphous calcium carbonate and calcium phosphate mineral provides a periodic modulus mismatch leading to crack deflection, which in combination with its helicoidal (Bouligand) architecture of

fibers (Figures 2.1 B, C, E) allows for an enhanced work of fracture due to crack twisting (Figures 2.1 D, F) (13; 14; 103). Additional work showed that this helicoidal design provides a shear wave filtering effect during impact (104). Moreover, dynamic finite element analysis and micromechanical modeling showed that the maximum principal stresses during an impact event occur closest to the impact surface within the outer exocuticle layer (14). Although the effective transfer of impact momentum to its prey necessitates a hard and stiff outer region, details concerning the ultrastructural–mechanical property relationships of the impact region and impact surface have not yet received full attention. A recent examination of crystalline and chemical aspects of the impact region suggested the presence of a fluorinated apatite–calcium sulfate phase (105). Additionally, supporting nanomechanical studies revealed the anisotropic stiffness response and quasi-plastic nature of the impact region (105; 106). However, key details regarding the micro- and nano-structural features and the corresponding mechanical response have yet to be revealed.

2.2 Objectives & hypotheses

The objectives of this work are to characterize the multi-length-scale structure, chemical composition, and mechanical properties of the dactyl impact region and surface. Fracture analysis and advanced in-situ mechanical characterization will also be used to identify potential toughening mechanisms within these regions. Given that the dactyl experiences highest principal stresses nearest to the impact surface during striking, it is suspected that the impact region requires an adequate combination of hardness and

toughness. Moreover, it is expected that the impact region and impact surface feature a similar helicoidal architecture of fibers given their close proximity to the perioidic region as well as comparable microstructures in the cuticles of other arthropod systems (107-111). It is also suspected that the highest concentrations of mineral elements (i.e., Ca, P) are located within the impact surface, which correlate with the highest elastic modulus and hardness.

2.3 Materials & methods

Research Specimens: Live specimens of *Odontodactylus scyllarus* were obtained from a commercial supplier and housed in an artificial seawater system. Fresh inter-molt dactyl clubs were obtained from both live and recently deceased specimens. Polished cross-sections of the dactyl club were prepared by embedding in epoxy (System 2000, Fibre Glast Developments Corp., USA), sectioned using a low-speed saw with diamond blade, and polished with progressively finer silicon carbide and diamond abrasive down to 50 nm grit. Fractured samples were obtained along the sagittal plane using a hammer and sharpened chisel. To highlight interfaces of the fibrous microstructure in the herringbone structure from polished sections, some specimens were washed in dilute aqueous solutions of acetic acid, ethylenediaminetetraacetic acid, or citric acid for various periods of time to partially demineralize the sample surface. Occasionally, samples were also washed in dilute aqueous solutions of sodium hydroxide to remove protein to characterize the polysaccharide fibers. Samples were finally washed in deionized (DI) water and dried in air prior to SEM

observation. The University of California Riverside has no specific guidelines for experiments on invertebrate organisms.

Nanoindentation: Nanoindentation on flat polished cross-sections of the dactyl club was performed at room temperature using a TI 950 TriboIndenter (Hysitron, USA). Indentation mapping of the impact region was performed using a low-load transducer with a diamond cube corner tip. Indents were placed in a square array and controlled in displacement to a depth of 200 nm. The trapezoidal load function consisted of a 5 s load, followed by a 2 s hold, and a 5 s unload. High-resolution mapping was performed on a 90 by 90 μm area and indents were spaced 3 μm apart. Lower-resolution mapping was performed on a 1.2 by 1.2 mm area and indents were spaced 30 μm apart. Values for reduced elastic modulus and hardness were calculated using the Oliver and Pharr method (112). Spatial maps of reduced modulus and hardness were subsequently plotted using the scatter function in MATLAB (MathWorks, USA). High-load indents were performed using a high-load transducer with a diamond cube corner tip to induce fracture. Indents were placed individually in areas of the impact region and impact surface and were controlled in load. The load function consisted of a 5 s load followed by a 5 s unload.

SEM: Fractured, microtomed, and polished indented sections of the dactyl club were mounted to aluminum pin mounts using carbon tape and sputter coated with a thin layer of platinum and palladium. In some cases, conductive silver paint was also applied to increase conductivity and prevent charging. Specimens were imaged at 10 kV using an XL-30 FEG (FEI-Philips, USA).

X-Ray Mapping: Polished sections of the club were mounted on carbon tape-coated aluminum stubs, carbon coated, and analyzed using a JSM-840 SEM (JEOL, USA) operating at 20 kV. X-ray maps were post-processed using the "Chemical Imaging" software package within the Moran Scientific Microanalysis System (113).

TEM: Specimens for TEM were prepared by first isolating 1 mm cubed pieces of the impact region, which were cut from a transverse section of the dactyl club using a razor blade. The pieces were then fixed with glutaraldehyde (2.5%) in aqueous sodium phosphate buffer solution (0.1 M, pH = 7.2) for 2 h and subsequently washed in DI water three times for 5 min each. Specimens were then post-fixed in osmium tetroxide (1%) in sodium phosphate buffer (0.1 M, pH = 7.2) overnight and washed again in DI water three times for 5 min each. Samples were serially dehydrated to 100% ethanol and embedded in resin (Epofix Cold-Setting Embedding Resin, Electron Microscopy Sciences, USA) in silicon molds at room temperature overnight. Cured resin blocks were then sectioned using an ultramicrotome (RMC MT-X, Boeckeler Instruments, USA) and diamond knife (PELCO, Ted Pella, USA) to produce 70 nm thin sections, which were deposited on carbon-coated copper grids and imaged at 300 kV in a CM300 TEM (FEI-Philips, USA).

In-situ TEM Picoindentation: Thin sections of the bulk impact region were milled from a polished transverse section using a LYRA3 FIB-SEM (TESCAN, USA). In-situ indentation was performed using a PI-95 TEM Picoindenter (Hysitron, USA) and imaged in a Tecnai F30 TEM (FEI, USA) at 300 kV. Samples were indented using a boron-doped diamond wedge tip with 100 nm radius of curvature and controlled under load at a rate of 0.18 $\mu N\ s^{-1}$.

3D Printing and Bulk Mechanical Testing: Cylindrical samples were printed in a Connex350 (Objet, USA), using VeroWhitePlus for the fibers and TangoBlackPlus for the matrix. In both cases the cylinders are 60 mm in diameter and 37 mm in height. The volume fractions are 0.242 and 0.267, for the Bouligand and herringbone, respectively. The samples were tested under compressive load in a MTS Insight 300 (MTS System Corporation, USA) using a 569331-01 load cell; the rate used was 0.5 mm min^{-1}. The software VIC3D from Correlated Solutions was employed for the 3D Digital Image Correlation analysis.

3D Finite Element Modeling (FEM): The FEM simulations were carried out in Abaqus/Standard (114). For the herringbone structure, we used 81 × 81 × 81 trilinear elements (C3D8), and the body was subjected to uniaxial strain conditions in the *z* direction. In the case of the particulated model, we used 594602 triangular linear elements (CPS3).

2.4 Results & discussion

2.4.1 Optical microscopy and high resolution nanoindentation of the impact region

Optical microscopy was initially used to examine the macro-structural features of the impact region (Figure 2.2). Subsequent nanoindentation mapping was used to probe the local mechanical properties at high resolution. Micro-computed tomographic (μ-CT) imaging of a polished sagittal section highlights the multi-regional nature of the stomatopod dactyl club, revealing the dense and highly mineralized outer impact region and a more organic rich inner periodic region (Figure 2.2 C) (1). Corresponding differential

interference contrast imaging (Figure 2.2 D) of the impact region highlights the thick (~ 500 μm) bulk component and the thin (~ 70 μm) surface layer (impact surface). Close observation within this bulk impact region reveals a well-defined and highly ordered herringbone pattern, which takes the form of a triangular waveform (see inset Figure 2.2 D). Each herringbone subunit has an identical wavelength, λ, equal to approximately 45 μm; however, the amplitude, A, of these units is graded in the radial direction (from 70 μm observed at the impact-periodic region interface to 100 μm at the impact region-surface interface and abruptly decreases to 50 μm within the impact surface region).

Nanoindentation within the impact region (Figures 2.2 E–I) was subsequently used to probe local and global changes in elastic modulus and hardness within the herringbone region. High-resolution mapping (Figure 2.2 F) reveals a strong correlation between the local elastic modulus (which oscillates between approximately 30 GPa and 45 GPa) and the herringbone pattern observed from the differential interference contrast image. In addition, varied gradients in reduced modulus and hardness are observed (Figures 2.2 H-I) from the periodic region into the impact region (a distance of approximately 600 microns) from 25 to 50 GPa and 0.7 to 2 GPa, respectively, and maximized at the club surface (i.e., a modulus and hardness of 60 GPa and 3 GPa, respectively). Such trends are the result of a gradient in mineralization (14).

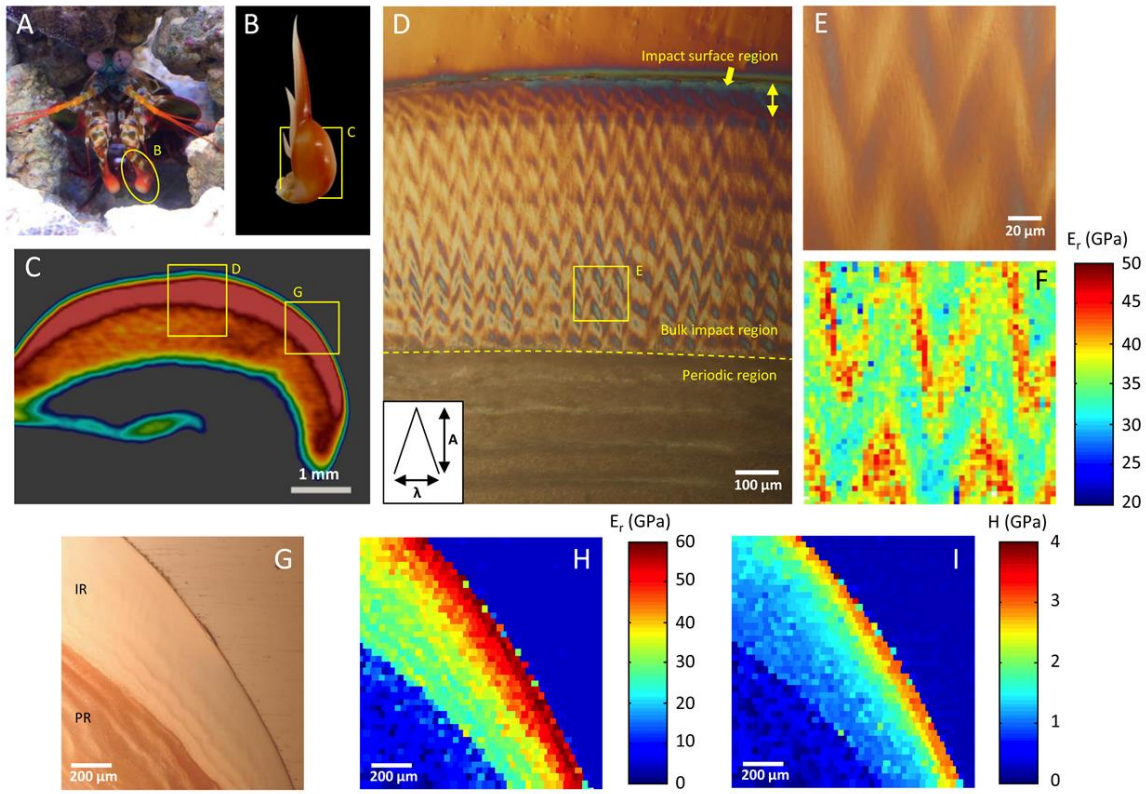

Figure 2.2. Optical microscopy and high resolution nanoindentation of the dactyl impact region. (A) Anterior of O. scyllarus with the dactyl segment circled in yellow. (B) Dactyl club separated from the raptorial appendage. Yellow box denotes the sagittal plane of section. (C) µ-CT scan of a sagittal section as denoted in (B). (D) Higher magnification differential interference contrast image of region marked in (C) highlighting the impact surface, bulk impact, and periodic regions. (E) High magnification differential interference contrast image of bulk impact region as denoted in (D). (F) High resolution nanoindentation map of region (E) displaying oscillating elastic modulus correlating with herringbone pattern observed within the bulk impact region. (G) Bright field image of impact region as denoted in (C). (H,I) Low magnification nanoindentation maps of region (G) showing gradients in reduced elastic modulus (H) and hardness (I) through the impact region and near the club surface. Figure reproduced from Reference (1).

Figure 2.3 shows the results of elemental mapping within the impact region of a polished transverse section of the dactyl. Carbon content decreases moving from the periodic region into the bulk of the impact region while calcium and phosphorus show an inverse trend (Figures 2.3 B, C, D). The impact surface shows the lowest concentration of

carbon and highest concentrations of calcium and phosphorus, indicating a very high fraction of mineral relative to organic material. Pseudo-colored mapping of magnesium, calcium, and phosphorus contents (Figure 2.3 E) show a magnesium-rich periodic region, attributed to magnesium's role in stabilizing the amorphous mineral phase, as well as a phosphorus-rich region at the impact-periodic region interface, indicating a substitution of calcium carbonate for calcium phosphate in the exocuticle (14; 102; 115; 116). The two-dimensional scatter diagram in Figure 2.3 F shows pixel frequency versus elemental cocnentration for calcium and phosphorus plotted against one another (113). Nodes in the diagram correspond to unique "phases" and chemical compositions (113). Examining regions of the highest calcium and phosphorus concentrations within the dactyl (blue and green boxes in Figure 2.3 F) reveal unique compositions that correspond to the bulk of the impact region (Figure 2.3 G) and the impact surface region (Figure 2.3 H), respectively. Quantitative elemental analysis via EDS shows Ca/P molar ratios of 2.07 and 1.97 for the impact surface and impact region, respectively. This variation could be attributed to the substitution of fluorine, sulfur, and perhaps carbonate into the apatite crystal closer to the club surface, which, as reported previously, would explain the higher elastic modulus and hardness within the impact surface (105).

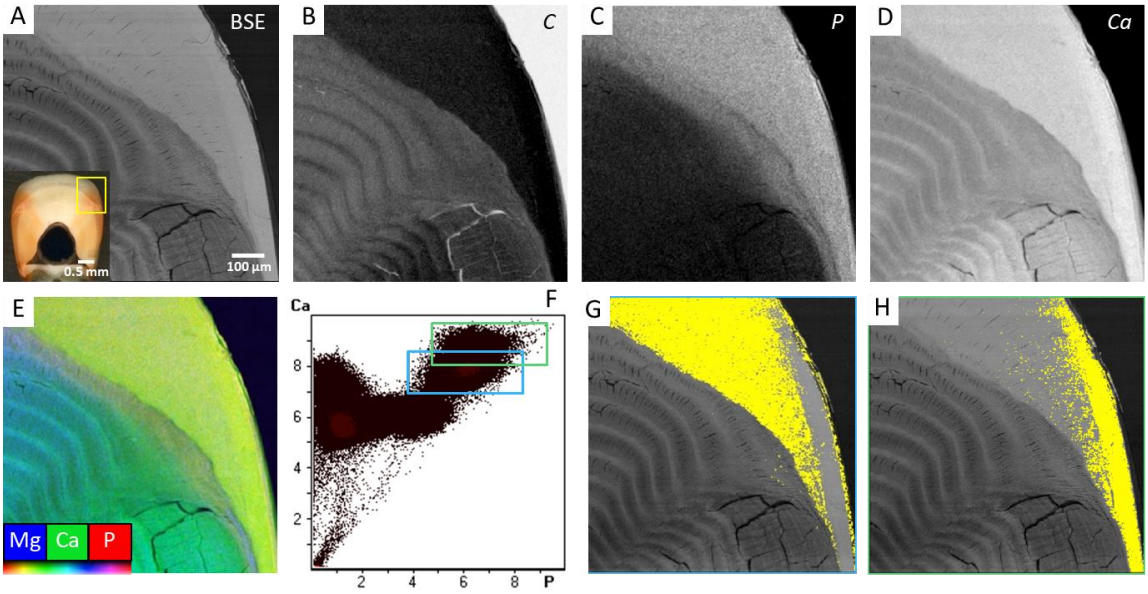

Figure 2.3. X-Ray mapping and elemental analysis of the impact region. (A) Backscattered electron micrograph of the impact region from a polished transverse section of the dactyl club. Inset showing polished transverse section with yellow boxed region indicating mapped region. (B-D) EDS maps showing local distribution of carbon, phosphorus, and calcium respectively. (E) Pseudo-colored map revealing local concentrations of magnesium (blue), calcium (green) and phosphorus (red). (F) Scatter diagram of mapped area showing pixel frequency versus elemental concentration profiles for calcium and phosphorus plotted against one another. (G, H) Maps displaying regions of unique composition of calcium and phosphorus corresponding to the green and blue boxed areas, respectively, of the scatter diagram in (F). Highlighted region in (H) corresponds to nanoparticulated surface domain. Figure reproduced from Reference (1).

2.4.2 Micro- and nano-structural characterization of the impact region and surface

Analysis of a fractured dactyl club (along its sagittal plane) by SEM (Figure 2.4) reveals that the characteristic helicoidal arrangement of mineralized chitin fibers observed in the periodic region is highly compacted laterally within the impact region, forming a herringbone pattern (Figure 2.4 A). Fibers continue to rotate in the plane (x-y) of the micrograph (Figure 2.4 B) about an axis (z) normal to the club surface; however, the

laminations appear to be compacted in the azimuthal directions, yielding sinusoidally bent fibers forming the herringbone pattern. Closer observation (Figure 2.4 C) highlights that the out-of-plane mineralized fibers that are oriented normal to the plane of fracture are interspersed between vertically aligned fibrous pore canal tubules, which remain in a fixed orientation normal to the surface of the dactyl club. In-plane fibers, which are oriented parallel to the plane of fracture (Figure 2.4 D) are 49 ± 13 nm in diameter. The oriented pore canal tubules are also a common feature of the Bouligand structure, which not only function as channels for material transport during molting, but also serve an important mechanical role in terms of imparting anisotropy and toughness (109; 117; 118). In fact, the continuation of fibrous pore canal tubules from the periodic region into the impact region likely plays a role in strengthening this interface, which can experience shear and tensile stress due to wave propagation upon impact (104). Similar tubular structures such as those found in bone, teeth and horns have been found to enhance toughness through mechanisms such as crack deflection and resistance to microbuckling (119; 120). A schematic depicting the intersecting rotating fiber and pore canal tubule architecture is shown in Figure 2.4 E. Thus, it is likely that areas of higher elastic modulus observed in Figure 2.2 F correlate to the interrogation of out-of-plane fibers while lower values of elastic modulus likely result from probing in-plane fibers. This is due not only to the mechanical anisotropy of the chitinous fibers, but also due to the high degree of crystallographic texturing of the apatite mineral phase (14; 121). The herringbone structure observed in the bulk of the impact region transitions (Figure 2.4 F) to densely packed nanoparticles (with an average diameter of 64 ± 12 nm) with pore canal tubules persisting

to the club surface. The persistence of a wavy (sinusoidal) pattern within the impact surface region (Figure 2.5) suggests the presence of a structural gradient across the bulk impact region-impact surface interface.

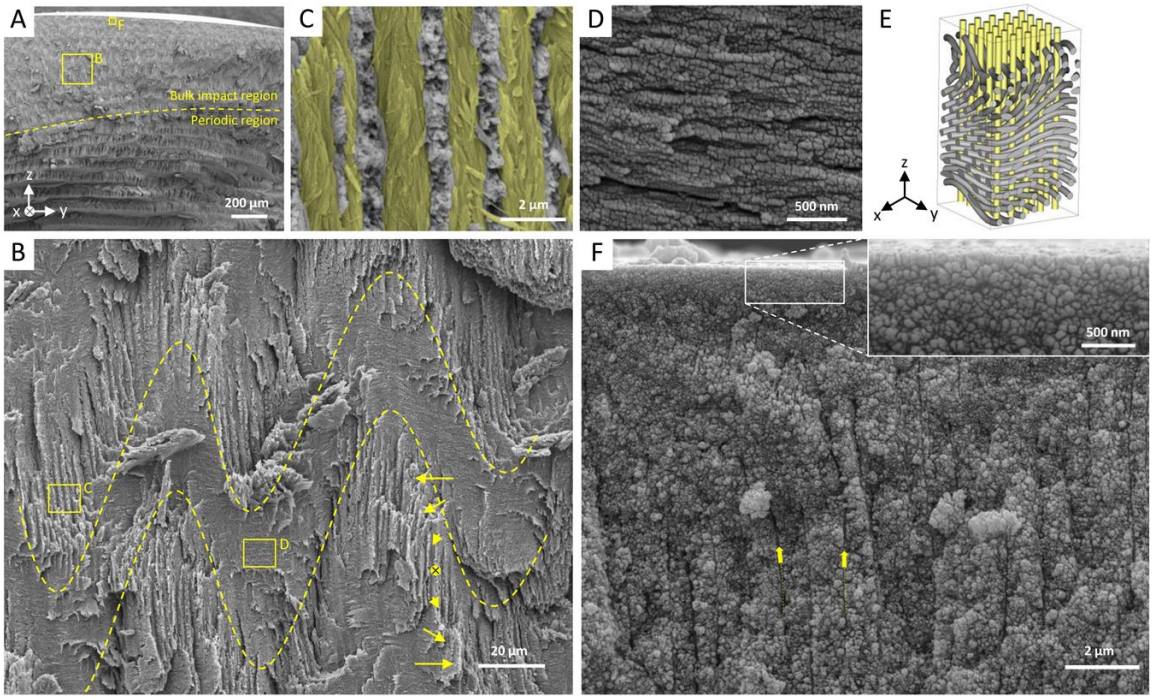

Figure 2.4. Microstructural features of the impact region. (A) SEM of fractured sagittal plane. Dashed line highlights the interface between impact and periodic regions. (B) Higher magnification of the bulk impact region as depicted in (A) showing the compacted helicoidal structure forming the herringbone motif. Dashed lines correspond to in and out of the plane fiber orientations. Arrows denote local fiber orientation. (C,D) High resolution SEM micrographs from (B) showing mineralized fibers oriented out of the plane of the page (C) and in the plane of the page (D). Out of plane oriented fibers reveal underlying network of fibrous pore canal tubules (yellow), which are aligned normal to the dactyl club surface. (E) Schematic showing the organization of rotating fibers and interpenetrating fibrous pore canal tubules. (F) Magnified area of region shown in (A) highlighting the particle morphology within the impact surface region. Arrows and dashed lines denote pore canal channels oriented normal to the club surface. Inset showing nanoparticles averaging 65 nm in diameter located at the outermost surface of the club. Figure reproduced from Reference (1).

Samples of the dactyl club were additionally etched in dilute acid to remove the mineral in order to better characterize the structure of the fibrous organic matrix. Figure 2.6 shows the results of a two-day long demineralization of a polished transverse cross-

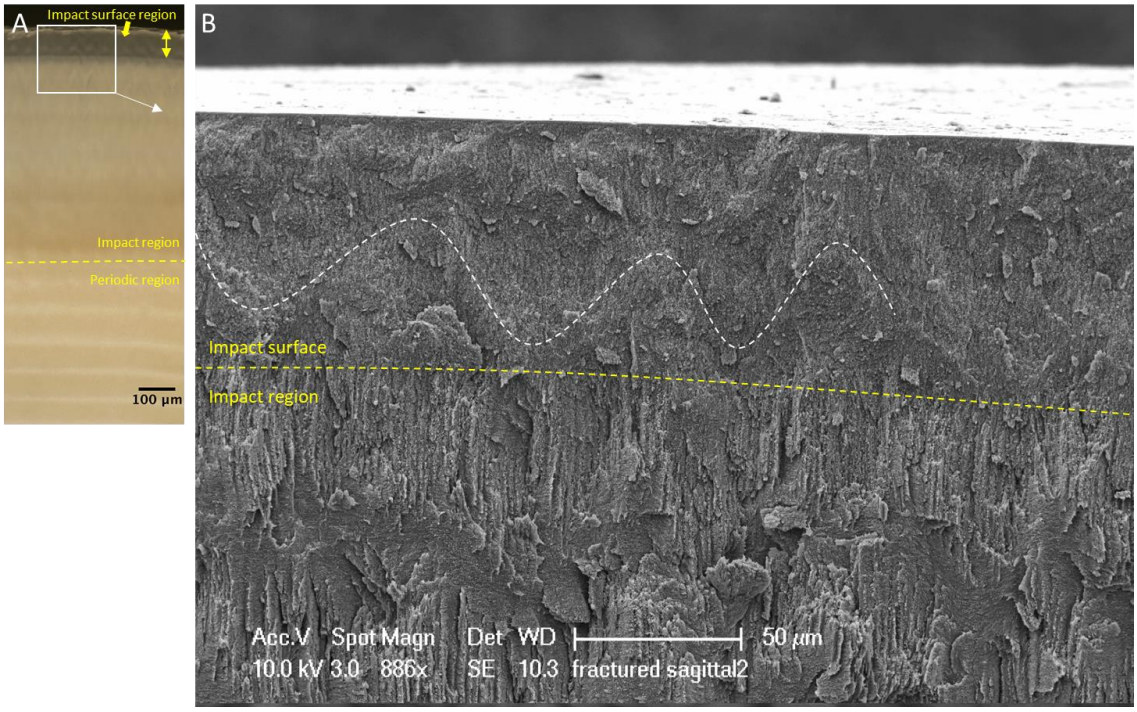

Figure 2.5. The impact region-impact surface interface. (A) Dark-field optical micrograph of a polished sagittal section of the dactyl club showing distinctions between the periodic region, impact region, and impact surface. (B) SEM micrograph of a fractured sagittal section of the dactyl (region from boxed area in Panel A), highlighting the presence of a herringbone pattern within the impact surface, indicating a structural gradient across the impact region-impact surface interface.

section of the dactyl in 0.1 M ethylenediaminetetraacetic acid followed by deproteination in 1 M sodium hydroxide for an additional 48 hours. Notice the collapse of the periodic and striated regions, due to the ease with which the amorphous mineral is removed (Figure 2.6 A). By comparison, the impact region appears to be less deformed, which can be attributed to the presence of crystalline mineral: hydroxyapatite and potentially fluorinated

apatite, which are more stable and resistant to dissolution. Closer examination of the impact surface reveals that nanoparticles of apatite are still present after the etching treatment (Figure 2.6 B). In other areas of the impact surface, the demineralization effectively removed most of the mineral, revealing the chitinous scaffold fibers (Figure 2.6 C); however, some nanoparticles are still present. A most interesting observation can be made by looking at the impact-periodic region interface. As we move from the impact region towards the periodic region (Figure 2.6 D), wavy sinusoidal fiber layers (Figure 2.6 E) begin to flatten out, showing a decrease in amplitude, until flat Bouligand layers are observed within the periodic region (Figure 2.6 F). This structural gradient, coupled with elemental data (presented in Figure 2.3), may provide clues as to the mechanisms driving the formation of the herringbone architecture. This topic will be discussed further in Section 2.4.4.

A coronal section of the dactyl impact region was also demineralized in order to better characterize the 3-dimensional nature of the herringbone architecture. Figure 2.7 shows the results of a polished coronal section of the dactyl club within the impact region that was lightly etched and fixed in 20 mM citric acid + 2.5 % (v/v) glutaraldehyde for 5 minutes. In this orientation, etching reveals the opening of the pore canal tubules (Figures 2.7 C, D, E, F). Moreover, the tubules are arranged in a sinusoidal pattern (Figures 2.7 C, D), consistent with the herringbone pattern and architecture observed in the sagittal and transverse planes. The pore canal tubules have an inner diameter of 200 – 500 nm and are spaced approximately 2 μm from one another (Figures 2.7 E, F). The hollow nature of the tubules further suggests their multifunctional role: mechanical anisotropy and resistance to

buckling as well as conduits for the transport of mineral species (resorption & deposition) during periodic molting events (119).

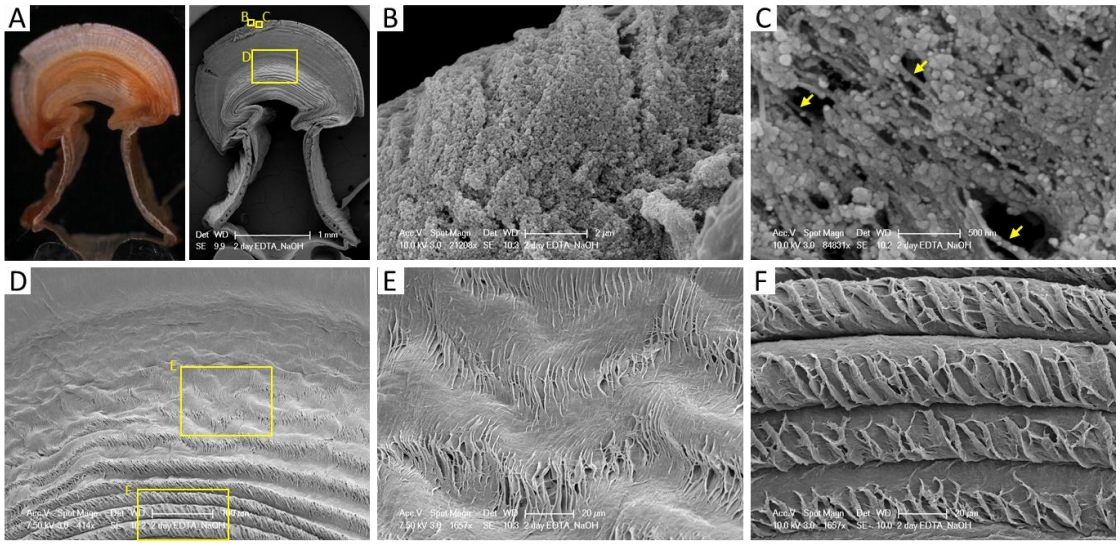

Figure 2.6. Demineralized/deproteinated surface of the dactyl club. (A) Dark-field optical (left) and SEM (right) micrographs of the post-48-hour demineralized and deproteinated polished transverse cross-section of the dactyl. (B) SEM micrograph of the impact surface (region denoted in Panel A) showing abundance of apatite nanoparticles. (C) High magnification SEM micrograph of impact surface (region denoted in Panel A) showing organic fibrils (denoted by arrows) with attached mineral nanoparticles. (D) SEM micrograph of the impact-periodic region interface (region denoted in Panel A), showing transition of wavy fiber layers to flat fiber layers. (E) Higher magnification SEM micrograph (region denoted in Panel D) showing herringbone fiber layers at the impact-periodic region interface. (F) Higher magnification micrograph (region denoted in Panel D) showing flat Bouligand fiber layers within the periodic region.

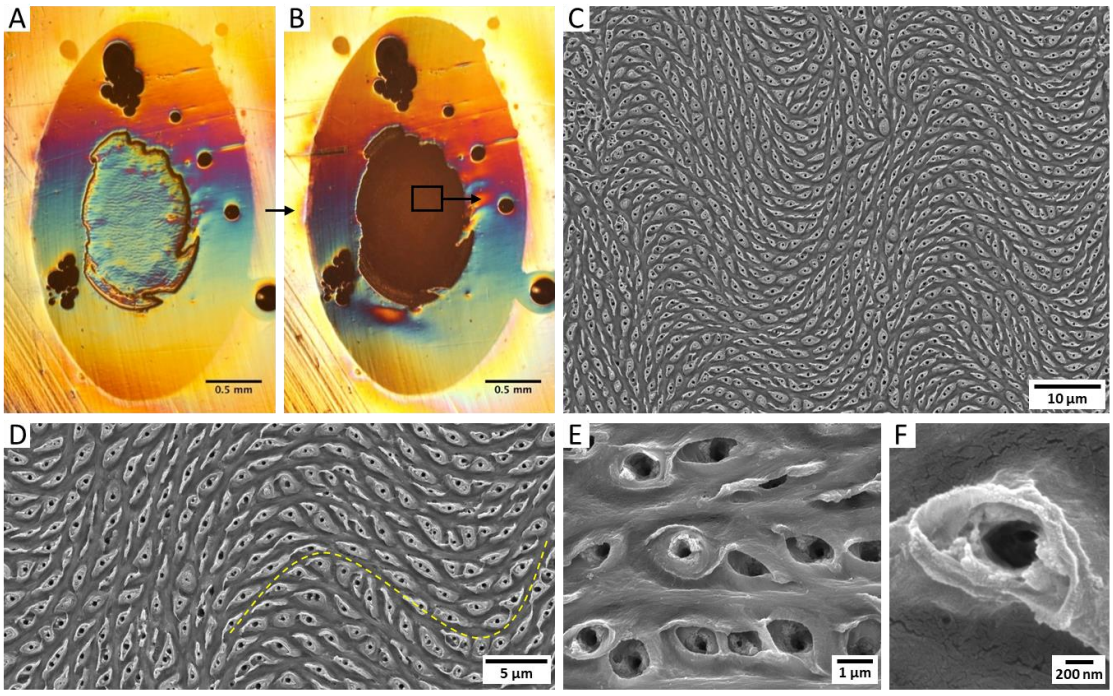

Figure 2.7. Coronal impact region demineralization. (A) Differential interference contrast micrograph of the polished coronal section through the impact region before demineralization. (B) Differential interference contrast micrograph of polished section after demineralization treatment. (C) Low magnification SEM micrograph of the etched coronal surface as denoted by the boxed region in (B). (D) Higher magnification SEM micrograph showing sinusoidal arrangement (dashed yellow line) of exposed pore canal tubules. (E) Higher magnification SEM micrograph of open pore canal tubules. (F) High magnification SEM micrograph of a single exposed hollow pore canal tubule.

Transmission electron microscopy (TEM) was subsequently used to interrogate the nano-structural and crystallographic features of both the impact region and surface (Figure 2.8). Inspection of the impact surface (Figure 2.8 A) confirms the observed nanoparticle morphology and array of pore canal tubules. Selected area electron diffraction (SAED, Figure 2.8 B) and HRTEM and fast Fourier transform (FFT) analysis/ inverse fast Fourier transform (IFFT) analysis (Figure 2.8 C) within the impact surface corroborates that the particles are isotropic single crystalline hydroxyapatite.

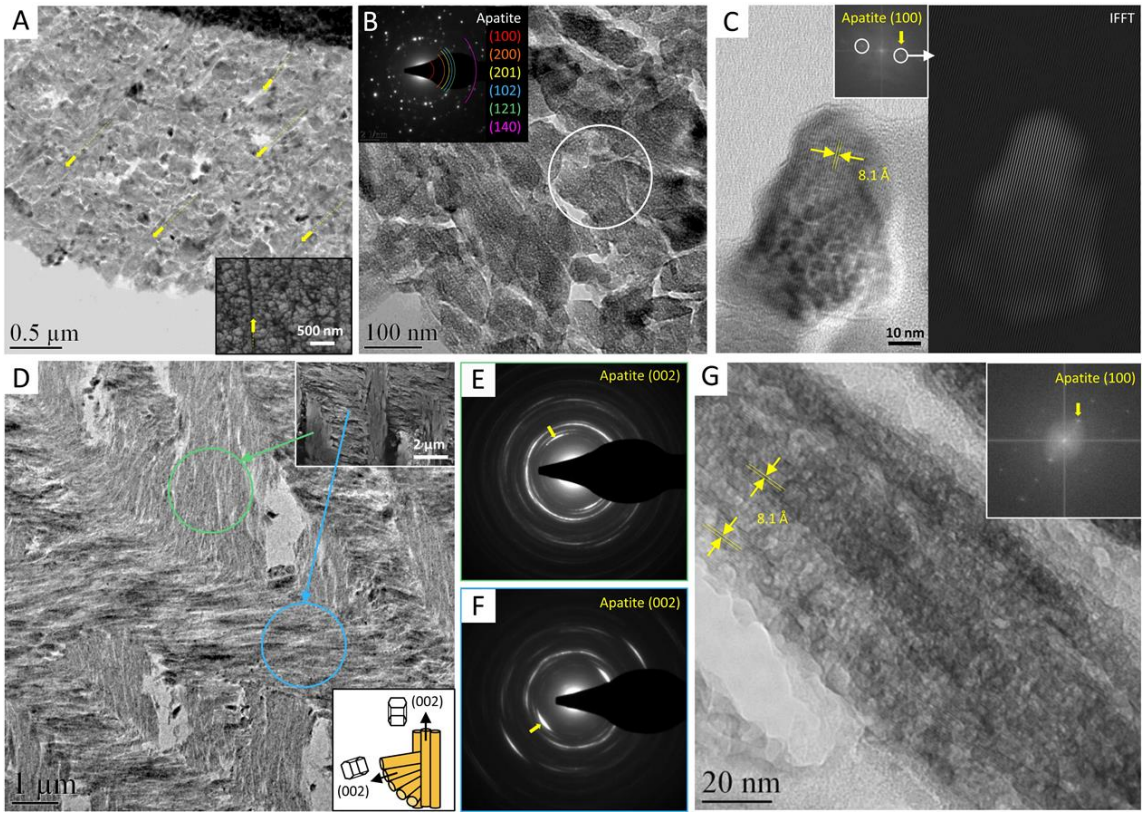

Figure 2.8. Nanostructural features of the impact region. (A) Low magnification TEM micrograph of impact surface showing pore canal fibers (marked by yellow arrows) that penetrate through to the club surface. Inset showing corresponding SEM micrograph of impact surface. (B) Higher magnification of impact surface showing nanoparticle morphology. Inset: diffraction pattern of selected area suggesting single crystalline nature of the nanoparticles. (C) (Left) High resolution TEM of an isolated nanoparticle, inset showing FFT revealing apatite (100) planes. (Right) IFFT of masked (100) planes highlighting the entire nanoparticle thus confirming single crystallinity. (D) TEM micrograph of the bulk impact region showing in-plane rotating fibers intersecting with out-of-plane pore canal fibers. Lower inset: schematic showing apatite texturing scheme and fiber architecture of the impact region, corresponding to (D). Upper inset: SEM micrograph of microtomed thin section of impact region revealing in-plane and pore canal fibers. (E,F) Selected area diffraction patterns from regions shown in (D) highlighting the preferred orientation of apatite c-axis parallel to the fiber axes for pore canal fibers (E) and in-plane rotating fibers (F). (G) Higher magnification of single mineralized fiber from (D). Inset: Fast Fourier Transform of (G) highlighting apatite (100) planes oriented parallel to the fiber long axis. Figure reproduced from Reference (1).

Bright-field TEM of the bulk of the impact region highlights the superimposed orthogonal fiber bundles within the herringbone structure (Figure 2.8 D). SAED (Figures 2.8 E and F) corresponding to the vertically oriented pore canal fibers and the horizontally oriented in-plane fibers, respectively, reveals the strong crystallographic texturing of the apatite mineral phase with the (002) planes showing a preferred orientation normal to the fiber direction. Thus the apatite c-axis has a preferred orientation parallel to the long axis of chitin fibers. High-resolution bright-field TEM of an isolated mineralized chitin fiber within the impact region (Figure 2.8 G) and a corresponding Fast Fourier transform (inset, Figure 2.8 G) reveal the lattice spacing and orientation of the (100) apatite planes, which supports the proposed texture of the mineral phase. Previous synchrotron x-ray diffraction studies proposed that the apatite mineral phase had a preferred orientation with the crystallites c-axis orientation perpendicular to the club surface; however, our TEM analyses show that this is only true for the pore canal tubule fibers (14). In-fact, the c-axis orientation of apatite is preferentially aligned parallel to the fiber long axis and thus, for the rotating fibers, the apatite c-axis has a preferred orientation parallel to the local fiber orientation of the herringbone structure.

2.4.3 High-load nanoindentation and in-situ TEM pico-indentation

High load nanoindentation within the bulk of the impact region was used to initiate fracture and examine the effect of local microstructure on crack propagation in order to identify potential toughening mechanisms of the herringbone structure. A representative SEM micrograph (Figure 2.9 A) of a 1000 mN peak load indent placed within the bulk of

the impact region, which was subsequently etched in dilute acid to highlight structural features, reveals contrast due to the preferential etching of out-of-plane fibers of the herringbone structure. Cracks are observed emanating from the area of the indent; however, these cracks appear to become arrested at the transitional zones between in-plane and out-of-plane oriented fibers. Examination further away from the indent shows that cracks re-appear within areas containing out-of-plane fibers. In fact, cracking is observed only in regions where the local fiber orientation is normal to the plane of the section. It is expected that cracks twist as well, following the local orientation of helicoidally-arranged fibers. Similar observations have been made with respect to the periodic region of the dactyl club and helicoidal structures found within most arthropod cuticles as well as other natural composite materials including lamellar bone, cell walls of wood and fish scales (13; 14; 70; 122-126). Crack deflection is an extrinsic form of toughening that is well-documented in natural composite materials, specifically biomineralized tissues (3). The periodic nature of hard and soft interfaces, in this case between alpha-chitin fibrils and hydroxyapatite crystals, results in a crack-tip shielding effect that changes the crack driving force and thereby arresting crack propagation (127; 128). He and Hutchinson discussed the role of elastic mismatch on the strain energy release rate of a crack, which determines if the crack gets deflected at an interface or penetrates through to the other solid (129).

However, unlike a simple 90° crack deflection, cracks within this structure are twisting and thus increase toughening. We hypothesize that, as opposed to crack deflection in interfaces as observed in other biological materials like nacre, crack twisting in a helicoidal structure can provide (i) a strategy to create multiple twisting microcracks that

grow at different nucleation sites but never coalesce given the nature of the helicoidal architecture and (ii) more crack surface per unit volume, and therefore maximizing energy dissipation (13; 14).

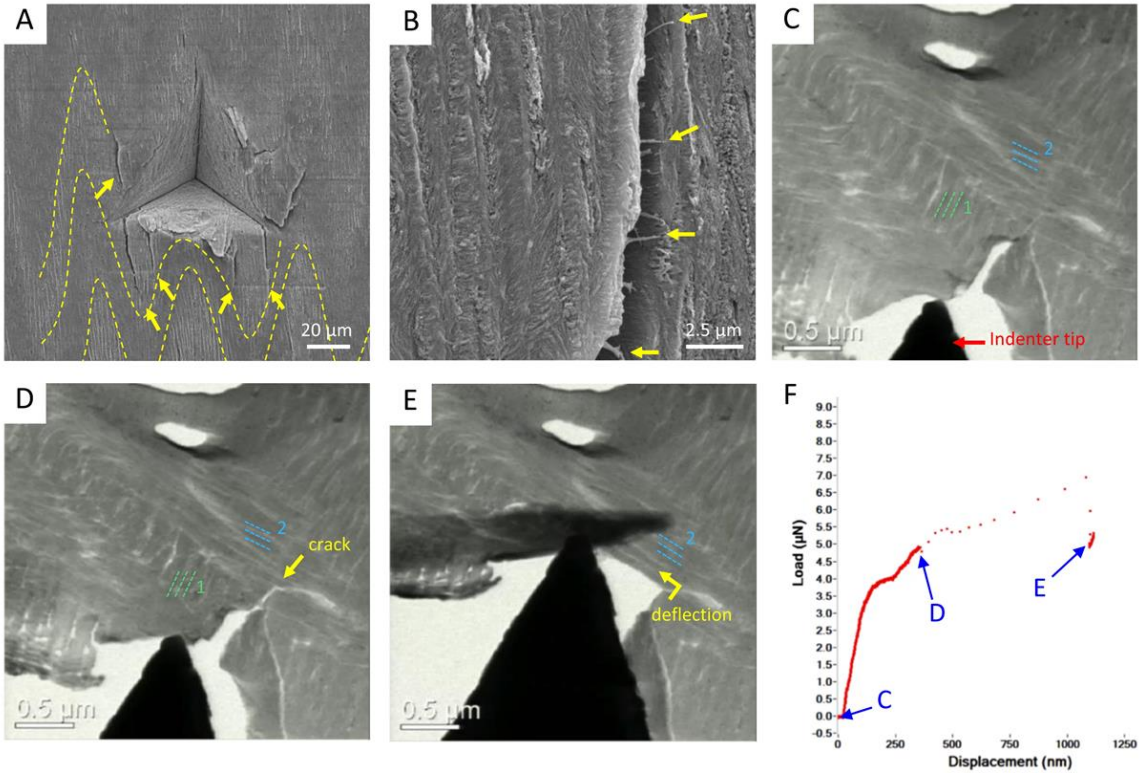

Figure 2.9. High load nanoindentation and in-situ TEM picoindentation of the bulk impact region. (A) SEM micrograph of 1000 mN peak load indent placed within the impact region. Surface was lightly etched to reveal the herringbone structure and crack deflection (arrows) at interfaces between in-plane and out-of-plane fiber orientations (dashed line). (B) SEM micrograph showing fiber bridging (yellow arrows) at the indent edge. (C-E) TEM micrographs showing progressing stages of loading of a FIB-sectioned area of the bulk impact region. The local microstructure consists of overlapping fiber bundles that are oriented normal to one another. Dashed blue and green lines depict local fiber orientation from two separate overlapping bundles (1 and 2, respectively), which correspond to rotating and pore canal fibers of the herringbone structure. (F) Load-displacement curve at various stages of indentation corresponding to (C-E). (C,D) Mode I crack is opened at pre-existing notch in region 1 and propagates in the direction of the local fibers (dashed green lines). (D) Crack approaches fiber bundle 2 and begins to deflect at an off-angle. (E) Localized failure as crack transitions to mode III failure due to out-of-plane bending. Crack is deflected 90° in the direction of bundle 2 fibers (dashed blue lines). Figure reproduced from Reference (1).

In addition to crack deflection/rotation, we also observe fibrils bridging an opened crack surface adjacent to the indented area (Figure 2.9 B). These fibers act to reduce the crack-tip stress concentration and prevent further crack opening, providing an additional source of extrinsic toughening (17; 40; 130). Finally, we expect that the herringbone structure offers an additional improvement in toughening over a helicoidal motif by incorporating a sinusoidal interface between lamellar fibrillar layers.

In order to examine in-situ fracture and identify toughening mechanisms at the nanoscale within the bulk impact region, TEM pico-indentation was performed on a focused-ion beam (FIB) milled section. Figures 2.9 C - F show the results of progressing stages of quasi-static loading of a thin section containing overlapping fiber bundles (correspond to the in-plane and pore canal tubule fibers, Figure 2.9 C) that are oriented normal to one another. Initially, a mode-I crack is opened at a pre-existing notch located within fiber bundle 1 (green dashed lines, corresponding to the in-plane mineralized fibers) and continues to propagate parallel to the long axis of these fibers (Figure 2.9 D). After reaching a load of approximately 5 μN, the crack front approaches fiber bundle 2, which corresponds to a fibrous pore canal tubule (blue dashed lines) oriented normal to the direction of crack propagation. Beyond this load, the material fails locally as the crack is deflected and transitions to mode-III failure due to out-of-plane bending (Figure 2.9 E). Direct observations from the TEM micrograph show that the crack was deflected 90° in the direction of the pore canal fiber bundle. Load-displacement data of the indentation event (Figure 2.9 F) highlights an initial linear-elastic region followed by a pop-in event, which corresponds to the crack opening as shown in Figure 2.9 D. These results not only

provide direct evidence of nanoscale extrinsic toughening through crack deflection at an orthogonal fiber interface, but also highlight the effect of crystallographic texturing (results from Figure 2.8) on imparting mechanical anisotropy to polymeric fibers.

2.4.4 Finite element analysis and testing of 3D printed mimics

Finite element (FE) analysis in combination with 3D printing was used to examine the role of the herringbone architecture on the mechanical performance under compression versus a helicoidal structure. Schematics of the helicoid and a herringbone architecture are shown in Figure 2.10 A (left and right, respectively). The coloration denotes the relative position of the fibers along the z-axis. The herringbone microstructure was modeled using a transverse isotropic material, changing the orientation of the symmetry axis for each element. This alignment follows the tangent of the curve formed by the intersection of Equation (1) and a vertical plane rotated by the pitch angle. Both helicoidal and

$$f(x,y) = A\sin\left(\frac{2\pi x}{\lambda}\right)\sin\left(\frac{2\pi y}{\lambda}\right) \quad (1)$$

herringbone structures were subjected to uniaxial strain conditions in the *z* direction. Figures 2.10 C and 2.10 D show surfaces of constant normalized von Mises stress ($\sigma_{\text{Mises}}/E_{\text{t}}$) for 1.89×10^{-2}, 1.95×10^{-2}, and 2.28×10^{-2} subjected to compressive loading for the Bouligand and herringbone structures, respectively. These results reveal that the herringbone structure allows for a greater redistribution of stresses compared to the helicoidal design. Our hypothesis is that the redistribution of stresses is directly translated into a redistribution of damage, opposed to a localization, which would lead to catastrophic failure.

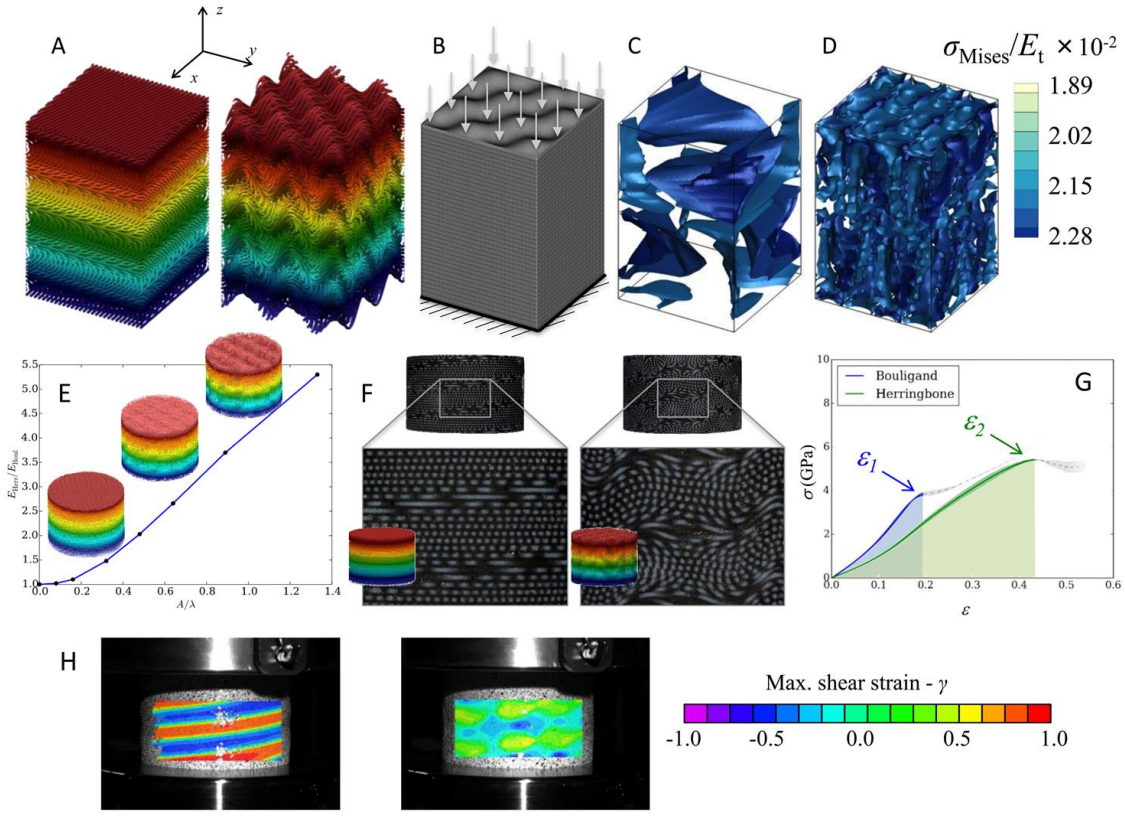

Figure 2.10. Finite Element Analysis and testing of 3D printed mimics comparing the helicoidal and herringbone structures. (A) Schematic of the geometry and fiber orientation for the helicoidal and herringbone structures. The colors represent the relative position along the z-axis. (B) A mesh for the case of the herringbone structure used for the analysis. (C-D) Surfaces of constant normalized von Mises stress (σ_{Mises}/E_t) for the values 1.89×10^{-2}, 1.95×10^{-2}, and 2.28×10^{-2} for the helicodial (C) and herringbone (D) cases. Observe the von Mises stresses that are redistributed within the volume. (E) Relative Young modulus for herringbone pattern with respect to the helicoidal case. The horizontal axis shows the aspect ratio between the amplitude and wavelength of the herringbone pattern. (F) 3D printed samples of the helicoid and herringbone structures. (G) Results of compression tests for the 3D printed samples. (H) Comparison for the 3D printed samples at a deformation of 0.1 (left, helicoidal; right, herringbone). Figure reproduced from Reference (1).

The effect of the amplitude to wavelength ratio, A/λ, of the herringbone structure on the mechanical properties was also examined under uniaxial stress loading conditions. We recall that the herringbone structure within the impact region of the dactyl club exhibits

increasing amplitude moving from the impact-periodic interface to the club surface. This is evident by differential interference contrast imaging at this interface showing flat layers within the periodic region gradually becoming wavy, then finally forming a well-defined herringbone pattern within the impact region (Figure 2.11). We hypothesize that certain crystallization stresses occur during the transformation from a hydrated amorphous state (within the periodic region) to hydroxylapatite (within the impact region) driving the formation of the herringbone-like structure. Figure 2.10 E shows that the normalized effective Young's modulus of the herringbone structure increases with A/λ (note that the helicoid corresponds to $A/\lambda = 0$). While nanoindentation in the sagittal plane (Figure 2.2 H) shows a similar trend of increasing E_r moving towards the club surface, it is likely that this is due to the gradient in mineralization (increasing mineral content near the club surface).

Nonetheless, we hypothesize that the amplitude gradient of the herringbone structure also contributes to a gradient in Young's modulus in the loading direction of the club. This structural gradient would ensure that there is no abrupt interfacial plane where the material properties completely and drastically change from one region to the other, which likely plays an important role in preventing cracks from initiating at this interface thus causing the material to fail catastrophically. Previous studies have shown that increasing the amplitude to wavelength (A/λ) ratio of sinusoidal interfaces in materials can delay unstable crack propagation and increase toughness (131; 132). Our results may

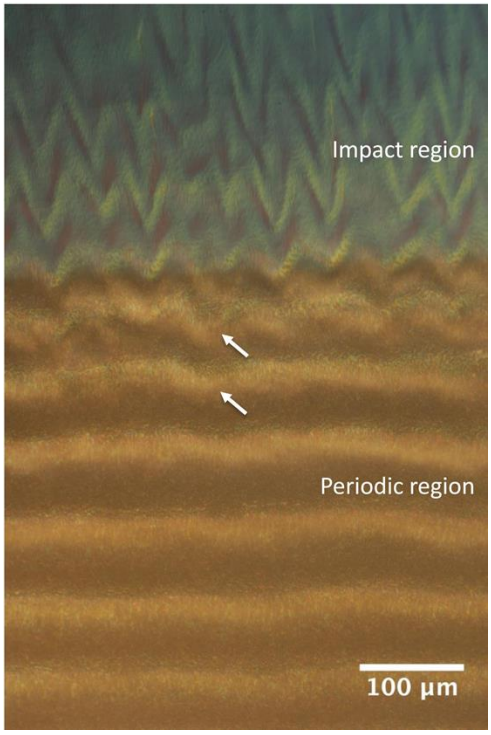

Figure 2.11. Differential interference contrast image of impact region-periodic region interface showing a gradual transition from flat Bouligand layers within the periodic region to a well-defined herringbone structure within the impact region.

provide new insights on how to impart additional toughness as well as modulate through-thickness stiffness in composite laminates by varying the architecture of in-plane fibers. Carbon-fiber epoxy composite laminates mimicking the helicoidal architecture of the periodic region have been found to exhibit improved impact-resistance in comparison to traditional quasi-isotropic aerospace designs (88).

3D printed biomimetic herringbone and helicoid structures were fabricated and tested to failure under compressive loading. Figure 2.10 F shows the 3D printed helicoid (left) and herringbone (right) cylindrical parts. For both structures, the fibers are printed with a hard polymer and the matrix with a soft elastomer. The samples were subsequently

coated with paint to obtain a random black-and-white speckle pattern for posteriori 3D digital image correlation (3D-DIC) analysis. The experimental load vs. displacement experiments allow large deformations in the matrix and fibers (Figure 2.10 G), which ultimately leads to a relatively more compliant herringbone structure as compared with the helicoidal specimen. This is due to the fact that the sinusoidally-arranged fibers within the 3D printed mimics straighten upon compression. Additionally, experiments show that the herringbone structure has better energy absorption capabilities than the helicoid motif. Both curves show a local maximum in stress at ε_1 and ε_2 for the helicoid and herringbone structures, respectively. This local maximum corresponds to critical applied strain where significant damage is observed. The fact that $\varepsilon_1 < \varepsilon_2$ suggests that the herringbone structure is capable of withstanding large strains without significant damage leading to a higher absorbed energy density. The values are 0.35 $J \cdot m^{-3}$ and 1.20 $J \cdot m^{-3}$, for the helicoid and herringbone structures, an increase of 3.43 times. 3D DIC of each sample at an applied strain of 0.1 (Figure 2.10 H) shows more strain localization in the helicoidal structure. On the other hand, the herringbone structure exhibits much lower and distributed strains, which also enables the material to withstand localized damage and efficiently transfer momentum to the surface it is striking.

2.4.5 High-load nanoindentation and FE simulation of the impact surface

High load nanoindentation in combination with FE simulation was also used to ascertain the role of the nanoparticulated impact surface on the mechanical response of dactyl club exocuticle. Figure 2.12 A shows a dark-field optical micrograph of a polished

sagittal section of the dactyl exocuticle with a corresponding schematic, highlighting the nanoparticle-based impact surface interfacing with the herringbone structure within the impact region. High load indentation was conducted within the impact surface and the impact region using an embedded dactyl club polished in the coronal direction through the impact region. SEM observations (Figure 2.12 B) of quasi-static indentations to peak loads of 100 mN, 500 mN, and 1000 mN within the impact surface (top row) and impact region (bottom row) showed clear differences in the deformation and fracture behavior. Indents within the impact surface layer generally feature a high degree of pile-up surrounding the faces of the indent. This pile-up behavior was not observed within the impact region (i.e., with the impact surface removed); in general, we saw smooth faced plastic-looking indents with minimal cracking within the impact region. We note that the cracks observed in the bottom row of Figure 2.12 B within the impact region were the result of inadvertent stresses introduced during polishing and were not, in fact, the result of indentation. However, cracking is observed within the impact surface for all three indents. Similar pile-up behavior has been attributed to shear-band localization and that the impact surface consisted of an oriented fluorinated apatite rod-like microstructure through which the shear induced cracking led to the rotation and sliding of crystallites (105; 106).

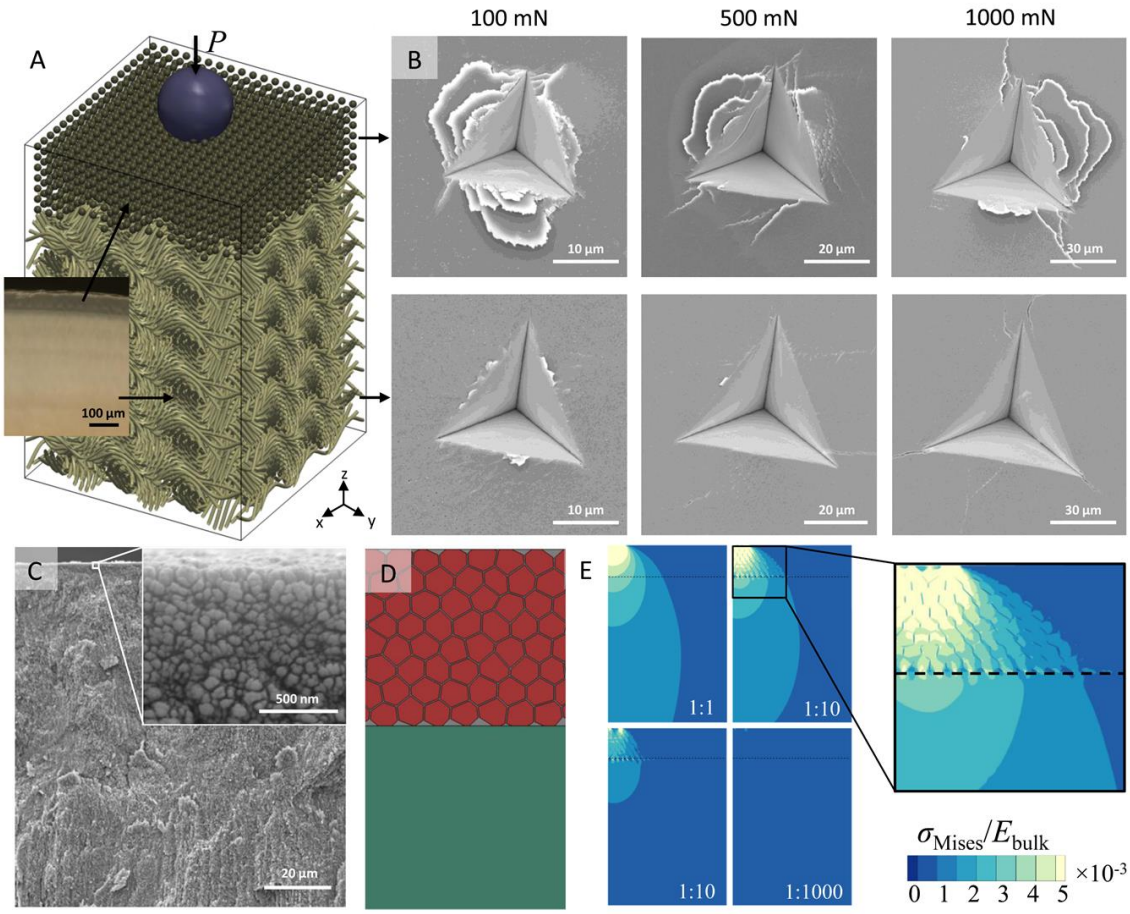

Figure 2.12. High load nanoindentation and FE Simulation of the impact surface particulate layer. (A) Three dimensional schematic of the impact region and impact surface showing the particulate layer placed on top of the herringbone structure. Inset: dark field optical micrograph of the corresponding area. (B) SEM micrographs of high-load indents placed within the impact surface and the impact region to peak loads of 100 mN, 500 mN, and 1000 mN. (C) SEM micrographs of the impact surface highlighting the nanoparticle morphology. (D) Schematic model for the particulated layer used in the FE Simulation. (E) von Mises Stress in the region highlighted in (D). The particulated region is delimited by the dashed line. The Young modulus ratio between matrix and particle is changed: 1/1, 1/10, 1/100, 1/1000. We can see a confinement of the stress when the ratio between the particles and matrix increases. Figure reproduced from Reference (1).

However, our HRTEM analyses reveal that the particles within the impact surface are single crystalline and isotropic domains that are crystallographically separated. Given that the pile-up behavior is not apparent within the herringbone-structured impact region,

we suspect that the pile-up behavior in response to indentation is the result of meso-scale displacement of the isotropic nanoparticles. This motion may have implications for the redistribution of stress during impact loading. The ability for nanoparticulate layers to plastically deform through particle motion may be critical for preventing stress concentration during impact loading. Without the impact surface, peaks of the underlying herringbone structure would likely serve as sites for stress concentration and potentially crack initiation. Nanoparticulated surface coatings have been observed in other biological composite materials such as the ultra-hard teeth of the chiton, *Cryptochiton stelleri*, a marine mollusk (133). These teeth feature an outermost 2 μm thick layer of densely packed sub-100 nm magnetite particles with no preferred orientation, which cover an underlying rod-like microstructure and provide abrasion resistance (133). The incorporation of ceramic nanoparticles into epoxy polymers used as matrix materials for fiber-reinforced composites has also been shown to improve the toughness as well as Young's modulus of the polymer (134-136). The extent of plastic deformation of the epoxy is enhanced so as to dissipate more energy in regions surrounding the crack tip (134; 135).

FE simulations were used to examine the effect of the nanoparticles of the impact surface (Figure 2.12 D, E) on the mechanical response of the dactyl club exocuticle. A SEM micrograph of the impact surface and schematic model used for FE simulation are shown in Figures 2.12 C and D, respectively. The model consists of a 70 μm thick layer of isotropic particles with 88% volume fraction. This layer is placed on top of an isotropic homogeneous substrate. The material properties of the upper layer are chosen to match those of the substrate, using the Voigt homogenization method (137). The simulation was

displacement-controlled, and the images in Figure 2.12 E are shown at 1 μm; the size of the loading region was 10 μm. Figure 2.12 E shows the distribution of von Mises stress for cases where the Young's modulus ratios between the particle and matrix were varied from 1:1, 1:10, 1:100, and 1:1000. The 1:1 case signifies no particles within the outer layer. In the stomatopod, we expect the ratio to be in the range of 1:100 to 1:1000, representing particles that are stiffer than the material between them. We can see that stress is confined within the impact surface layer when the ratio between the Young's modulus of the particles and matrix material is increased, which supports our preliminary hypothesis concerning the role of particles in redistributing stress.

2.5 Conclusions

Here, we uncovered a previously unreported ultrastructural motif within the impact region, featuring a highly ordered compacted and pitch-graded sinusoidal arrangement of helicoidally arranged alpha-chitin fibers mineralized with highly textured apatite mineral. TEM analysis showed that the apatite crystallites exhibit a preferred orientation parallel to the long axis of the chitin fibers, which imparts mechanical anisotropy. FE analysis and testing of biomimetic 3D printed structures revealed that the herringbone architecture offers an enhancement in stress redistribution and out-of-plane stiffness in response to compressive loading compared to the helicoidal architecture. Although the FE models did not take into account the pore canal tubule network, we expect that the out-of-plane mineralized fibers in combination with the sinusoidal arrangement of helicoidal in-plane mineralized fibers provides an optimal out-of-plane compressive strength and toughness

necessary for transferring maximum load to its prey while resisting fracture. Additionally, the incorporation of sinusoidal interfaces in the herringbone structure may improve toughness via extending the path length for crack growth, thereby enhancing energy dissipation. We also identified a thin layer of isotropic single crystalline apatite nanoparticles, which cap the impact region and likely provide additional stress redistribution through particle motion.

Chapter 3: Structure-mechanical property relationships and convergent evolution of the mantis shrimp telson

3.1 Background

Mantis shrimp are commonly divided into two types: smashing and spearing. Species of the smashing type (smashers) employ heavily mineralized bulbous club-like appendages to smash through the mechanically tough exteriors of their prey, which include mollusks, crabs, and other shelled organisms with tremendous force and speed (11; 97). Conversely, the spearing variety (spearers) employ slender dactyl structures containing many sharp spines and are used for rapidly piercing and capturing soft-bodied prey such as fish.

In conjunction with the dactyl, stomatopods possess a shield-like segment of abdominal armor called the telson, which can also be used for personal protection during ritualized fighting and specifically grappling with conspecifics (11; 12; 97; 99; 138). The telson structure is common amongst crustaceans and its primary function is to assist in the cardioid escape reaction, whereby rapid abdominal contractions create powerful swimming strokes that thrust the crustacean backwards to escape predators and other threats (139-141). The telson, which combines with the uropods to create the tail fin, contains a high surface area that acts as a paddle for rapid swimming. In the mantis shrimp though, specifically the smashers, the telson takes on more complex agnostic roles. Smasher stomatopods partake in an act called coiling, whereby they curl up and use their telson as a shield to either physically block the entrance to their dwelling place while inside for

cavity defense or absorb the directed impacts from the dactyls of conspecifics during one-on-one combat (12; 97; 99). The telson can endure repeated direct blows from the dactyl clubs of conspecifics without catastrophically failing, which suggests a similarly impressive and robust design. Additionally, observations made by Caldwell seem to suggest that the coiling behavior, i.e. using the telson to withstand directed dactyl strikes, is limited to the smashing type stomatopods (97; 98). It has also been noted that the most cavity-limited species of smashers are not only the most aggressive, but also possess the most heavily armored telson structures (97; 98).

Smasher stomatopods commonly and historically dwell in pre-existing cavities in rock, rubble and coral whereas spearers construct and inhabit burrows in substrates of sand or mud. Due to the limited availability of cavity dwelling places and competition for habitat among conspecifics, it is believed that smashers evolved more complex and intense agnostic behavior in comparison to spearers, which have access to an abundance of substrate and can thus relocate and rebuild their burrows if necessary (97; 98). Thus, it is expected that the telson structures have co-evolved with the intensity of agnostic behavior and damage potential of the raptorial appendage, resulting in smashers possessing more robust and damage-tolerant telsons.

Taylor and Patek examined the mechanical impact properties of the telson from the smashing species, *Neogonodactylus wennerae* (99). Measurements of the coefficient of restitution revealed an inelastic response of the telson structure, thereby allowing it to effectively absorb and dissipate 69% of the impact energy (99). Through μ-CT measurements, varying degrees of mineralization as well as morphological features

including ridge-like regions called carinae were identified within the telson structure, which were hypothesized to impart a combination of stiffness and compliance necessary for energy absorption (99). Details however regarding the ultrastructural features, chemical composition, mechanical properties, and mechanisms underlying the telson's resistance to high-energy impact loading have not yet been uncovered. Recently, Zhang et al. identified a fibrous twisted plywood (Bouligand) microstructure, characteristic of most crustacean cuticle, within the telson of the smashing type mantis shrimp, *Odontodactylus scyllarus* (142). Synchrotron x-ray micro-diffraction was also used to map the three-dimensional alpha-chitin fiber orientation, which revealed texturing corresponding to the helicoidal fiber architecture (142).

3.2 Objectives & hypotheses

The objectives of this work are to uncover and compare the structure-mechanical property relationships of the smasher and spearer stomatopod telsons from *Odontodactylus scyllarus* (peacock mantis shrimp) and *Lysiosquillina maculata* (zebra mantis shrimp), respectively. The multi-length-scale structure, chemical composition, and mechanical properties of the smasher- and spearer-type telsons will be characterized. Fracture will also be induced to identify potential toughening mechanisms within these structures. Such studies will not only reveal important clues as to the role of various ultrastructural features on imparting strength and toughness in biological composite materials, but they will also allow us to draw new conclusions as to role of selective pressures, namely habitat and agnostic behavior, on the evolution of impact-resistant biological armor in stomatopods.

Given the more aggressive behavior and ritualized fighting of smashing mantis shrimp, I hypothesize that the smasher telson is stiffer and more damage-tolerant than the spearer telson. I also suspect that the difference in impact-resistant properties is due to differences in ultrastructural features and composition (e.g., bulk morphology, cuticle thickness, fiber architecture, degree of mineralization, and mineral crystallinity/phase/orientation). I suspect that the smasher telson features a thicker cuticle, a higher degree of mineralization (higher weight fraction), and perhaps more crystalline and/or oriented mineral near the impact surface.

3.3 Materials & methods

Specimens: Smasher and spearer telson specimens were provided from live organisms of *Odontodactylus scyllarus* and *Lysiosquillina maculata* respectively. Organisms were purchased from a commercial supplier and housed and maintained in an in-house sea-water system. Prior to testing, animals were placed in a refrigerator until deceased and dissected thereafter. Molt cycles were carefully monitored and only animals in the inter-molt phase were selected for study. Measurements of bulk length and width were taken from optical images of eight smasher and six spearer telsons.

Optical and electron microscopy: For analysis of polished cross-sections of the telson structures, specimens were initially dehydrated in air at room temperature and then embedded in epoxy (System 2000, Fibre Glast Developments Corporation, USA) and cured at 60°C for 1 hour. Samples were subsequently sectioned along the desired orthogonal plane using a low speed diamond saw (TechCut 4, Allied High Tech Products Inc., USA)

and polished using a manual grinder/polisher (MetPrep 3, Allied High Tech Products Inc., USA) with graded silicon carbide paper and diamond abrasive solutions down to 50 nm grit size. Polished samples were washed in DI water in between steps to prevent cross-contamination and finally washed and sonicated in DI water for 5 minutes to remove any abrasive material from the polished surface. For analysis of fractured sections of the telson, 1-2 mm thick sections of embedded telson were cut using the low speed diamond saw and mechanically fractured by bending along the desired plane. All samples were subsequently sputter coated with a thin layer of platinum and palladium for conductivity and imaged using a scanning electron microscope (XL-30-FEG, Philips, USA or MIRA3 GMU, TESCAN, USA) at 10 kV accelerating voltage. Transmission electron microscopy and selected area electron diffraction were conducted using a TEM (Tecnai12, FEI, USA) operated at 120 kV accelerating voltage. Thin sections, approximately 70 nm thick, for TEM were prepared using an ultramicrotome (XT-X, RMC Boeckeler, USA) and diamond knife (Pelco, Ted Pella, Inc., USA).

Micro-computed tomography: Micro-CT scans of the smasher and spearer telson were acquired using an Xradia 510 Versa (Zeiss, Germany) operated at 70 kV. Reconstruction, volume rendering, and visualization were performed using Amira 3D (FEI, USA) and CTvox (Bruker, USA) software packages.

Energy dispersive spectroscopy: Standardless elemental mapping and analysis was conducted on non-coated polished cross-sections of the telson structures using a field-emission SEM (MIRA3 GMU, TESCAN, USA) operated at 20 kV and a Quantax 400 EDS

system equipped with dual xFlash 6 SSD detectors (Bruker, USA) in low vacuum variable pressure mode. Elemental maps were collected for 10-15 minutes.

Nanoindentation: Nanoindentation mapping within the dried telson cross-sections was performed using a TI-950 TriboIndenter (Hysitron, USA). The spearer telson map featured a 15 by 10 point array with 10 μm spacing between indents. A trapezoidal (5 second load, 2 second hold, 5 second unload) quasi-static load function was used. Indents were made using a diamond cube corner probe and controlled in displacement to a peak depth of 1 μm. The smasher telson map consisted of a 33 by 7 point array with 10 μm spacing between indents. A similar trapezoidal (5 second load, 2 second hold, 5 second unload) quasi-static load function was used. Indents were made using a diamond cube corner probe and controlled in displacement to a peak depth of 500 nm.

Compression testing and 3D printing: Compression tests on bulk telson segments were performed using an ElectroForce 3200 Series III mechanical tester (Bose, USA). Telson structures were compressed between two steel parallel plate fixtures. A pre-load of 20 mN was applied to ensure contact before testing. Telson structures were compressed to 500 μm relative displacement at a rate of 10 μm/s for a total of 5 cycles. Hydrated samples were left in artificial sea water for 6-12 hours and removed immediately preceding testing. Dried specimens were washed in DI water and left to dry in air at room temperature for 6-12 hours before testing. 3D printed telson cross-sectional mimics were compressed to 1 mm relative displacement at a rate of 2 μm/s. Pre-loads of 50 mN were applied to the samples to ensure contact with the parallel plate fixtures prior to testing. Biomimetic structures mimicking the 2D cross-sectional curvatures of the smasher and spearer telson

were 3D printed using a desktop stereolithography printer (Form 2, FormLabs, USA) with a clear methacrylate-based photopolymer resin. CAD files of the telson cross-sectional geometries were modeled using SolidWorks (Dassault Systèmes, France). These files were then used for 3D printing.

Powder X-ray diffraction: Powdered telson samples were prepared using a mortar and pestle. Phase identification was determined using an x-ray diffractometer (Empyrean, PANalytical, Almelo, The Netherlands) with Cu-Kα radiation with a generator voltage of 45 kV and tube current of 40 mA. The scan range was set from 10° to 70° (2θ).

Thermogravimetric analysis: Powdered telson samples approximately 10 mg by mass were placed in a clean alumina crucible and examined in a combination thermogravimetric/differential scanning calorimetry analyzer (SDT Q600, TA Instruments, USA) against a clean alumina reference pan. TGA/DSC were run under inert argon atmosphere with a flow rate of 100 mL/minute. The run included a 10 minute isothermal hold at room temperature followed by a ramp at 5°C/minute to 1200°C and then a steady ramp back down to room temperature.

3.4 Results & discussion

3.4.1 Optical microscopy & macro-morphological features of the telson

Bulk specimens as well as polished cross-sections were initially examined by optical microscopy to identify macrostructural features of the smasher and spearer telsons. Figures 3.1 and 3.2 present an overview of these macro-morphological features. Figures

3.1 A and 3.2 A show representative body plans of the smasher (*O. scyllarus*) and spearer (*L. maculata*) stomatopods, respectively. Dashed regions highlight the raptorial appendage and telson. Optical microscopy of the dissected smasher and spearer dactyls (Figures 3.1 B and 3.2 B, respectively) show the drastic differences in morphology. We note the hammer-like and comb-like nature of the smasher and spearer dactyls, representative of their utility in smashing through hard-shelled prey and impaling and capturing soft-bodied prey, respectively. Dorsal views of the corresponding dissected telson structures are similarly shown in Figures 3.1 C and 3.2 C, respectively. The two telson structures are similar in overall size. Both have comparable widths (23.5 ± 3.3 mm vs. 20.6 ± 3.3 mm for smasher and spearer, respectively); however, the smasher telson is slightly longer (26.9 ± 4.0 mm) than the spearer telson (20.2 ± 3.2 mm). Comparison of the aspect ratio (length/width) thus reveals a longer slenderer smasher telson (1.14 ± 0.04) and a more square spearer telson (0.98 ± 0.02).

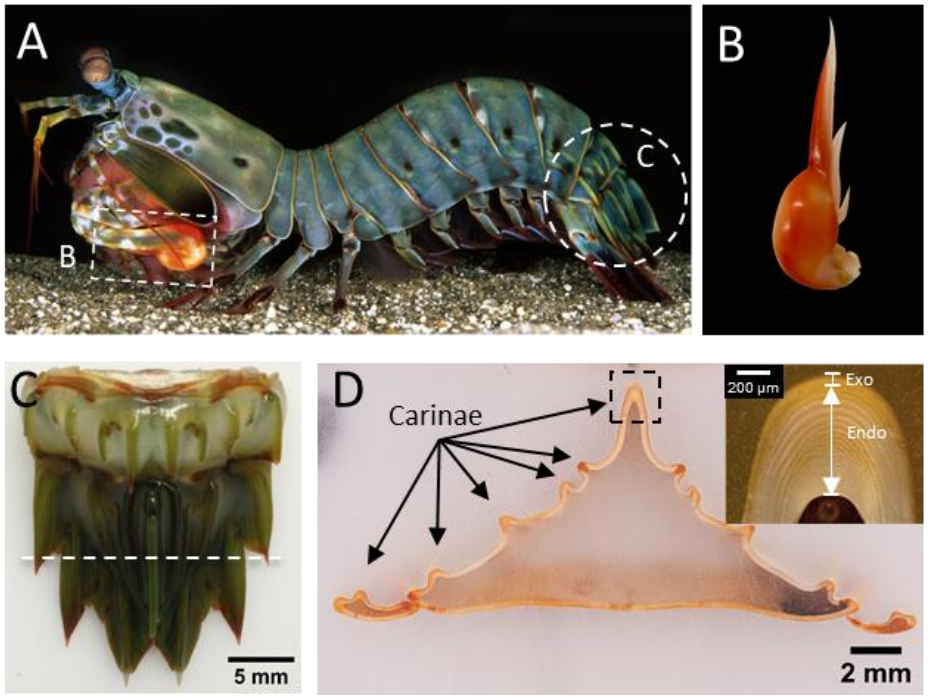

Figure 3.1. Smasher telson overview & bulk morphology. (A) *O. scyllarus* (smashing type stomatopod) highlighting the raptorial appendage and telson. (B) Hammer-like dactyl appendage of *O. scyllarus*. (C) Telson segment of *O. scyllarus.* (D) Polished transverse cross-section of the smasher telson. Plane of section denoted by dashed line in (C). Inset showing higher magnification optical micrograph of dorsal cuticle along the medial ridge (dashed box). Panel *A* reproduced from Reference (11).

Noticeable differences in the telson bulk morphologies are also apparent. The smasher telson features many ridges on is dorsal surface. These ridges, which are called carinae, terminate into sharp spines at the posterior edge, some of which have noticeable teeth (Figure 3.1 C). Conversely, the spearer telson has a fairly simple, smooth and rounded bulk morphology, lacking any well-defined carinae; although, some short and less-developed spines are apparent at the posterior edge (Figure 3.2 C). Both smasher and spearer telsons can be used, in combination with spines found on the adjacent uropod structures, in an offensive effort to stab or push away conspecifics during agnostic

interactions (97). However, the presence of more pronounced spines in the smasher telson reflects an evolutionary history of more intense agnostic interactions between the Gonodactylidae. Cross-sectional analysis of the smasher telson along the transverse plane (Figure 3.1 D) reveals the highly contoured and concave morphology of the cuticle, with carinae lining the dorsal surface (denoted by black arrows). A unique feature of the telson

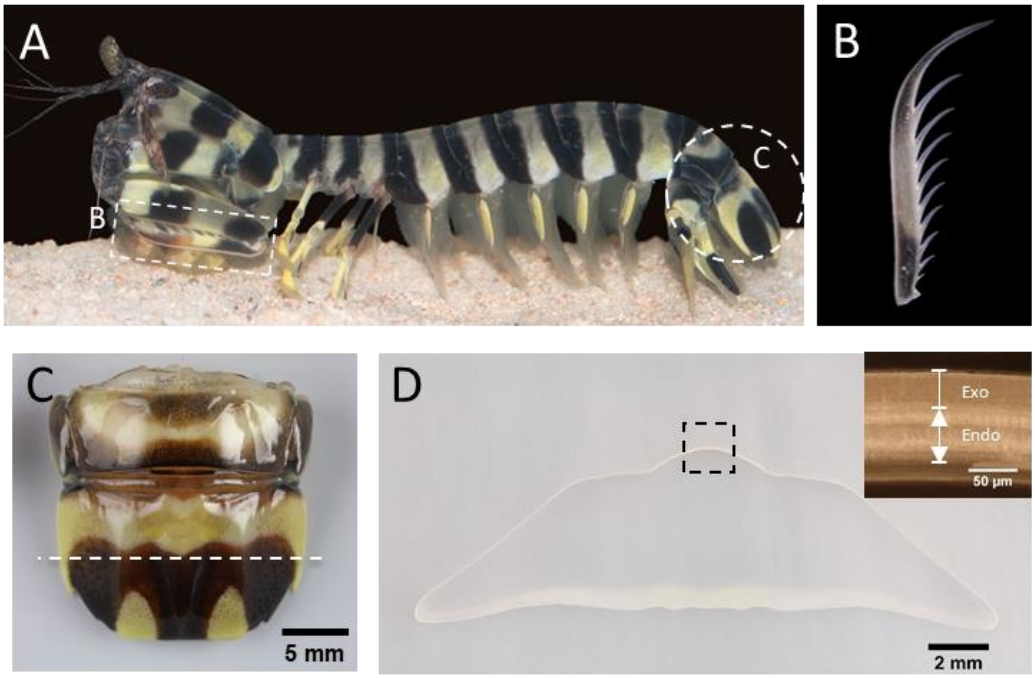

Figure 3.2. Spearer telson overview & bulk morphology. (A) *L. maculata* (spearing type stomatopod) highlighting the raptorial appendage and telson. (B) Comb-like dactyl appendage of *L. maculata*. (C) Telson segment of *L. maculata.* (D) Polished transverse cross-section of the spearer telson. Plane of section denoted by dashed line in (C). Inset showing higher magnification optical micrograph of dorsal cuticle along center line (dashed box).

from *O. scyllarus* is its pronounced medial carina, which is the largest carina and is located along the mid-plane. By comparison, the spearer telson cross-section (Figure 3.2 D) shows a simple convex geometry, which lacks any high curvature regions along the dorsal surface

due to the lack of carinae. A single broad (high radius of curvature) medial ridge is apparent though in most spearer (*L. maculata*) telsons.

3.4.2 Compositional analysis of the telsons

To determine information about the elemental composition, distribution, and the mineral phases present within the telson structures, a combination of thermogravimetric analysis (TGA), x-ray diffraction (XRD), energy dispersive spectroscopy (EDS) and micro-computer tomography (µ-CT) was used. Figure 3.3 presents the resulting powder diffraction patterns obtained from untreated powdered/ground telson samples (Figure 3.3 A) and those that were annealed in argon 1200°C (Figure 3.3 B). Both untreated telson samples show broad peaks identifying the presence of amorphous or weakly crystalline mineral phases. The XRD data also confirms the high abundance of chitin within each cuticle structure. Upon annealing the smasher and spearer telson structures to 1200°C, a mixture of hydroxyapatite and calcium oxide phases is formed, as evidenced by the XRD spectra shown in Figure 3.3 B. These results suggest that the mineral initially present in the intact telson structures includes an amorphous or nanocrystalline calcium phosphate phase. Moreover, Fourier-transform infrared spectroscopy (FTIR) analysis on powdered telson samples (data not shown here) showed absorption bands corresponding to chitin, calcium carbonate, and calcium phosphate.

Thermogravimetric analysis of smasher and spearer telson samples annealed to 1200°C in inert argon atmosphere (Figure 3.4) reveals that both structures are similar in composition, containing approximately 55-60 wt% mineral, 30% organic matter, and 10-

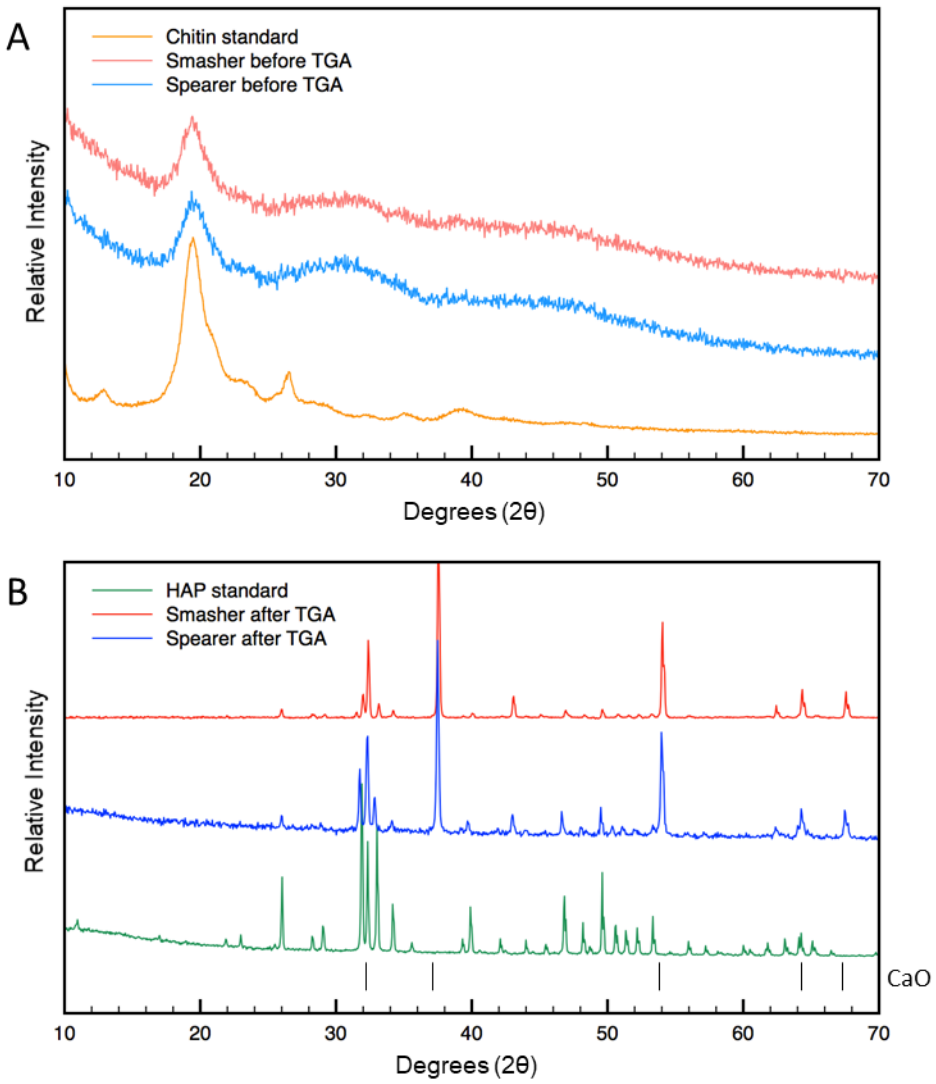

Figure 3.3. Powder x-ray diffraction of ground smasher and spearer telson cuticle. (A) XRD spectra of intact powdered smasher and spearer telsons in addition to commercially available pure chitin. (B) XRD spectra of powdered telson samples after thermal annealing to 1200 °C in inert atmosphere, indicating transition to a mixture of hydroxyapatite and calcium oxide.

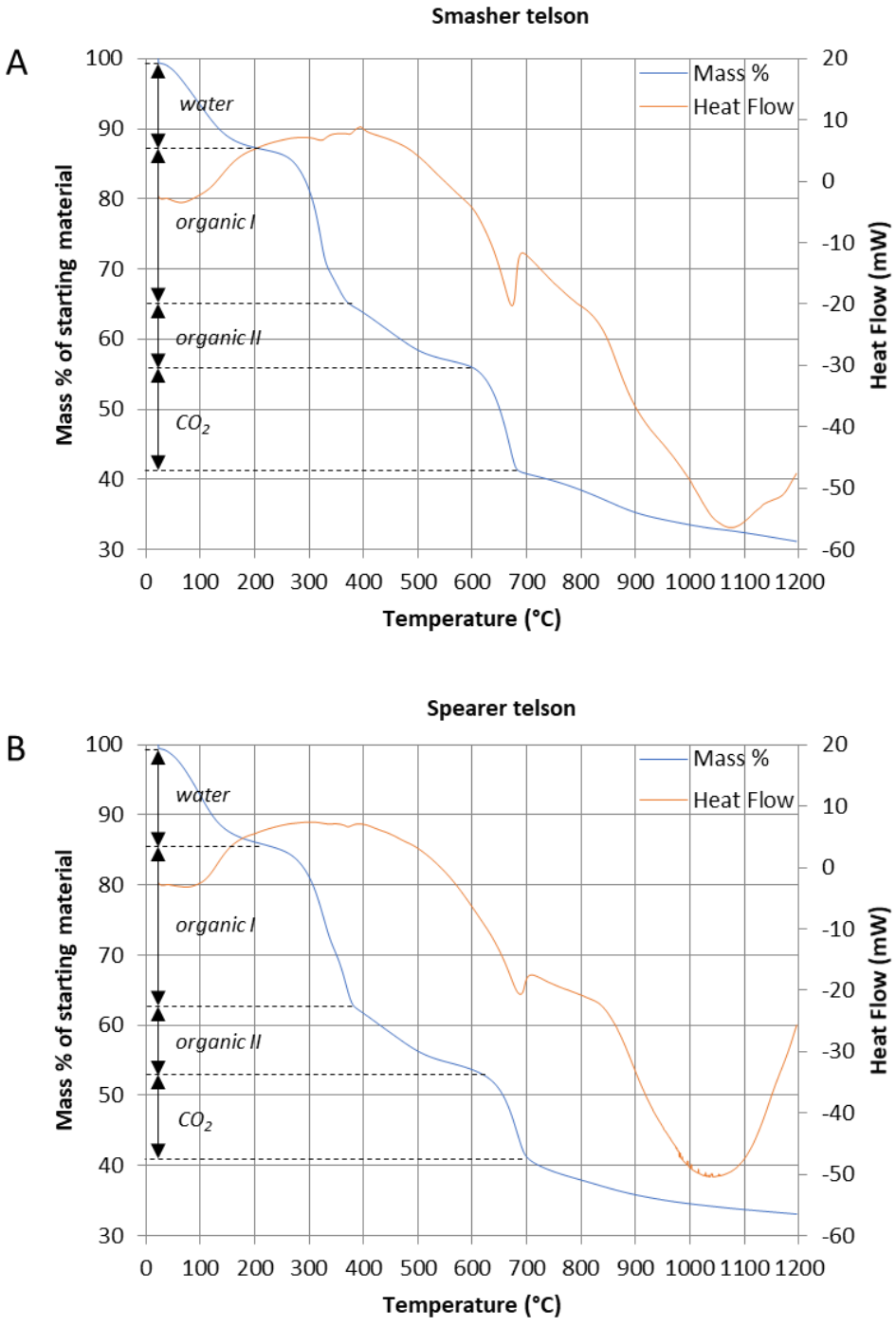

Figure 3.4. Thermogravimetric analysis of powdered telson samples. (A) TGA curve showing mass loss and heat flow versus temperature for a powdered smasher telson sample. (B) TGA curve showing mass loss and heat flow versus temperature for a powdered spearer telson sample.

15% water. We note two distinct decompositions in the range of approximately 300 °C to 600°C, which correspond to the organic matrix and likely two different kinds of organic materials (e.g., protein, polysaccharide).

EDS mapping was used to identify elemental compositions present within each structure. Figures 3.5 and 3.6 show maps of carbon, calcium, phosphorus, and magnesium corresponding to 15-minute collection times within the non-coated transverse cross-section of the smasher and spearer telsons, respectively. The maps confirm that the exocuticle regions of both the smasher and spearer telsons are more heavily mineralized than the endocuticle regions, containing higher concentrations of calcium and phosphorus. While

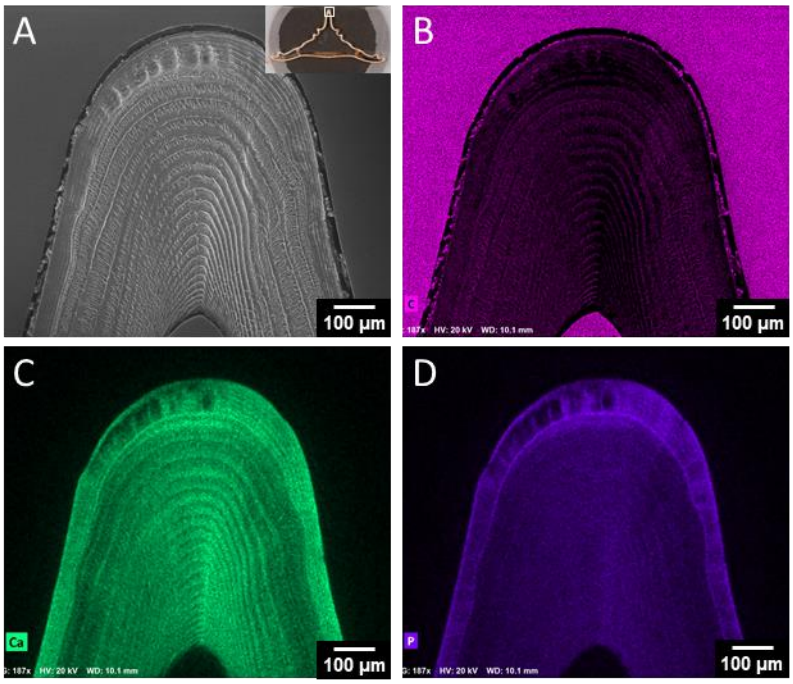

Figure 3.5. EDS mapping of the smasher telson cuticle along the medial carina. (A) Secondary electron SEM micrograph of the medial carina of the smasher telson. Inset showing optical micrograph of the polished transverse cross-section and white box denoting region of interest. (B, C, D) EDS maps showing elemental concentrations and distributions of (B) carbon, (C) calcium, and (D) phosphorus.

the trend is consistent for both telson structures, the difference appears to be more substantial for the smasher telson. The higher degree of mineralization of the exocuticle relative to the endocuticle as compared to the spearer telson may suggest the need for a stiffer outer impact region to provide additional resistance to deformation and/or puncture-resistance from impact. The presence of magnesium in both telsons (data not shown here) also suggests its role in stabilizing amorphous or nanocrystalline mineral.

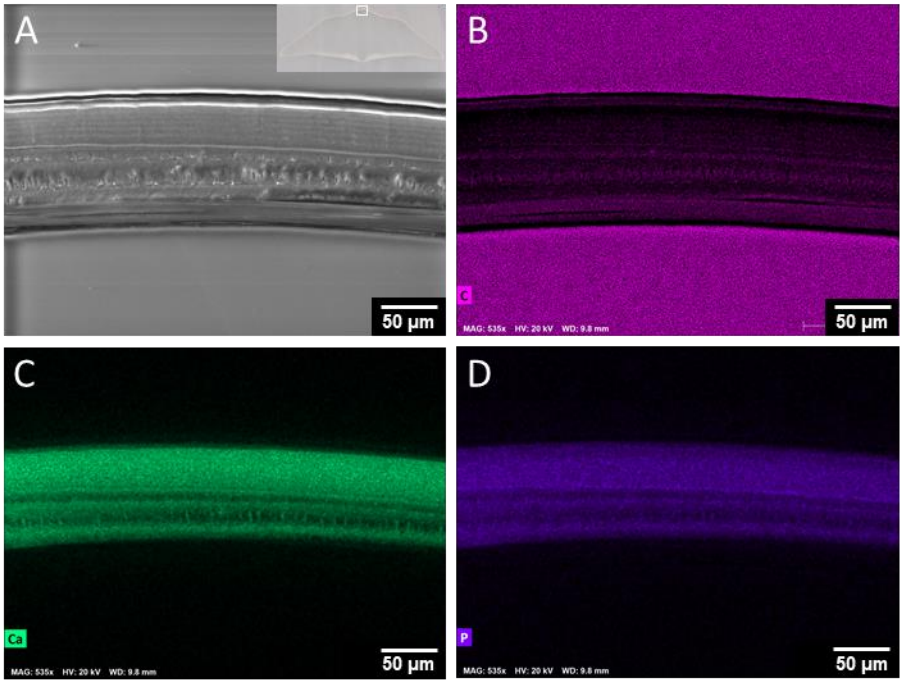

Figure 3.6. EDS mapping of the spearer telson cuticle along the mid-plane. (A) Secondary electron SEM micrograph of the mid-plane dorsal cuticle of the spearer telson. Inset showing optical micrograph of the polished transverse cross-section and white box denoting region of interest. (B, C, D) EDS maps showing elemental concentrations and distributions of (B) carbon, (C) calcium, and (D) phosphorus.

Micro-computed tomography scans of the smasher and spearer telson corroborate differences in degree of mineralization of the exo- and endo-cuticle regions as well as differences in the relative overall cuticle thickness. The µ-CT reconstructions (Figure 3.7)

clearly show a thinner spearer telson cuticle, as evident by higher transmitted x-ray intensity. We also observe higher x-ray attenuation along the center-line of both telson structures, suggesting higher degrees of mineralization in the area where impact would be likely to occur.

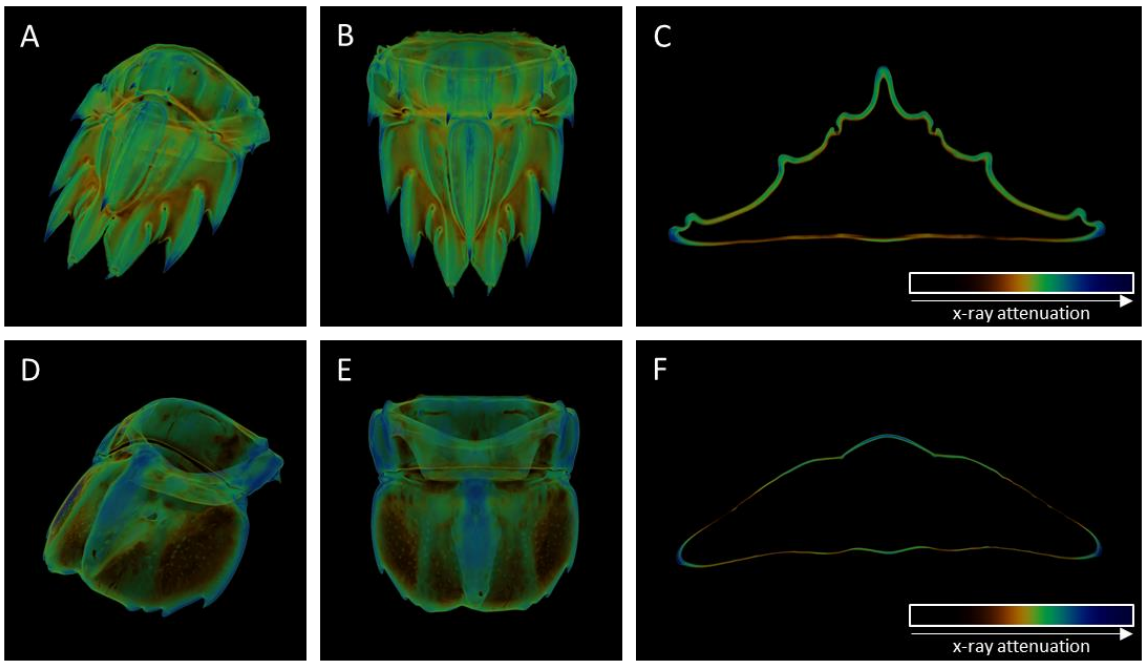

Figure 3.7. Micro-computed tomography of the smasher and spearer telsons. (A) Isotropic view of the CT-reconstructed smasher telson. (B) Front view of the CT-reconstructed smasher telson. (C) Transverse cross-sectional reconstruction of the smasher telson along the mid-plane. (D) Isotropic view of the CT-reconstructed spearer telson. (E) Front view of the CT-reconstructed spearer telson. (F) Transverse cross-sectional reconstruction of the spearer telson along the mid-plane. Scale-bars for the color-coded transfer function shown in insets of (C) and (F).

3.4.3 Micro- and nano-structural features of the telson

Microstructural features of the telson structures were subsequently examined by SEM analysis of fractured and polished cross-sectional specimens. Higher magnification

micrographs of the smasher and spearer telson cross-sections along the mid-line of the dorsal cuticle (insets of Figures 3.1 D and 3.2 D, respectively) show a laminated

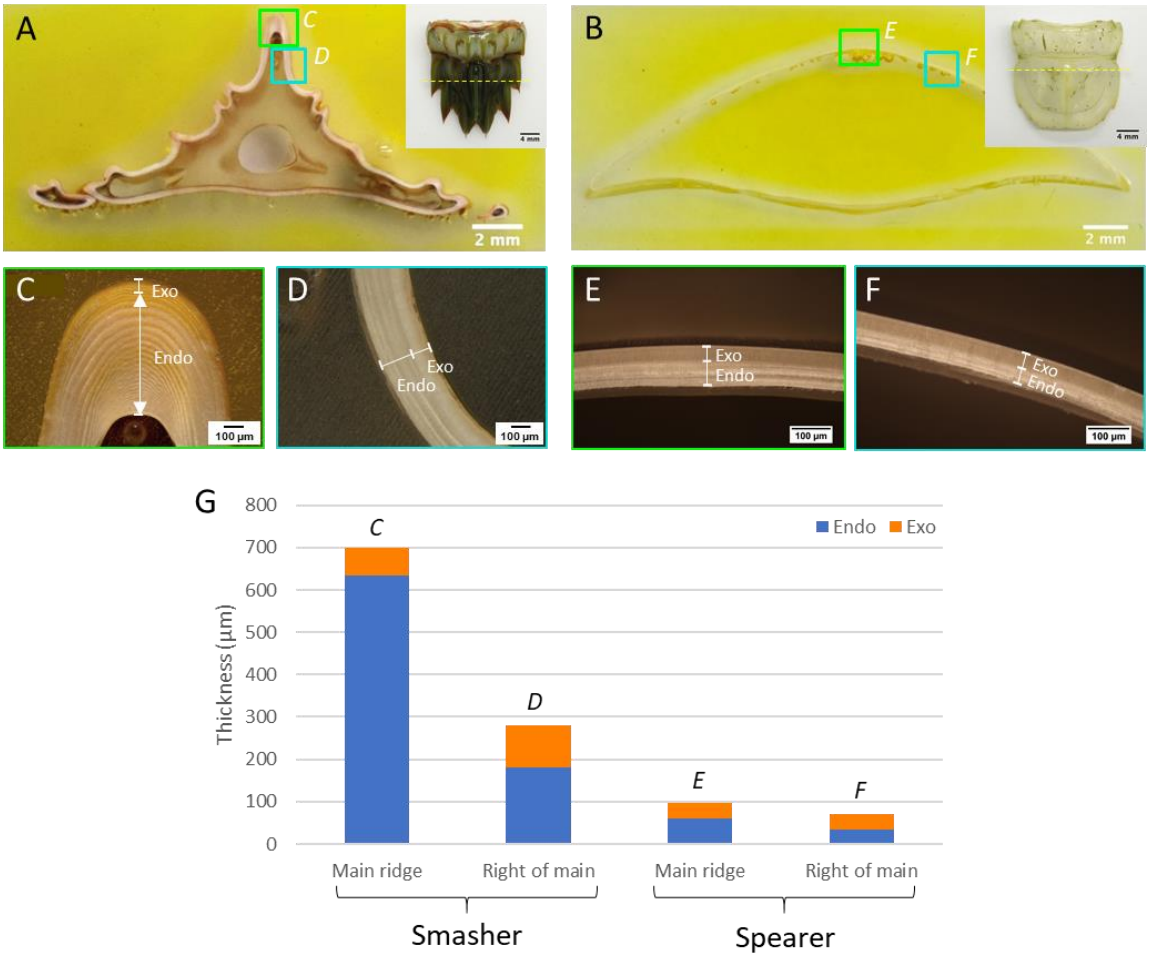

Figure 3.8. Comparison of telson cuticle thickness. (A) Optical micrograph of polished transverse cross-section of the smasher telson. Inset showing plane of section. (B) Optical micrograph of polished transverse cross-section of the spearer telson. Inset showing plane of section. (C) Higher magnification optical micrograph of smasher cuticle along main (medial) ridge. Region denoted in A. (D) Higher magnification optical micrograph of smasher cuticle right of the medial ridge. Region denoted in A. (E) Higher magnification optical micrograph of spearer cuticle along the center-line (main ridge). Region denoted in B. (F) Higher magnification optical micrograph of spearer cuticle right of the main ridge. Region denoted in B. (G) Bar graph showing relative thicknesses of the exocuticle and endocuticle layers within the different regions, denoted in C-F, of the smasher and spearer telson cuticle.

microstructure, which is characteristic of the twisted plywood architecture of fibers found within most crustacean cuticle (108; 117; 122; 143-145). Measurements of the local cuticle thicknesses in various areas of the smasher and spearer telson cross-sections were taken for comparison (Figure 3.8). The highest cross-sectional thickness for both smasher and spearer telsons was located at the medial dorsal region of the cuticle (approximately 700 μm and 100 μm, respectively). In general, the smasher telson has a substantially higher (approximately 2-7 times) cuticle thickness than the spearer telson in any one region. While the spearer telson has a fairly uniform cross-sectional thickness (approximately 80-100 μm) (Figures 3.8 E, F), the smasher telson shows much more variation in cuticle thickness (Figures 3.8 C, D). Ridged (carinae) regions are generally thicker than non-ridged areas of the cuticle, with the highest thickness always along the medial carina (approximately 500-700 μm). Noticeable differences in the relative thicknesses of exo- and endo-cuticle regions are also apparent comparing the smasher and spearer telsons (Figure 3.8 G). Along the smasher medial carina, the endocuticle makes up 90% of the total cuticle thickness compared to 62% in the spearer telson. In non-ridged regions (i.e., right of the telson center-line), the relative thickness of endocuticle drops to 64% and 48% for the smasher and spearer, respectively. This begs the question as to the relationship between the relative thicknesses of exo- and endo-cuticle layers as well as overall cuticle thickness in specific regions of the telson and the structure's ability to absorb energy and withstand impact loading. This topic will be discussed further in section 3.4.7.

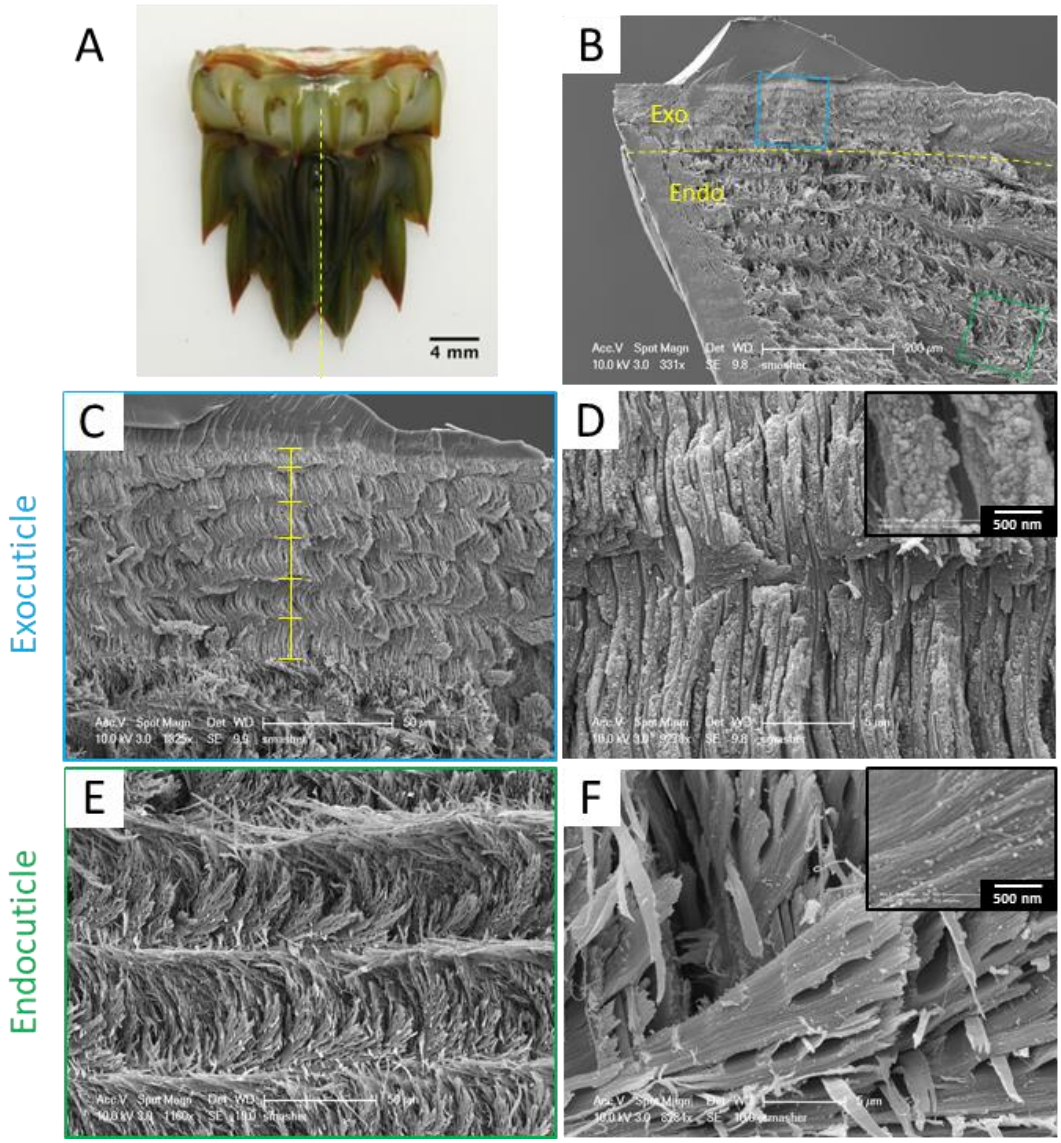

Figure 3.9. Microstructural features of the smasher telson. (A) Optical micrograph of the smasher telson with dashed line denoting plane of fracture. (B) Low magnification SEM of fractured surface. (C) Higher magnification of exocuticle region denoted in (B) (blue box). Yellow hash marks denote periods of rotation of the Bouligand microstructure. (D) Higher magnification of the exocuticle region showing mineralized fibers rotating in the plane of the page. Inset shows grainy surface of mineralized fibers. (E) Higher magnification of the endocuticle region denoted in (B) (green box). (F) Higher magnification of endocuticle region showing pore canal fibers interspersed between rotating fibers. Inset show smoother surface of fibers as compared to exocuticle region.

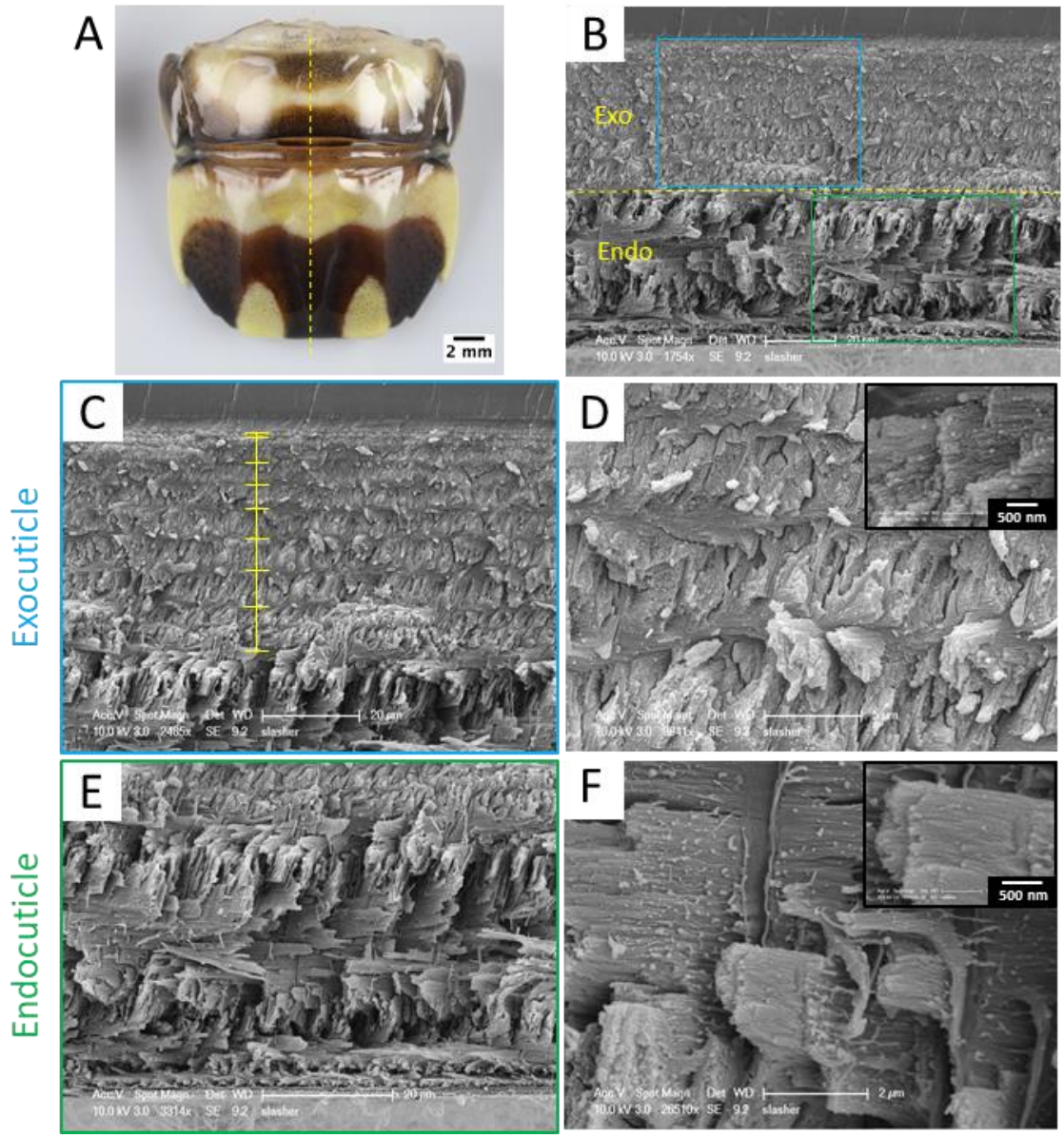

Figure 3.10. Microstructural features of the spearer telson. (A) Optical micrograph of the spearer telson with dashed line denoting plane of fracture. (B) Low magnification SEM of fractured surface. (C) Higher magnification of exocuticle region denoted in (B) (blue box). Yellow hash marks denote periods of rotation of the Bouligand microstructure. (D) Higher magnification of the exocuticle region showing mineralized fibers rotating in the plane of the page. Inset shows grainy surface of mineralized fibers. (E) Higher magnification of the endocuticle region denoted in (B) (green box). (F) Higher magnification of endocuticle region. Inset show smoother surface of fibers as compared to exocuticle region.

Smasher and spearer telsons were subsequently fractured along the sagittal plane to interrogate microstructural features of the cuticle. Scanning electron microscope (SEM) micrographs of the fractured smasher and spearer telson surfaces (Figures 3.9 and 3.10, respectively) reveal that both telson structures feature the twisted plywood (Bouligand) arrangement of alpha-chitin fibers, characteristic of most arthropod cuticles. Figures 3.9 B and 3.10 B show low magnification SEM micrographs of the fractured smasher and spearer telsons, respectively, along the medial dorsal cuticle. Unidirectional alpha-chitin fiber sheets are stacked and rotated about an axis normal to the cuticle surface producing the helicoidal architecture. Pore canal tubule fibers, also composed of alpha-chitin, interpenetrate the in-plane helicoidal fibers and are aligned normal to the cuticle surface (out-of-plane). These fibers serve as conduits for the transport of mineral species for resorption and deposition of mineral during periodic molting. They also provide structural reinforcement and can enhance the toughness of the cuticle through mechanisms such as crack deflection, which will be discussed later. Horizontal lines from the micrographs in Figures 3.9 C and 3.10 C correspond to one full period of rotation of fibers. We define the pitch length as the distance for one 180° rotation of fiber layers. Both smasher and spearer telson cuticles show denser packing of fiber layers within the exocuticle (Figures 3.9 C, 3.10 C, respectively) compared to the endocuticle (Figures 3.9 E, 3.10 E, respectively), which is a common structural trait across the arthropod cuticle.

The exocuticle of the smasher telson (Figure 3.9 C) appears to contain approximately 6 densely packed periods of rotation. High resolution imaging of a set of fiber bundles within the smasher exocuticle (inset, Figure 3.9 D) shows that large granules

are contained on the surface of the fibers, which most likely correspond to the mineral phase. Examination of the endocuticle (Figure 3.9 E) shows the common twisted plywood appearance, which is characteristic of the Bouligand structure. High resolution imaging within the smasher telson endocuticle (Figure 3.9 F) reveals the presence of pore canal tubules, which interpenetrate the rotating fibers of the Bouligand structure and are aligned normal to the telson surface. In contrast to the fibers within the exocuticle, the fiber bundles within the endocuticle appear smooth, suggesting a lower degree of mineralization (inset, Figure 3.9 F), which was corroborated by EDS analysis (see Figure 3.5).

Examination of the spearer telson exocuticle (Figure 3.10 C) reveals that there are approximately 8 periods of densely packed rotating fibers. Closer examination of the exocuticle fiber bundles shows similar granular material on the surface corresponding to a mineral phase (inset, Figure 3.10 D). Interestingly, inspection of the spearer telson endocuticle reveals that there are only two periods of rotation and the fiber bundles appear to be spaced out fairly broadly (Figure 3.10 E). Closer inspection of the endocuticle fiber bundles reveals smooth fibers suggesting once again a lower degree of mineralization (Figure 3.10 F).

Although both smasher and spearer telson structures feature the Bouligand microstructure characteristic of the arthropod cuticle, key differences exist comparing the total thickness, number of Bouligand pitches, and gradients in pitch length amongst the smasher and spearer telson microstructures (Figure 3.11). Line plots comparing the pitch length gradient through the exo- and endo-cuticle regions of the smasher and spearer telson (corresponding to the SEM micrographs in Figures 3.11 A and 3.11 C, respectively) are

shown in Figures 3.11 B and 3.11 D, respectively. In one set of representative samples, the smasher telson features six periods of rotation within the exocuticle, with a pitch length increasing from the cuticle surface from approximately 7 µm to about 18 µm at the exo-/endo-cuticle interface. The pitch length continues to increase within the endocuticle, reaching a maximum pitch distance of approximately 50 µm before gradually decreasing to approximately 5 µm. A total of about 25 Bouligand periods exist within the endocuticle,

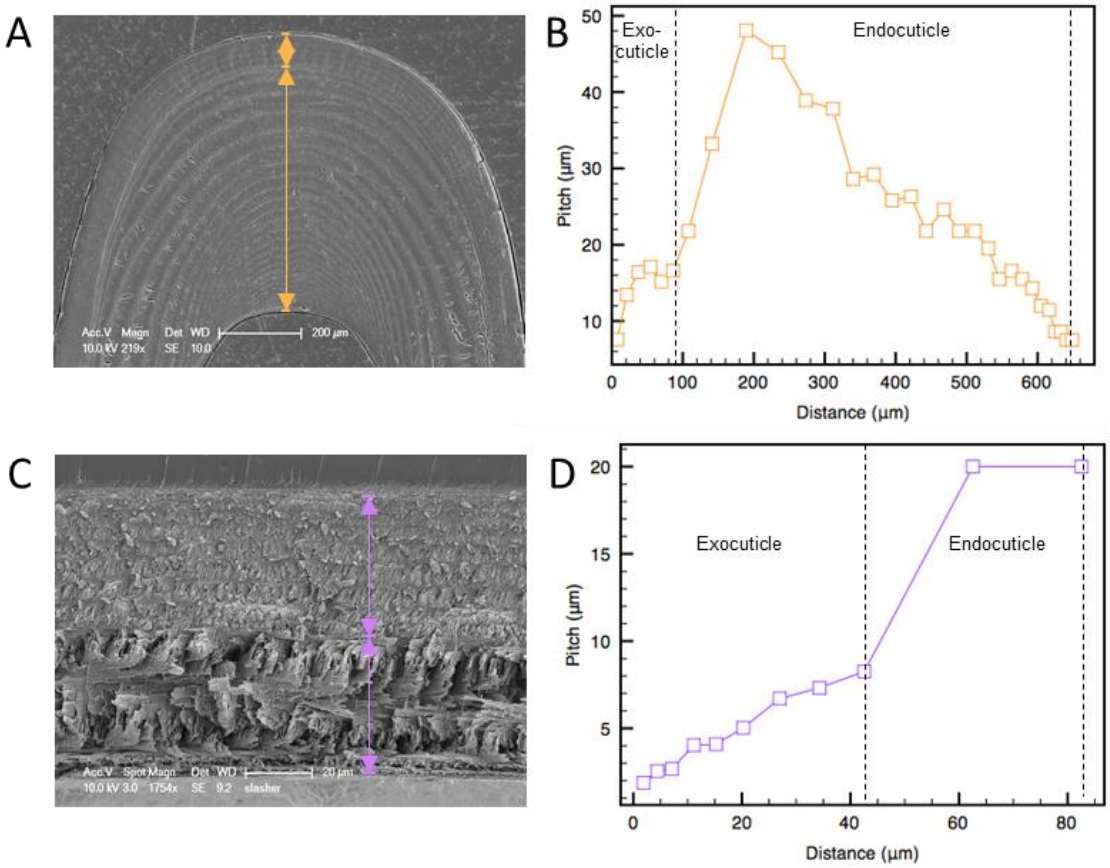

Figure 3.11. Comparison of pitch gradients within the smasher and spearer telsons. (A) SEM micrograph of a polished transverse section of the smasher telson along the medial carina. Arrows denote location of measurement and interfaces between exocuticle and endocuticle. (B) Line plot showing pitch length as a function of distance from the dorsal surface of the smasher telson. (C) SEM micrograph of fractured transverse section of the spearer telson along the mid-plane. Arrows denote location of measurement and interfaces between exocuticle and endocuticle. (D) Line plot showing pitch length as a function of distance from the dorsal surface of the spearer telson.

demonstrating a smooth gradient in pitch within the endocuticle. By comparison, the spearer telson features a similarly densely packed exocuticle with 9 periods of rotation and a pitch length increasing from approximately 2 μm at the cuticle surface to about 8 μm at the exo-/endo-cuticle interface. However, the spearer telson endocuticle only features two Bouligand periods within the endocuticle, both of which have a pitch distance of approximately 20 μm, demonstrating the lack of a well-defined pitch gradient. Although the smasher telson has fewer periods of rotating fibers within the exocuticle than the spearer telson, the smasher telson features a more highly developed endocuticle, which may contribute additional energy absorption during impact as well as localized stiffening to resist deformation upon impact.

Transmission electron microscopy on microtomed thin (<100 nm) sections of the smasher and spearer telson was performed (Figure 3.12) to characterize the nano-structural and crystallographic features of the cuticles. Bright field TEM within the smasher and spearer exocuticle regions along the mid-plane reveals the nested arc laminated pattern, characteristic of the Bouligand architecture of fibers (Figures 3.12 A and C). High magnification imaging reveals that the mineralized alpha-chitin fibers are approximately 44.4 ± 5.7 nm in diameter. We can observe and distinguish the interpenetrating pore canal tubule fibers, which are oriented normal to the telson surface, from the rotating fibers (Figures 3.12 B and D). Selected area electron diffraction within the exocuticle regions of the smasher and spearer telsons reveals very diffuse rings indicative of amorphous or poorly ordered mineral phase (insets, Figures 3.12 B and D). SAED within the exocuticle region shows a most intense, yet still diffuse diffraction ring corresponding to a d-spacing

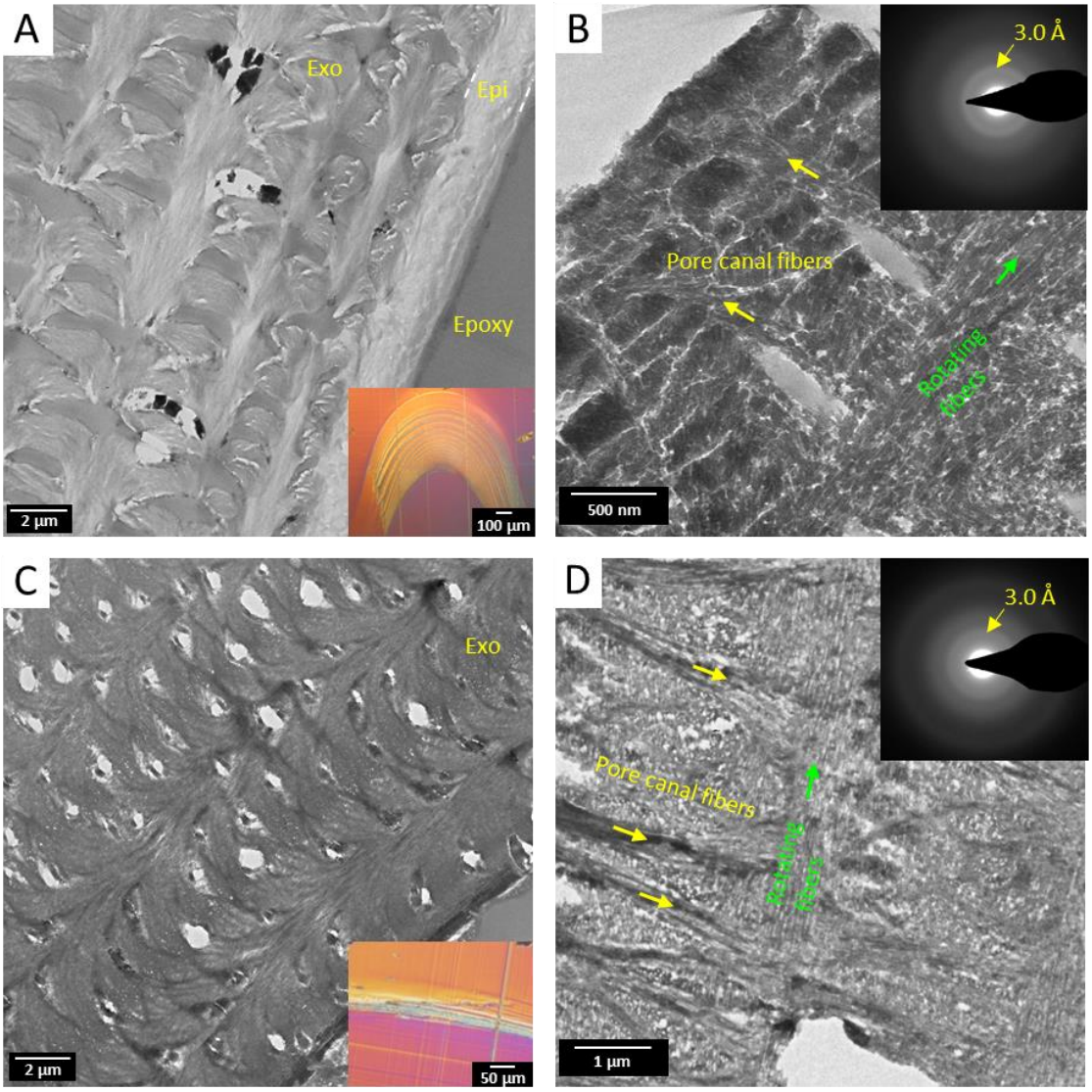

Figure 3.12. TEM analysis of the smasher and spearer telson. (A) Bright-field TEM of the smasher exocuticle near the telson surface. Inset showing optical micrograph of microtomed area, which is along the medial carina. (B) High magnification within the exocuticle showing pore canal tubule and rotating fibers. Inset diffraction pattern showing nanocrystalline mineral. (C) Bright-field TEM within the spearer telson exocuticle. Inset showing optical micrograph of microtomed area, which is along the center-line. (D) High magnification within the spearer telson exocuticle showing tubule and rotating fibers. Inset diffraction pattern showing diffuse rings signifying weakly crystalline mineral.

of approximately 3.0 Å, which correlates with the calcium carbonate or calcium phosphate peak from powder XRD and indicates that the mineral is nanocrystalline and randomly

oriented. Lower d-spacing diffraction rings observed likely correspond to the alpha-chitin fibers. A slightly more diffuse diffraction ring (larger full width at half-maximum intensity) at 3.0 Å observed in the spearer telson lamella (inset, Figure 3.12 D) as compared to that of the smasher telson lamella (inset, Figure 3.12 B) may indicate that the smasher telson features more crystalline (larger grain sized) mineral.

3.4.4 Nano-mechanical properties of the telson

To compare the nanomechanical properties of the telson structures, nanoindentation mapping was performed on polished transverse cross-sections. Figure 3.13 shows the results of indentation maps along the second lateral carina and center-line of the smasher and spearer telsons, respectively. Both smasher and spearer telsons show gradients in reduced elastic modulus and hardness across the exo-/ endo-cuticle interface, which are consistent with the elemental trends from EDS mapping. The reduced elastic modulus and hardness are highest within the exocuticle (approximately 6-8 GPa and 0.3-0.45 GPa, respectively for the smasher telson) (Figures 3.13 C and D). Properties reach a minimum within the endocuticle of approximately 2 GPa and 0.1 GPa, respectively. Nanomechanical properties within the spearer telson (Figure 3.13 G and H) are similar to those of the smasher telson, with a slightly higher range of elastic modulus. Reduced elastic modulus and hardness range from approximately 2-14 GPa and 0.1-0.5 GPa, respectively. The change in mechanical properties however between the exo- and endo-cuticle regions of the spearer telson is less apparent. While the reduced modulus map shows somewhat of a trend

of decreasing modulus from the exocuticle to the endocuticle, no apparent gradient is observed within the hardness map. This contrasts with the smasher telson, which shows a

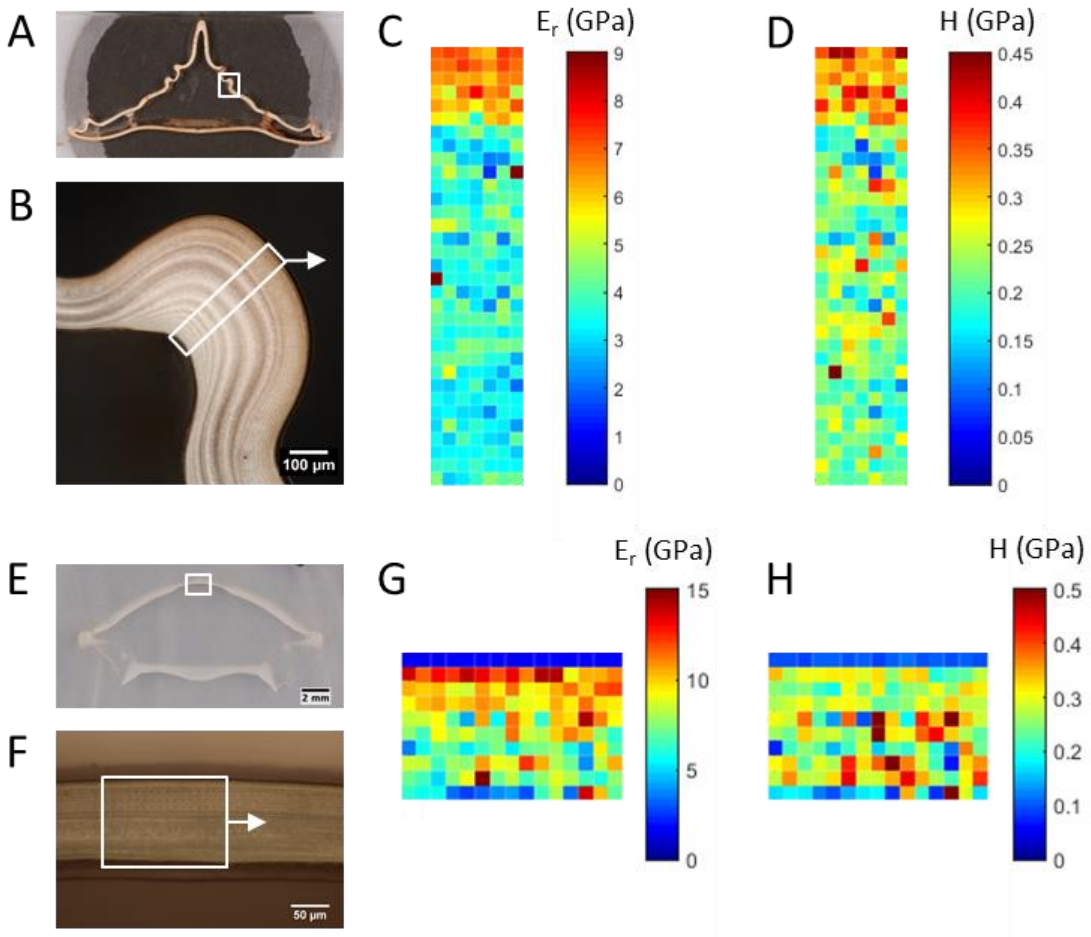

Figure 3.13. Nanoindentation mapping of the smasher and spearer telsons. (A) Optical micrograph of the polished transverse cross-section of the smasher telson. (B) Higher magnification optical micrograph of second lateral carina from boxed area in (A). Boxed region in (B) denotes the area for nanomechanical mapping. (C, D) Results of nanoindentation mapping of the boxed region in (B) showing reduced elastic modulus (C) and hardness (D). (E) Optical micrograph of the polished transverse cross-section of the spearer telson. (F) Higher magnification optical micrograph of center-line dorsal cuticle from boxed area in (E). (G, H) Results of nanoindentation mapping of the boxed region in (F) showing reduced elastic modulus (G) and hardness (H).

sharp increase in elastic modulus and hardness transitioning from the endocuticle to the exocuticle region. This may also be consistent with the EDS maps, which show a more

pronounced gradient in concentration of calcium and phosphorus across the exo- and endo-cuticle regions in the smasher telson than in the spearer telson.

3.4.5 Macro-morphological effects on the mechanical response of the telson

Quasi-static compression testing was performed to assess and compare the strength and stiffness of the bulk smasher and spearer telsons. Hydrated and dried telson specimens were loaded in a parallel plate configuration and compressed cyclically to a controlled displacement of 500 μm at a rate of 10 μm/s. Telson samples were also cut, using a razor blade, along the flexible soft tissue separating the two segments of the bifurcated telson, which we call here the anterior and posterior telson segments. This was done to also compare their load bearing capabilities to assess if either segment plays a larger role in the overall stiffness response of the structure. Figure 3.14 A shows images of the dissected anterior and posterior segments of the smasher and spearer telsons.

Load-displacement results for compression testing of the smasher and spearer telson segments under dried and hydrated conditions are shown in Figures 3.14 B and 3.14 C, respectively. Comparison of the compressive stiffness, measured by the slope of the load-displacement curve, shows that the smasher telson has a substantially higher stiffness than that of the spearer for both anterior and posterior segments under both dried and hydrated conditions. All dried samples show higher stiffness than hydrated samples, as expected. Hydrated biological tissues typically have higher extensibility and lower stiffness as compared to the dry state, due to water's ability to act as a plasticizer by forming hydrogen bonds between the polymer chains of organic fibers.

In addition, posterior segments show higher stiffness than anterior segments within each smasher and spearer telson. This makes intuitive sense since the posterior segments make up most the telson volume and are thus likely to bear the primary loads from attacks from predators and conspecifics. Comparing posterior telson segments, the smasher showed bulk compressive stiffnesses of 14.88 N/mm and 2.69 N/mm under dried and hydrated conditions, respectively, while the spearer telson reported stiffnesses of 0.94 N/mm and 0.36 N/mm, respectively. The stiffnesses of the anterior segments were 5.51 N/mm and 0.45 N/mm for the smasher telson under dried and hydrated conditions, respectively, and 0.29 N/mm and 0.11 N/mm for the spearer, respectively.

Compression testing of 3D printed mimetic telson cross-sections was subsequently performed to assess the role of macro-morphological features of the telson, such as carinae and overall curvature, on the bulk mechanical properties. As we recall from the cross-sectional geometries of the smasher and spearer telsons, the smasher telson features a concave dorsal cuticle, compared to the spearer telson, which features more of a convex geometry. To understand the effect of this curvature on mechanical performance, simplified truss structures were first modeled using a computer-aided design software (SolidWorks) and then 3D printed. Concave and convex parts, featuring the same radius of curvature of the smasher and spearer telson dorsal cuticles, respectively, were modeled in 2-dimensions and then extruded to create a 3-dimenisonal part. A triangular truss structure was also modeled and printed as a control. All parts were designed to be the same height and depth. The 3D printed mimetic structures were compressed to 1 mm displacement, in a parallel plate configuration, at a loading rate of 2 μm/s. The load-displacement curves for

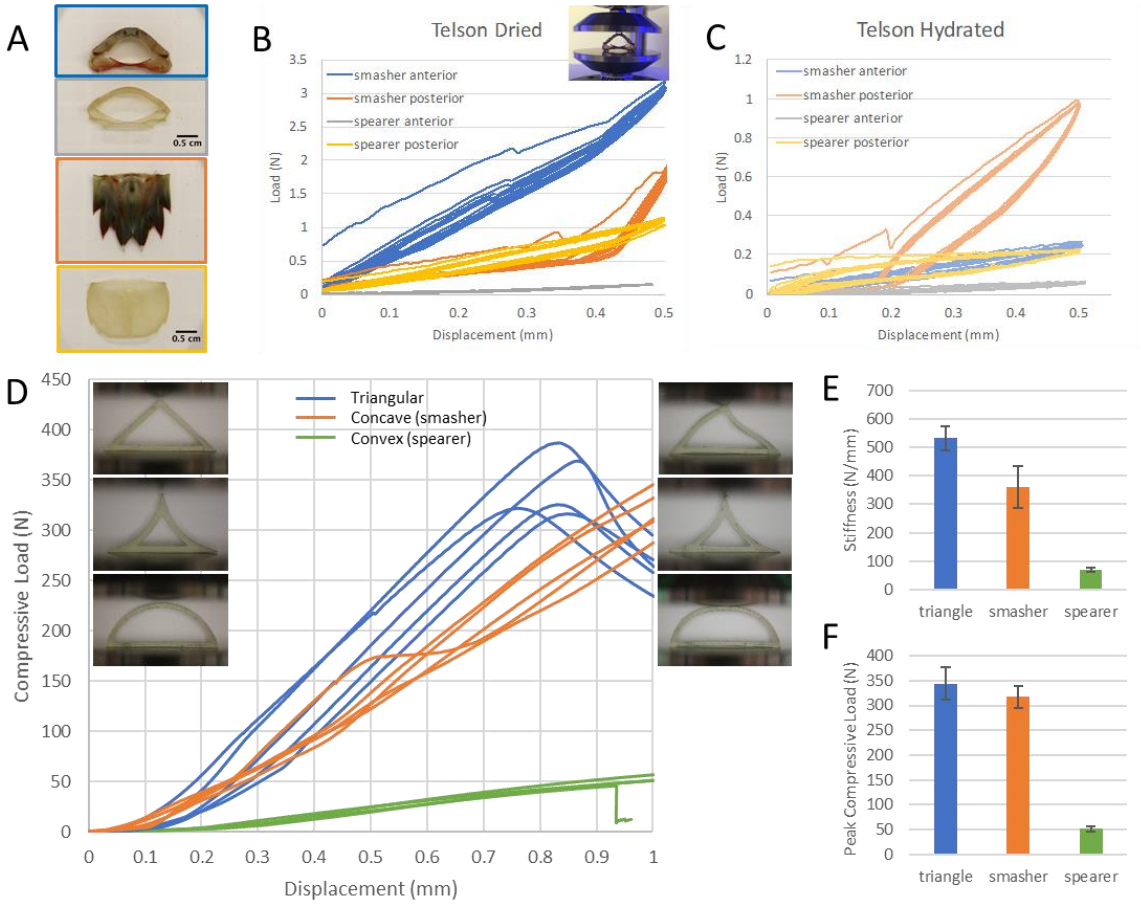

Figure 3.14. Compression testing of natural and biomimetic telson structures. (A) Images of the dissected anterior and posterior segments of smasher and spearer telson (from top to bottom: anterior smasher, anterior spearer, posterior smasher, posterior spearer). (B, C) Load-displacement plots showing results of cyclical compression tests on the smasher and spearer anterior and posterior telson segments under dried (B) and hydrated (C) conditions. (D) Load-displacement curves showing results of compression testing on biomimetic 3D printed telson geometries. Insets show images of the triangle control (top), concave (middle), and convex (bottom) 3D printed transverse cross-sectional geometries before testing (left) and at peak load (right). Notice the buckling of the triangular and convex parts. (E) Bar graph showing average compressive stiffness of the triangle, smasher, and spearer mimetic parts. (F) Bar graph showing average peak compressive load for the triangle, smasher, and spearer mimetic parts.

the smasher and spearer telson mimics as well as the triangular control are shown in Figure 3.14 D. Comparison of the load-displacement data shows that the smasher (concave) telson cross-sectional geometry produces a substantially higher bulk compressive stiffness

compared to concave geometry of the spearer telson mimic: 361.51 ± 73.52 N/mm versus 68.85 ± 6.72 N/mm (Figure 3.14 E). The concave geometry also reaches a peak compressive load (317.46 ± 22.34 N) that is more than six times higher that of the convex geometry (51.40 ± 4.60 N) (Figure 3.14 F). Based on this observation, it is expected that the higher compressive stiffness and load-bearing ability of the natural smasher telson structure can be attributed in part to its concave macro-morphology as compared to the spearer's convex curvature. This is an important design cue that can provide insight to nature's ability impart structural stiffening by varying the macro-morphology of its structures.

3.4.6 Finite element analysis and simulation of the telson under impact

Finite element (FE) simulation was performed on the smasher and spearer posterior telson segments to characterize the distribution of stresses upon compression and impact loading. Figure 3.15 shows the resulting stress distributions in the smasher and spearer telsons as a result of a single impact to the dorsal surface along the medial carina. Isotropic (top) and dorsal (bottom) views of the stress distributions within the bulk smasher (Figure 3.15 A) and spearer telson (Figure 3.15 B) meshes show highest concentration of von mises stresses within the "valleys" adjacent to the medial carinae. This suggests that the valleys, which, as mentioned before, typically have thinner cuticle, are less stiff and can potentially act as dampeners to allow for the telson to deform and thus absorb energy. An adequate combination of stiffness and deformability would be ideal for highest damage-tolerance, which may arise in the smasher telson due it its ridged macrostructure. To better understand

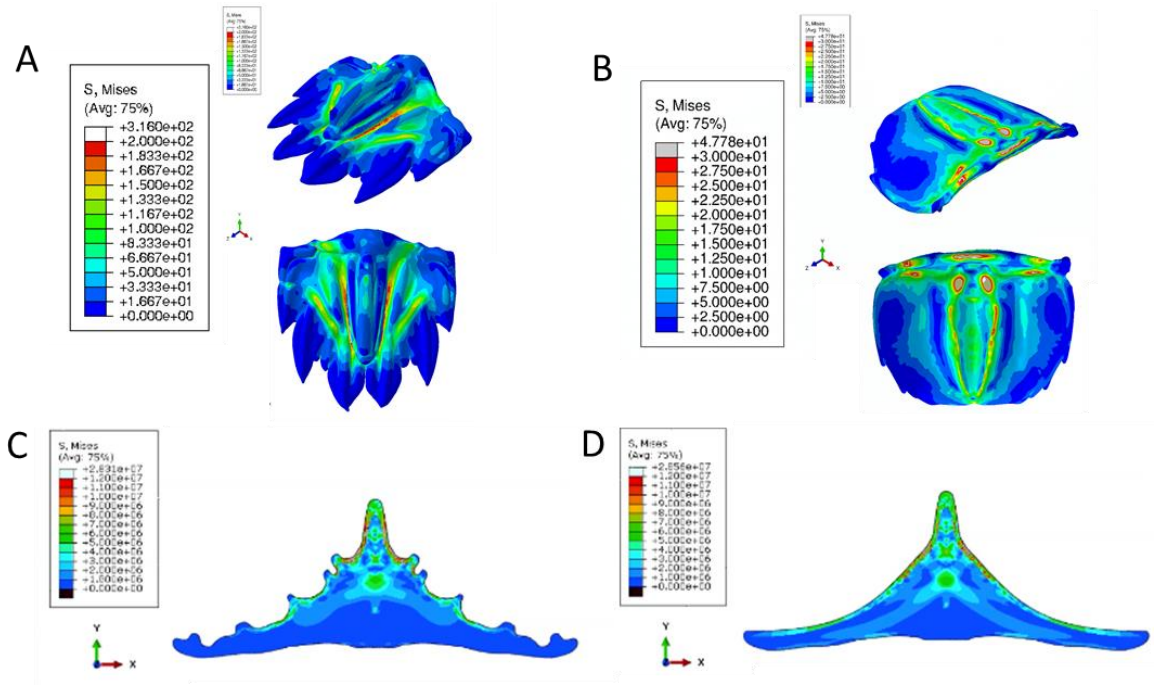

Figure 3.15. FE simulation of stress distributions in the telsons under impact. (A, B) Von mises stress distributions within the smasher (A) and spearer (B) posterior telson segments when subjected to impact normal to the dorsal surface along the center-line. Isotropic and dorsal views of the simulation are shown on the top and bottom, respectively. (C, D) Von mises stress wave propagation within the 2D cross-sectional volume of the smasher telson upon impact to the dorsal surface for the actual geometry (C) and with carinae removed (D), yielding a smooth dorsal surface.

the role of carinae on mechanical performance, FE simulations of stress distributions upon impact were also performed on models of the smasher telson with (Figure 3.15 C) and without (Figure 3.15 D) carinae. The simulations of stress wave propagation through the smasher telson transverse cross-sections show that, in the case where carinae are present, the ridges can act as wave traps retarding wave propagation. Conversely, the model in which carinae were removed, leaving a smooth dorsal surface, shows no evidence of wave retardation. These results are significant and suggest a multifunctional role of the carinae:

mitigating stress wave propagation and allowing the telson to deform to dampen impact energy.

3.4.7 Fracture analysis and toughening mechanisms of the telson cuticle

Characterization of failure processes in materials is critical for understanding and identifying potential mechanisms to resist fracture. Ex-situ compressive loading was thus performed on polished smasher and spearer telson cross-sections to observe crack propagation and identify toughening mechanisms. Figures 3.16 A-D show backscattered electron (BSE) micrographs of a smasher telson cross-section loaded in compression to approximately 10% strain. Highly tortuous cracking is observed along the lateral side of the medial carina (Figure 3.16 A). The inset shows a low magnification BSE micrograph of the cross-section loaded in a compression vice. Higher magnification within the cracked area (Figure 3.16 B) reveals a sinusoidal crack path, which is indicative of a crack twisting failure mode characteristic of the helicoidal fibrous architecture found within the cuticle. By having a rotating crack front, the propagating crack is forced to twist following the local microstructure, which significantly enhances the work of fracture (1; 14; 103). Microcracks branching off the main twisting crack front are also observed, which also improve the toughness of the material by reducing the crack tip stress concentration (3; 17; 120; 146). Fracture is also observed along the valley region between the left first and second lateral carinae (Figure 3.16 C). The cracking pattern is also indicative of a crack twisting failure mechanism. Figure 3.16 D reveals that toughening also exists in the form of crack twisting within the densely packed, more heavily mineralized exocuticle region of the smasher

telson. By comparison, the spearer telson cross-section was loaded to 20% strain and minimal controlled fracture was observed. Examination along the center-line of the dorsal cuticle (Figure 3.17 A) showed minimal cracking with some delamination within the endocuticle. The inset figure shows the low magnification BSE micrograph of the spearer telson cross- section loaded to 20% strain in the compression vice.

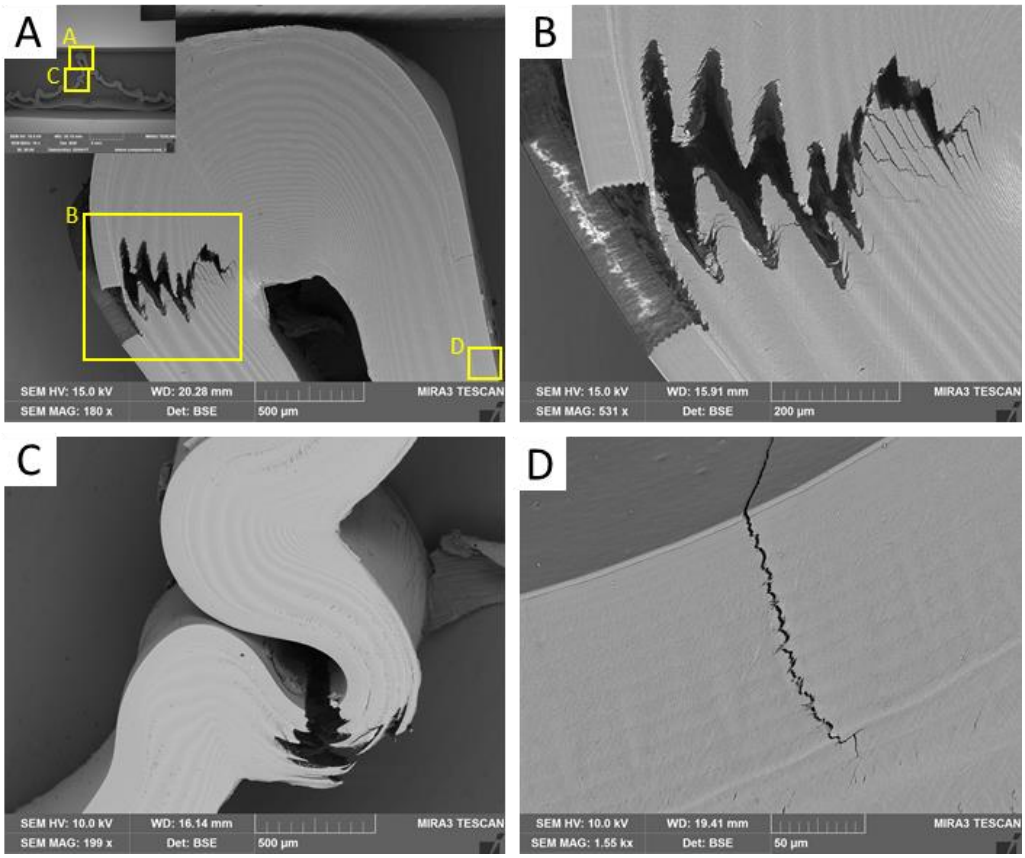

Figure 3.16. Ex-situ compression testing of smasher telson cross-section. (A) Low magnification backscattered electron (BSE) micrograph showing fracture along the lateral side of the medial carina of the smasher telson. Inset shows low magnification BSE micrograph of the overall telson cross-section loaded in the compression vice to 10% strain. (B) Higher magnification of the fractured cuticle from (A) showing sinusoidally twisting cracks within the exo- and endocuticle regions. Microcracks are also observed emanating from the crack front. (C) Catastrophic fracture between the first and second left lateral carina of the smasher telson. A twisted fracture path is also observed. (D) High magnification BSE micrograph within the exocuticle showing a nested arc crack pattern.

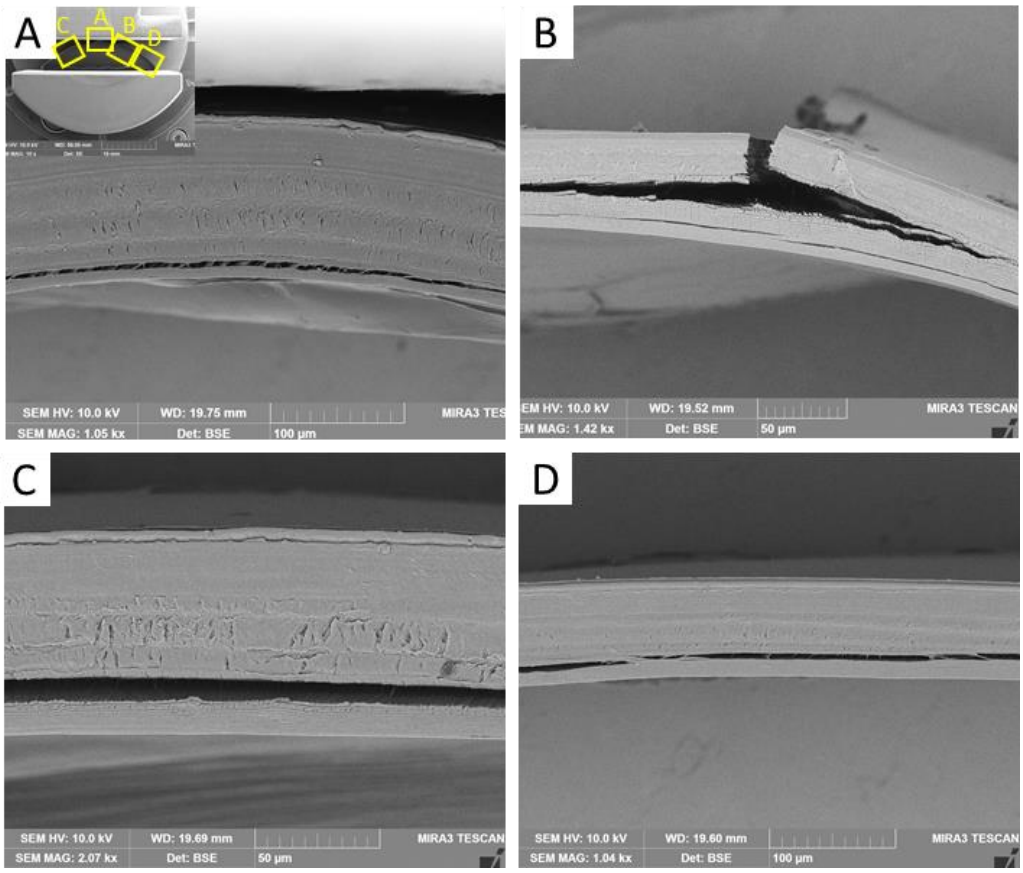

Figure 3.17. Ex-situ compression testing of spearer telson cross-section. (A) BSE micrograph of the spearer telson cuticle near the center-line, loaded to 20% compressive strain. Delamination within the endocuticle is apparent; however, twisting cracks are not observed. Inset showing low magnification BSE micrograph of the spearer telson cross-section loaded in the vice. (B) BSE micrograph of a lateral region of the dorsal cuticle, to the right of the center-line, showing fracture via buckling and longitudinal cracking within the endocuticle. (C, D) BSE micrographs of lateral areas of the dorsal spearer cuticle (shown in inset of (A)) showing delamination within the endocuticle and straight crack paths.

In one lateral area of the dorsal cuticle, fracture was observed (Figure 3.17 B) and is characterized by a fairly non-tortuous crack normal to the cuticle surface through the exocuticle followed by a longitudinal crack traversing the endocuticle. Little evidence of any crack twisting failure mechanisms is apparent in the spearer telson. Other lateral regions of the dorsal cuticle (Figures 3.17 C, 3.17 D) show similar delamination within the

endocuticle without any tortuous crack paths. Additional FE analysis of the principal stresses within the spearer telson cross-section subjected to uniaxial compression (data not shown here) suggests that the region of fracture shown in Figure 3.17 B undergoes predominantly bending stresses, which is consistent with the observed fracture pattern.

Nonetheless, an obvious question arises as to why a crack twisting mechanism is observed within the smasher telson, but not in the spearer telson. One hypothesis is that the differences microstructures, namely the number of Bouligand layers in the exo-/endo-cuticle regions and Bouligand pitch gradient, may be responsible for the different observed fracture mechanisms. As mentioned in section 3.4.3, the smasher telson endocuticle features a smoother pitch gradient in the rotated fibrous structure across the exo-/endo-cuticle interface as well as features more Bouligand layers and a thicker endocuticle region. Previous work by Grunenfelder et al. investigating the effect of inter-ply rotation angle on the impact-resistant properties of biomimetic helicoidal composite laminates as well as mechanical modeling work by Suksangpanya et al. found that certain rotation angles may facilitate a crack twisting mode of failure as opposed to a non-deflected crack propagating across fiber layers (88; 103). Guarin-Zapata et al. also found that certain pitch gradients in laminated helicoidal structures can effectively filter out shear waves from an impact event (104). The lack of a well-defined pitch gradient as well as few Bouligand periods within the endocuticle in the spearer telson may explain why predominately delamination failure modes are observed instead of a highly tortuous crack path.

3.5 Conclusions

In this work we characterized and compared the multi-length scale structure, composition and mechanical properties of the stomatopod telson from two temperamentally- and evolutionarily-different species: *O. scyllarus* and *L. maculata*, of the smashing-type and spearing-type variety. Structure-property relationships were derived to compare and better understand the material characteristics responsible for imparting enhanced damage-tolerance in the telson. The smasher telson reported mechanical properties, such as bulk compressive stiffness and fracture-tolerance far superior to those of the spearer telson. Bulk compressive testing of the telson segments showed substantially higher stiffness in the smasher telson. This enhancement is likely a result of a more sophisticated macro-morphology, namely the higher overall cuticle thickness and a concave geometry. Conversely, the presence of ridge-like structures called carinae impart transverse compliance for energy absorption. This suggests that the evolution of a ridged dorsal surface (i.e., carinae) as well as concave morphology in the smasher telson was an advantageous trait for its use as a defensive structure, requiring adequate stiffness to prevent puncture, yet sufficient compliance to absorb the impact energy.

Corrugation, resembling the ridged smasher telson dorsal surface, has been incorporated into many engineering structures (e.g., cardboard packaging, roofs and flooring, hoses and pipes), as a means of forming lightweight materials that are also mechanically anisotropic, possessing high stiffness transverse to the corrugation direction and compliance along the corrugation direction (147). Corrugated structures are also advantageous in yielding good stability under buckling load, energy absorption from

impact and resistance to shear and compressive loads (147). Questions though remain as to the multifunctional role of the smasher and spearer telson macro-morphologies, such as hydrodynamic drag for improved locomotion or even advantages for digging burrows in muddy or sandy substrates amongst the spearing stomatopods. Such features may be important or necessary for functions aside from self-defense and protection against predators and conspecifics.

The variation amongst smasher and spearer telson microstructural gradients beg the question as to the role of local cuticle thickness and number of Bouligand layers on the local stiffness and energy absorptive properties of the cuticle. A more developed endocuticle and more well-defined pitch gradient in the smasher telson may have evolved in response to more intense agnostic interactions and to prevent damage from dactyl strikes.

The more developed cuticle in the smasher telson, featuring a more well-defined pitch gradient and more periods of rotation allow for effective toughening through crack twisting. This was apparent in the ex-situ compressive loading, which showed torturous crack paths that enhance the work of fracture in the smasher telson compared to straight cracks within the spearer telson. These structural features and resultant mechanical properties reflect the evolutionary history of the stomatopods and the necessity for more damage-tolerant defensive structures in the smashers. Limited availability of coral cavity dwelling places for the smashers led to more aggressive behavior and agnostic interactions amongst the smashers. Smashers with more heavily fortified telsons were likely able to better defend their habitant, ensuring their reproductive success and the proliferation of mantis shrimp with heavily armored telsons. Conversely, an overtly damage-tolerant

spearer telson was likely never necessary. Since the availability of sandy/muddy substrate for dwelling was in high supply, the spearers likely never developed aggressive behavior amongst conspecifics and thus did not necessitate a defensive telson structure.

Nonetheless, there is still much that can still be learned from the diversity of the stomatopod telson. Numerous species have been identified that are highly cavity-restricted, barely ever leaving their homes. These mantis shrimp display heavily armored telsons and even sport defensive features such as long spines that emanate radially from the dorsal surface. Additional research will be required to better understand the role of environmental pressures on the evolution of defensive structures not only within the stomatopods, but other biological organisms as well, with the hope that these insights may provide inspiration for the development of useful engineering tools and structures.

Chapter 4: Mantis-shrimp inspired biomimetic helicoidal composites

4.1 Background

The Bouligand architecture and, more broadly, helicoidal structures of biological origin have been identified as advantageous designs for biomimetic structural materials. Naleway et al. recently identified the helicoidal architecture as one of the eight most common structural motifs among biological materials in a variety of animal taxa and detailed its mechanical advantages (28). The helicoidal design has been identified not only in the exoskeletal structures of arthropods, but also other systems, such as the mineralized collagen layers in osteonal bone, in fish scale dermal armor, and in the cellulose fibrils in wood cell walls (120; 124-126). In fact, the wrapping of the tubule structures in bone osteons and in wood cell walls with helicoidal fiber layers has been found to enhance their torsional and bending rigidity (120; 148). The helicoidal arrangement of fibers provides several toughening mechanisms, leading to enhanced damage tolerance and energy absorption. Because of the anisotropic stiffness of chitin nanofibers, which are stiffer in the *c*-direction (i.e., the long axis) (149), the helicoidal architecture provides inherent elastic modulus oscillation resulting from the periodic nature of the helicoidal microstructure. Such modulus oscillation has been identified via nanoindentation in cross sections of osteonal bone (150), lobster cuticle (122), and the mantis shrimp dactyl club (14). The gradient thus results in reduction in local driving force for crack propagation between layers. Moreover, the modulus difference between the stiff mineral and the soft organic polymer within the mineralized fibers allows for extrinsic toughening in the form of crack deflection at the fiber interface. Fratzl and coworkers showed that for laminated structures

containing mineral–organic interfaces, when the ratio between Young's moduli of the stiff and the soft layer is sufficiently high (greater than five), the soft layers can act as crack arresters (127; 128). Combined with the helicoidal architecture, the result is a crack twisting effect that forces interfibrillar crack propagation along a tortuous helicoidal path, thereby increasing the work of fracture and allowing for high energy dissipation. The crack twisting effect has been observed at the osteon boundaries in bone as well as the mantis shrimp dactyl club, where nested-arced cracks were visualized within the endocuticle region by charge-contrast SEM imaging (14; 146).

Helicoidal reinforcement has also been shown to provide enhanced toughness through the reorientation of fiber layers in response to external loading: Zimmermann et al. used in-situ synchrotron small-angle X-ray scattering to measure the Bouligand-type arrangement of collagen fibril lamellae in the scales of *Arapaima gigas*, a freshwater fish (126). Their measurements showed that the collagen fibril lamellae rotate and reorient in response to tensile loading so as to deform in tension or compression, thus enhancing their ductility and toughness. An additional advantage of the Bouligand design found in arthropod cuticle is enhanced resistance to inter-lamellar delamination resulting from the incorporation of interpenetrating pore canal fibers. Similar to the effect of *z*-pinning in fiber-reinforced composites (151), pore canal fibers aligned through thickness effectively stitch the stacked rotating fiber layers together, providing not only resistance to delamination, but also improved tensile and compressive strength in the direction normal to the cuticle surface. Chen et al. examined tensile properties of the sheep crab cuticle (*Loxorhynchus grandis*) in directions longitudinal and normal to the cuticle surface and

found a high density of pore canal tubules showing necking and ductile fracture, which are thought to play an important role in enhancing toughness in the *z*-direction (117). Moreover, the tensile strength of dried specimens in the longitudinal direction (12.9 MPa) was approximately 50% lower than that in the normal direction (19.8 MPa), where pore canal fibers were directly engaged (117). Additionally, our work (presented here in chapter 2) identified a modified Bouligand architecture within the stiff and hard impact surface region (exocuticle) of the stomatopod dactyl club, which features sinusoidally arranged helicoidal fiber layers as opposed to the traditionally flat sheets found within most arthropod cuticles (1). We determined that this herringbone structure provides improved stress redistribution and strain-to-failure under compressive loading in the normal direction as compared to the Bouligand design because of the flattening of sinusoidal fiber layers. Moreover, through finite-element analysis, it was shown that by varying the aspect ratio (amplitude: wavelength) of the sinusoidal fiber layers, the relative Young's modulus in the loading direction can be increased (1). Guarin-Zapata et al. also showed that periodic Bouligand structures, such as that found within the mantis shrimp dactyl club, can exhibit band gaps at frequencies related to the stress pulse generated during impact loading, thus providing a shear wave filtering effect that enhances energy absorption (104).

Biomimetic efforts to replicate arthropod cuticle have only recently gained popularity, with the majority of reports published within the past few years. Research efforts have focused primarily on taking advantage of one of two kinds of properties of the cuticle, mechanical or optical. Here we focus on structural applications and examine biomimetic composite materials that feature the laminated helicoidal architecture of fibers

characteristic of the arthropod cuticle. We focus on two popular processing techniques for their fabrication, which include fiber-reinforced composite processing and additive manufacturing.

Fiber-reinforced composites (FRCs) are popular structural materials because of their combination of high strength and toughness and are currently found in a wide range of commercial applications, such as aerospace vehicles, automobiles, defensive armor systems, and high-performance sporting equipment. FRCs consist of fibers (reinforcement), typically woven fabrics or unidirectional sheets that are impregnated and embedded in a continuous matrix phase. Because of the wide range of mechanical properties (e.g., tensile strength, Young's modulus, ductility) of reinforcement and matrix materials, FRCs can find great versatility in application. One could imagine FRCs as candidates for cuticle-mimetic materials because of the reinforcement and matrix components being analogous to chitin-protein fibers and biomineral, respectively. Cheng et al. fabricated biomimetic helicoidal laminated composites using glass fiber pre-impregnated with epoxy resin (prepreg) (152). Panels measuring 0.3 m × 0.3 m containing 24 stacked fiber layers (plies) were produced. Single helicoid as well as double helicoid panels were fabricated, featuring continuous inter-ply rotation angles of 7.8° and 16.4°, respectively. An industry-standard quasi-isotropic design, which features a stacking sequence of $[0/-45°/45°/90°]_{3s}$, was used as a baseline control for comparison of mechanical performance (152). The mechanical properties were assessed under flexure and short-beam shear and it was found that the biomimetic helicoidal structures displayed higher flexural stiffness as well considerable increase in residual strength (damage-

tolerance) compared to the baseline (83% for single helicoid, 56% for single helicoid with midplane symmetry, and 23% for double helicoid). Grunenfelder et al. more recently fabricated 48-ply carbon fiber/epoxy biomimetic helicoidal composites by a similar out-of-autoclave prepreg processing route and examined their mechanical response to impact loading (88). Biomimetic helicoidal panels, featuring three different rotation angles, 7.8° (small), 16.3° (medium), and 25.7° (large), were fabricated and compared to unidirectional as well as quasi-isotropic controls (88). The purpose of testing various inter-ply rotation angles of the helicoid was to determine if there is an optimal helicoidal geometry for impact resistance and to understand the mechanical implications of having a graded pitch length throughout the cuticle cross section. Results of the impact testing, using a drop tower test with 100 J of impact energy, showed that each of the helicoidal mimetic composites outperformed the unidirectional and quasi-isotropic controls in terms of dent depth, a measure of surface damage, with the medium rotation angle panel showing a 49% reduction in dent depth compared to the quasi-isotropic control (88). Moreover, the medium- and large-angle panels showed a 16% and an 18% improvement, respectively, in residual compressive strength compared to the quasi-isotropic control. Post-impact ultrasonic imaging revealed internal damage within the composite panels and showed that the biomimetic helicoidal fiber architecture promotes lateral crack propagation as opposed to through-thickness damage that may lead to catastrophic failure (88).

Additive manufacturing, also commonly referred to as 3D printing, is one potential avenue that offers promise of assembling such complex geometries as those found in biological composites. Recently several additive manufacturing techniques have gained

much attention for their ability to achieve high-resolution feature printing and print a wide variety of novel materials (77; 79; 153-162). One example is a technique called direct ink writing (DIW), which is an extrusion-based printing technique that promises the potential to print essentially any material so long as the proper rheology of the desired ink-like material is attained (160; 162). The ink material is extruded in combination with controlled movement of a motorized x, y, z stage, which allows for the construction of a 3-dimensional structure. Direct ink writing has already successfully demonstrated the ability to fabricate a variety of unique structures. Some examples include hydroxyapatite scaffolds for application in replacement human bone tissue (163), free standing thermoplastic polymeric scaffolds (164; 165), graphene aerogel microlattices (155), and even biomimetic synthetic diatom frustules (77).

An acceptable ink for direct ink writing must first meet a set of criteria. First the ink must be non-Newtonian and shear-thinning. For the ink to flow through the syringe nozzle during extrusion, it's viscosity must be able to decrease in response to an applied shear stress. Subsequently, once extruded and the shear stress is removed, the ink material must instantaneously form a free-standing gel/solid. The gel must be able to support its own weight thereafter.

Since chitin is the primary organic component found within the mantis shrimp dactyl and telson, it seems to be an obvious choice for a biomimetic feedstock material; however, chitin has a poor solubility in most solvents. Chitosan on the other hand, which is the deacetylated form of chitin, can be solubilized under aqueous acidic conditions making it a better candidate for an ink material (166). Few cases in the literature have

reported using chitosan inks for direct ink writing. T.H. Ang et al. used chitosan and chitosan/hydroxyapatite (HA) inks consisting of 3 w/v% chitosan, with 0%, 20%, and 40% of the chitosan replaced by HA, in 2% v/v acetic acid. These inks were then printed directly into a bath mixture composed of varying % w/v NaOH and 100% high-grade ethanol mixed in a ratio of 7:3 using a rapid prototyping robotic dispensing system (167). An alternative recipe reported by C.R. Almeida et al. called for 3 w/v% chitosan in 2% acetic acid and dispensing into a bath mixture of 8 w/v% NaOH in 70% ethanol (168). Moreover, the ability to print ceramic materials by direct ink write would be useful for mimicking the inorganic components and structures found within most biomineralized tissues.

4.2 Objectives

The first objective of this work is to fabricate helicoidal biomimetic composites inspired by the structures found within the mantis shrimp dactyl club and telson. Biomimetic materials will be manufactured by two primary routes: traditional layup processing of FRCs and additive manufacturing via direct ink write. The second goal of this work is to perform bulk mechanical testing on the resultant biomimetic structures to assess their performance in comparison to standard geometries and architectures, such as the quasi-isotropic layup used in aerospace structures.

With respect to FRCs, we will specifically fabricate a range of composite materials, featuring carbon, glass, and aramid reinforcement coupled with epoxy and urethane matrix materials. While previous studies in the literature effectively assessed the role of inter-ply rotation angle (88; 152; 169) on the damage-tolerance of helicoidal composites, no studies

have properly investigated the effect of using different reinforcement and matrix materials on the impact performance. As previously mentioned, a sufficient modulus mismatch between the reinforcement and matrix materials is required to facilitate crack deflection at the fiber-matrix interface. Thus, by incorporating different moduli reinforcement and matrix materials into the helicoidal composite laminates, we can effectively assess the ability for crack twisting to occur and quantify the role of not only inter-ply rotation angle, but also reinforcement-matrix modulus mismatch on impact-resistance and damage-tolerance.

We will construct macro-scale helicoidal composites using a vacuum bagging technique with fibers (e.g., glass, carbon, polyethylene) of different moduli, fiber angles (e.g., 8°, 16°, 24°) embedded in epoxy resin and polyurethane matrices. Composites will subsequently be cut and tested using similar methods as reported by Grunenfelder et al. (88) as well as through high strain rate impact testing in collaboration with the Army Research Laboratory in Aberdeen, Maryland. Post-impact damage will be evaluated by microscopy. In parallel, chitosan- as well as various engineering ceramic-based (alumina, mullite) 3D printable inks will be developed. Their rheological properties will be characterized and optimized for additive manufacturing of helicoidal laminate geometries. Ceramic-based 3D printed structures may be sintered and post-infiltrated with polymer resin to create a composite design. Bulk mechanical properties will be measured via a combination of 3-point bend, tensile, and compressive testing.

4.3 Materials & methods

Fiber-reinforced composites processing: Reinforcement used in the composites consisted of dry unidirectional 12K carbon fiber, 406 tex S2 glass fiber, and 336 tex Kevlar® sheets with areal weights of 3.7 oz./yd.^{2}, 4 oz./yd.^{2}, and 3.2 oz./yd.^{2}, respectively (ACP Composites, Inc., USA). The non-woven unidirectional fibers are held in position by a fine spider web of polymer fibrils that coat the surface. Two-part epoxy (Max CLR, Polymer Composites, Inc., USA) and urethane (TAP Quick-Cast, TAP Plastics, USA) resins were used as the matrix materials. Three different helicoidal panels, featuring continuous inter-ply rotation angles of 7.5°, 15°, and 30°, as well as one quasi-isotropic control panel, which features 0°, ±45°, and 90° ply orientations, were fabricated for each of the six unique reinforcement-matrix composite combinations, yielding 24 unique composite designs. Three sets of each unique composite panel, each measuring approximately 215 mm long by 215 mm wide, were fabricated, from which two test coupons, each measuring approximately 102 mm long by 152 mm wide, were obtained. This yielded a total of 144 composite coupons for mechanical testing. It is important to note that, in this study, not all 144 coupons were fabricated and tested due to constraints on time and resources. Details will be provided in section 4.4.

For all composite samples, reinforcement plies were cut to specific angles prior to being laid up. In addition, all composites featured mid-plane symmetry with respect to the ply orientations. This was done to prevent warping of the cured panels due to residual stresses that can develop during the curing process. All composite laminates featured 25 plies of reinforcement. This allowed for one continuous 0° to 90° rotation and counter-

rotation within the 7.5° helicoidal composite, one 180° rotation and one 180° counter-rotation within the 15° helicoidal composite, and two 180° rotations and two 180° counter-rotations within the 30° helicoidal composite.

All composites were fabricated using a wet layup technique, in which dry reinforcement was laid down while wet resin was deposited and squeegeed across the fiber surface. This process was repeated layer-by-layer until all plies were laid up. The wet laminates were placed on top of a layer of non-perforated release film and then covered with a layer of nylon release peel ply and a layer of breather cloth (Fibre Glast Developments Corp., USA). The panels were then vacuum-bagged (<25 in. Hg) and cured in an oven at 60°C for 3 hours. After curing, test coupons measuring approximately 102 mm long by 152 mm wide were machined from the composite panels using a water-jet.

Optical and scanning electron microscopy: Cross-sectional imaging of the panels before and after testing was achieved by first polishing the edges of the samples using progressively finer grit silicon carbide sandpaper down to a grit of 1200 (15 μm). The sample cross-sections were then imaged using an optical microscope (Axio Imager.A2m, Zeiss, Germany) and a scanning electron microscope (MIRA3 GMU, TESCAN, USA) operated at 10 kV accelerating voltage.

Mechanical testing: Prior to testing, the dimensions (thickness and width) of all composite test specimens were measured in multiple areas using calipers, averaged, and recorded. Impact testing was performed in accordance with ASTM D7136 (170), using a drop weight impact testing system (Dynatup, Instron, USA) equipped with hemispherical indenter tip. The drop height and mass were adjusted to deliver an impact energy of 100 J.

During testing, test specimens were fixed in place to a rigid steel base, with a 76 mm x 127 mm rectangular hole in the center, using toggle clamps at the four corners. After impact, the dent depth of each test specimen was measured using a depth gauge and recorded. To assess the residual strength and toughness of the composites following impact, compression-after-impact experiments were performed in accordance with ASTM D7137 (171). Samples were compressed to failure in a material testing system (5500R Model II 25, Instron, USA) using a loading rate of 1.25 mm/min and a combination of 100 kN and 5 kN load cells.

Ink Formulations for Direct Ink Write 3D Printing: Chitosan ink formulations were modified from procedures used by Geng et al. (172) and Almeida et al. (168). Inks were produced by first preparing a 3% (w/v) chitosan (medium MW: 190-310 kDa, 75-85% deacetylated) in 2% (v/v) aqueous acetic acid solution. Solutions were stirred for at least 12 hours to ensure that the chitosan was fully dissolved, and the solution was homogeneous. The coagulation bath medium consisted of 1.5% (w/v) sodium hydroxide in 100% ethanol. The ability to form solid continuous chitosan filaments was first investigated by manually extruding the chitosan solution into the coagulation bath using a syringe pump (PHD 2000 Infusion, Harvard Apparatus, USA) at various flow rates. Once this was achieved, the ink and extrusion parameters were transferred to the 3D printer. Aluminum oxide ink formulations were adapted and modified from work by Rao et al. (173). A 40% (w/v) aqueous solution of poly(acrylic) acid (PAA) was first prepared and stirred to completely dissolve. The PAA solution was then mixed with aluminum oxide powder in a 0.65 g: 1 g ratio in a mix cup to the desired total volume of the ink. Then 50 mg of cellulose

powder was added. The mixture was then mixed in a planetary centrifugal mixer (AR-100, Think USA, USA) for 3 minutes and then left to sit for one hour. Meanwhile an aqueous solution of 10% (w/v) polyethylene glycol (PEG) was prepared. After the ink had rested for 1 hour, the PEG solution was added to the ink in 0.2 g increments and mixed in the planetary centrifugal mixer in between additions, until 1 g total had been added. Finally, aluminum oxide powder was added to the ink in 0.5 g increments and mixed until a rough consistency of peanut butter was attained. The ink was then test extruded manually using a syringe to ensure that a consistent solid self-supporting filament could be printed. Mullite inks were prepared using the same method as for alumina inks; however, instead of using a 0.65 g PAA: 1 g alumina, a 2 g PAA: 1 g ceramic ratio was used, where the ceramic consisted of a 3:2 mass ratio of aluminum oxide: silicon dioxide (fumed silica, submicron-sized spheres fused into highly branched short chains, 0.1-0.2 μm long). In addition, after mixing and before adding PEG, a wait time of 15 minutes was used instead of 1 hour.

3D printing: Chitosan 3D scaffolds were printed using a combination of a custom built direct ink write 3D printer, featuring a three-axis positioning stage (ABL 9000, Aerotech, USA), and a modified commercial delta style printer (DeltaWASP 20 40, WASP, Italy). Ink deposition was controlled using a pneumatic air-powdered fluid dispenser (Ultimus V, Nordson EFD, USA) operating at the appropriate pressure given the selected ink. G-code for printing paths for helicoidal structures were designed and modified using an open-source slicer software (CraftWare, CraftUnique, Hungary).

Post-processing of 3D-printed parts: Ceramic 3D printed parts were post-annealed in air to temperatures up to 1700 °C (according to the heating profile described in section

4.4.6, see Figure 4.14 F) to investigate the ability for particle sintering and part-strengthening.

4.4 Results & discussion

4.4.1 Characterization of the dactyl club as inspiration for biomimetic composites

The periodic helicoidal fibrous microstructure of the mantis shrimp dactyl club served as inspiration for the design of biomimetic helicoidal fiber-reinforced composites. Figure 4.1 shows an overview of the mantis shrimp dactyl club and internal fibrous helicoidal laminated architecture. A physical model representing the arrangement of rotating unidirectional fibrous layers is shown in Figure 4.1D. Previous work by Grunenfelder et al. characterized and quantified the helicoidal pitch gradient within the periodic region of the dactyl club and established that, given a single layer thickness of 1 μm, the dactyl club features inter-ply rotation angles varying from 1.6° in the outermost region to 6.2° within the innermost area of the periodic region (88). Given this information and, to remain consistent and compare our results with previous work, we decided to use inter-ply rotation angles of 7.5°, 15°, and 30°. These larger angles compared to those featured in the natural system were also chosen to allow for the minimum number of plies to produce a full rotation of the helicoidal structure, thereby minimizing a high cost of materials.

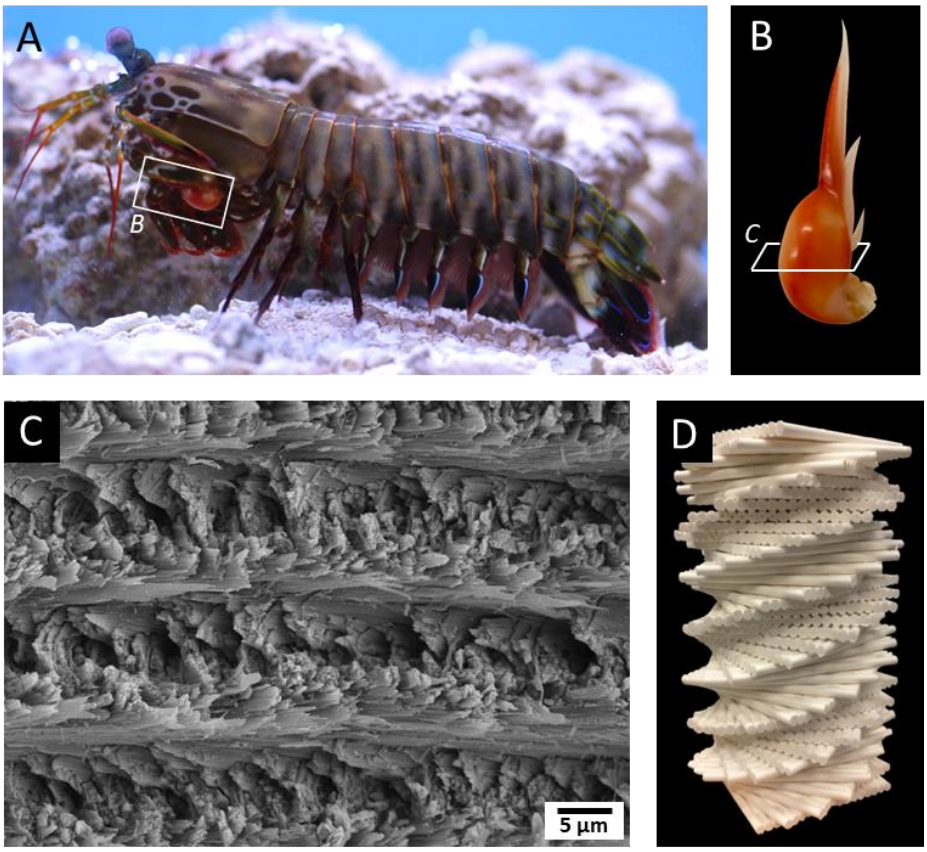

Figure 4.1. Overview of the laminated fibrous helicoidal architecture within the mantis shrimp dactyl club. (A) Image of the peacock mantis shrimp (*O. scyllarus*). (B) Image of the dactyl club. Region denoted in (A). (C) High magnification SEM micrograph of the helicoidal fibrous architecture found within the periodic region of the dactyl club. Plane of fracture denoted in (B). (D) Model of the Bouligand structure showing stacked and rotating unidirectional fiber layers.

4.4.2 Fabrication & characterization of biomimetic helicoidal FRCs

Biomimetic helicoidal composites were fabricated using a wet-layup and vacuum-bagging technique described in section 4.3. Details concerning the layup geometries and fiber orientations within each of the quasi-isotropic and helicoidal composite laminates are shown in Table 4.1. Following fabrication, cross-sectional analysis of the pre-tested

Table 4.1. Composite layup details.

Panel Design	Layup
Quasi-isotropic	$[0/\pm45/90]_{3s}$
Small angle helicoid	$[0/7.5/\ldots/90]_{s}$
Medium angle helicoid	$[0/15/\ldots/180]_{s}$
Large angle helicoid	$[0/30/\ldots/180]_{2s}$

composite panels was performed to assess the quality of the parts and check for any voids or defects. Optical microscopy of the completed panels as well as cross-sections of representative panels are shown in Figure 4.2. Contrast observed in the cross-sections, specifically for carbon fiber reinforced panels (Figures 4.2 A bottom, 4.2 D bottom), corresponds to the different orientations of the fiber layers. Bright layers correspond to in-plane oriented fibers whereas darker layers denote out-of-plane or out-of-normal fibers.

Panel thickness varied between 3 mm and 6 mm, where Kevlar-urethane composites showed the highest thickness. Urethane composites in general tended to have higher post-cured thicknesses, which may be due to the higher viscosity of the mixed urethane resin (2,000 cP) as compared to the epoxy resin (800-1,200 cP) and higher difficulty in removing excess resin using the vacuum system. We note that most panels show good infiltration of the matrix resins into the reinforcement; however, some panels show a few small voids where air bubbles may have become trapped and the matrix resin did not completely infiltrate the fibers.

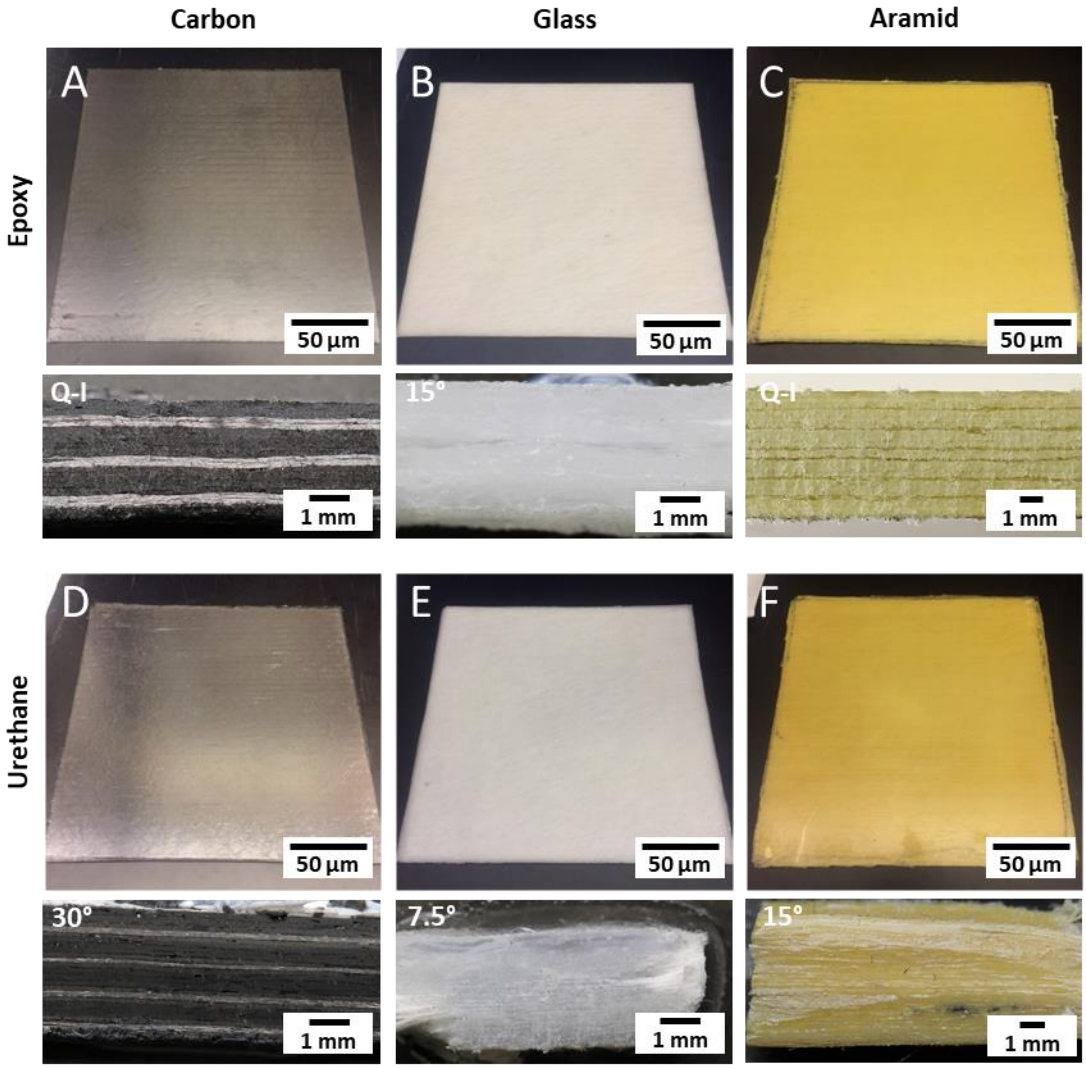

Figure 4.2. Optical microscopy of composite panels and their cross-sections. Top panels show the intact as-fabricated composite laminates and bottom panels show the cross-sections. (A) Carbon fiber-epoxy composite (top) and the cross-section of a quasi-isotropic carbon-epoxy panel (bottom). (B) Glass-epoxy composite (top) and the cross-section of a medium angle helicoidal glass-epoxy panel (bottom). (C) Kevlar-epoxy composite (top) and the cross-section of quasi-isotropic Kevlar-epoxy composite. (D) Carbon-urethane composite (top) and the cross-section of a large angle helicoidal carbon-urethane panel (bottom). (E) Glass-urethane composite (top) and the cross-section of a small angle helicoidal glass-urethane panel (bottom). (F) Kevlar-urethane composite (top) and the cross-section of a medium angle helicoidal Kevlar-urethane panel (bottom).

4.4.3 Impact response of biomimetic helicoidal FRCs

Composite panels were subsequently subjected to drop weight impact with 100 J of impact energy. The load versus time response of each impacted panel was recorded. Figure 4.3 shows plots comparing the impact load as well as energy versus for time data for two representative panels: glass-epoxy large angle helicoid (Figure 4.3 A) and glass-urethane large angle helicoid (Figure 4.3 B). The glass-epoxy panels, and epoxy-matrix composites overall, reach higher peak loads than the urethane composites. This can be attributed to the stiffer nature and higher elastic modulus of the epoxy resin compared to the urethane resin. The sharp drop in load following the first peak load within the epoxy composites signifies the initiation of fracture. Urethane composites do not show a sharp drop in load and rather show a gradual decrease, which may signify that the panels are deforming by flexure as opposed to cracking. Moreover, noticeable ringing is observed in the urethane composite load versus time plots, which arises due to harmonic resonant vibrations initiated within either the load transducer or the panel.

A comparison of the peak impact loads for each of the 24 composite systems is shown in Figure 4.4. Epoxy composites overall show higher peak impact loads than urethane composites. The glass-epoxy composites report the highest peak loads of all the reinforcement-matrix combinations. Although it seems intuitive that the carbon-epoxy composites would report the highest peak loads, due to them possessing the stiffest reinforcement and matrix materials in this study, the higher areal density of the glass fiber reinforcement than carbon fiber reinforcement may mean that there is a higher volume fraction of fibers in the glass composites, yielding a higher bulk stiffness upon impact. In

addition, the quasi-isotropic panels report the highest average peak load within each set, except for the carbon/epoxy. This suggests that the quasi-isotropic design, possessing the

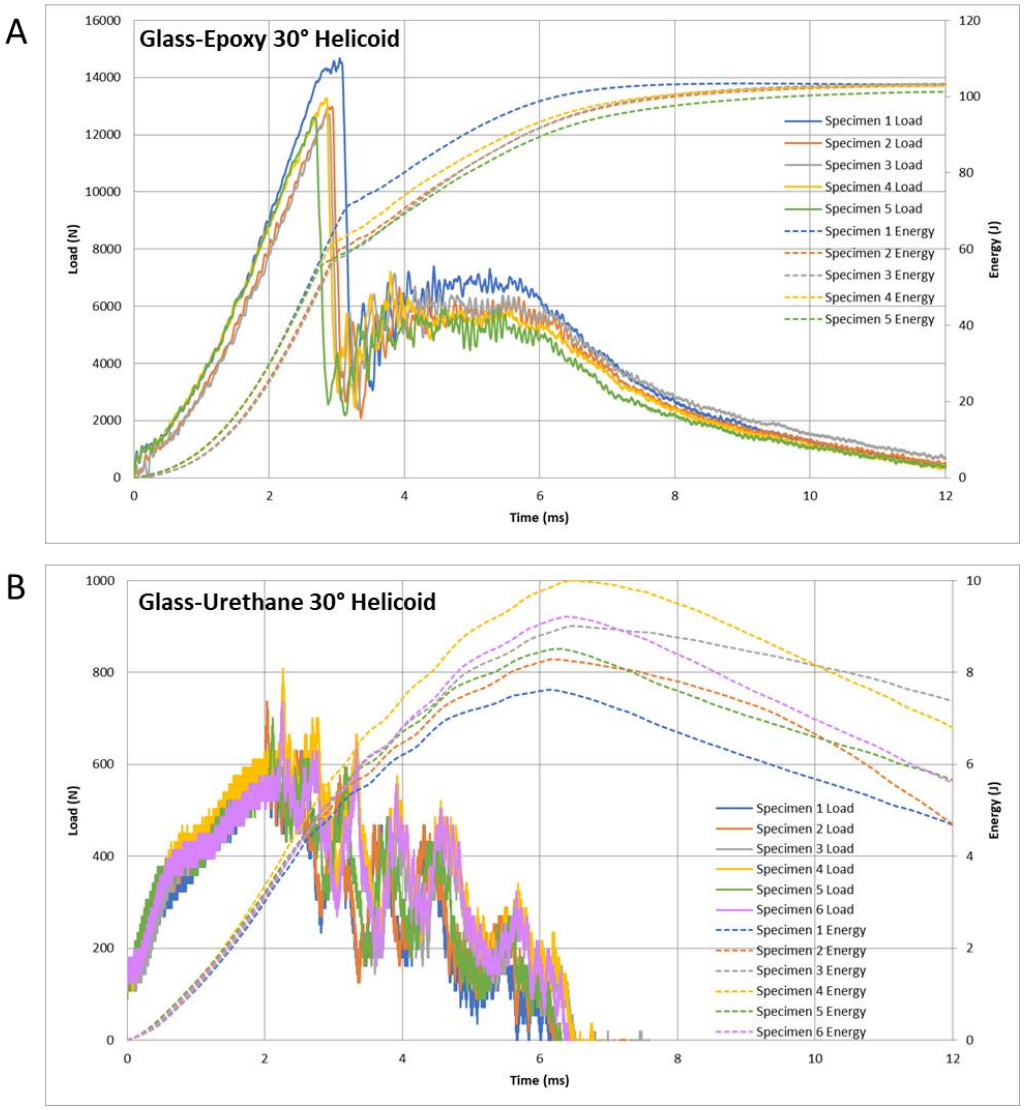

Figure 4.3. Representative impact load and energy versus time plots for biomimetic composites. (A) Load and energy vs. time plot for the large angle helicoidal glass-epoxy composites. (B) Load and energy vs. time plot for the large angle helicoidal glass-urethane composites.

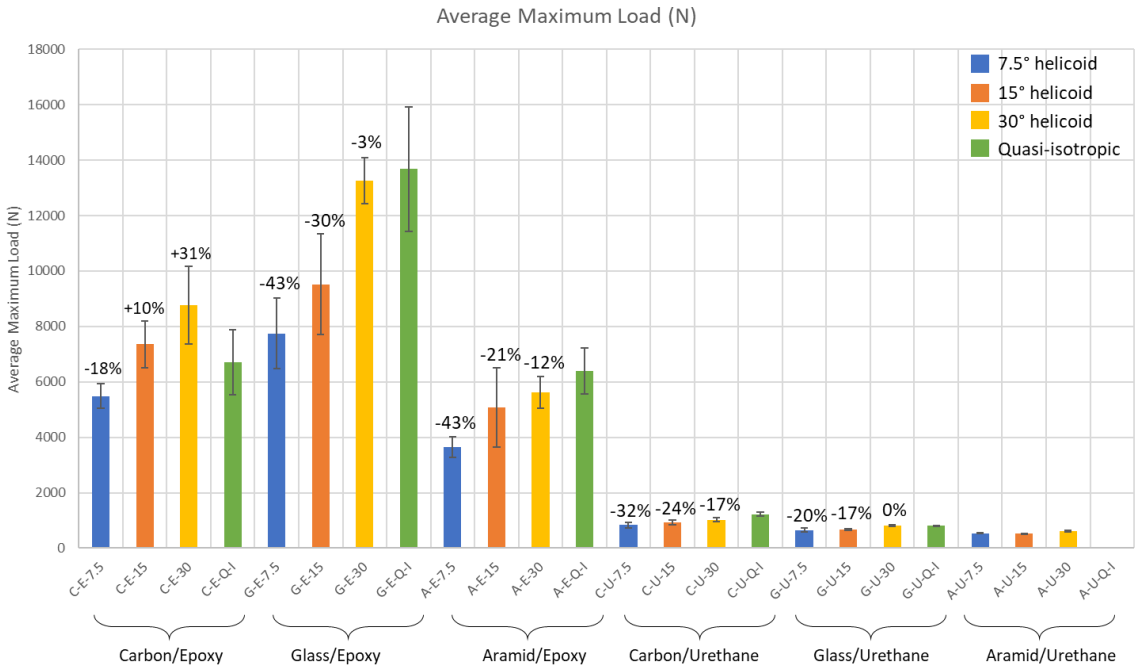

Figure 4.4. Average maximum load upon impact for biomimetic and quasi-isotropic composites. Percentages signify the change in average maximum load for the helicoidal composites in comparison to the quasi-isotropic control within each set.

highest number of reinforcement plies in the 0°, 45°, and 90° in-plane orientations, is optimal for providing the best rigidity and load-bearing capacity for out-of-plane impact.

However, maximum impact load does not provide information regarding the resistance to damage or toughness of the composite laminates. For this, we next measured the dent depth of the post-impacted composite panels. Dent depth, which is a measure of the penetration distance from the impactor into the composite, provides a qualitative, semi-quantitative measure of surface damage. Measurements of the dent depths for the epoxy matrix composites are shown in the plot in Figure 4.5. The urethane matrix composites showed no dent depth due to the highly elastic nature of the resin. Carbon-fiber epoxy composites showed the lowest dent depths while Kevlar-epoxy composites showed the

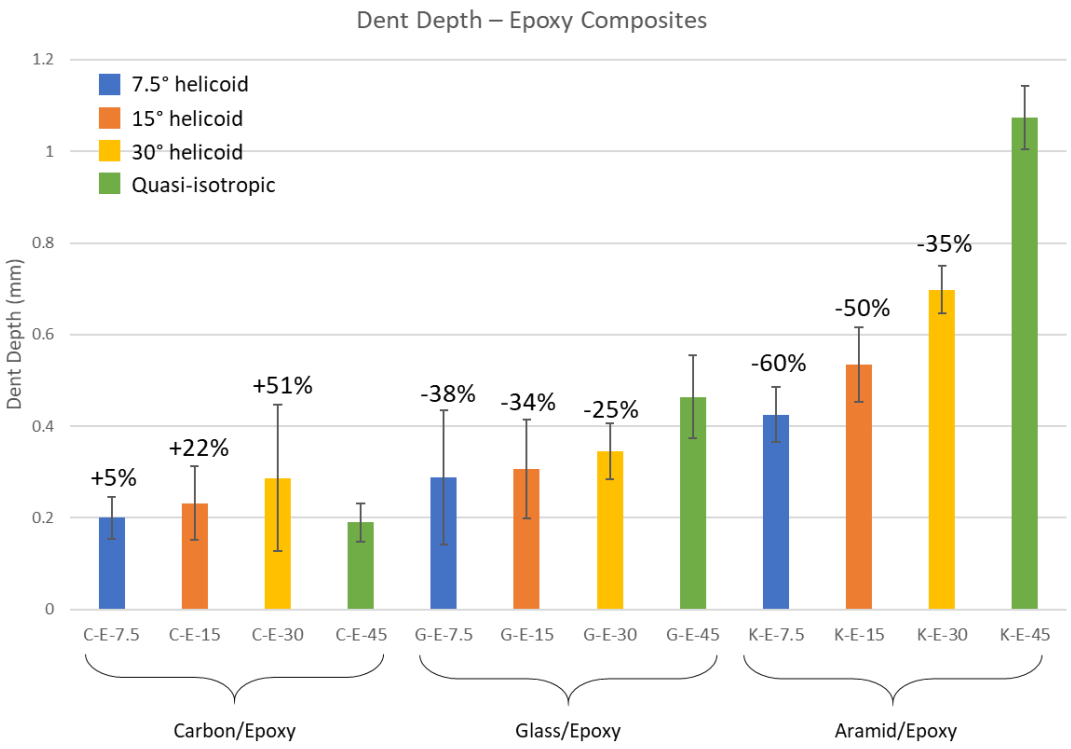

Figure 4.5. Post-impact dent depth measurements for biomimetic and quasi-isotropic epoxy composites. Percentages signify the change in dent depth for the helicoidal composites in comparison to the quasi-isotropic control within each set.

highest dent depths. It is important to note that all helicoidal composites, except for the carbon-epoxy composites, showed a reduction in dent depth compared to the quasi-isotropic control. In fact, the Kevlar-epoxy helicoidal composites show the most significant reduction in dent depth, with the small angle helicoid reporting a 60% reduction. Moreover, within each of the epoxy composites, we observed a reduction in dent depth with decreasing inter-ply rotation angle (e.g., small angle dent depth < medium angle dent depth< large angle dent depth) and the small angle helicoidal panels showed the greatest reduction in ident damage. Based on previous results by Grunenfelder et al., it is expected that a reduction in dent depth for helicoidal panels should also be observed in the carbon-

epoxy composite samples (88). The reason we do not observe this behavior in our samples may be attributed to human error and potential manufacturing defects in either the quasi-isotropic carbon-epoxy composite or the helicoidal carbon-epoxy composites.

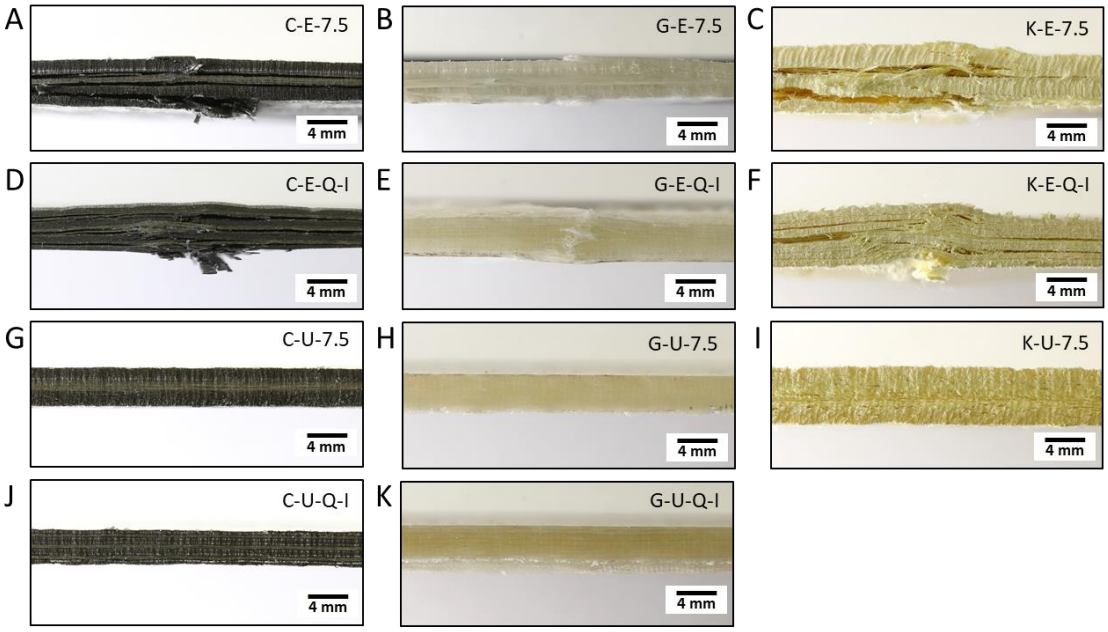

Figure 4.6. Edge-wise optical characterization of the post-impact composite panels. Small angle helicoidal epoxy-matrix composites with carbon (A), glass (B), and Kevlar (C) fiber reinforcements. Quasi-isotropic epoxy-matrix composites with carbon (D), glass (E), and Kevlar (F) fiber reinforcements. Small angle helicoidal urethane-matrix composites with carbon (G), glass (H), and Kevlar (I) fiber reinforcements. Quasi-isotropic urethane-matrix composites with carbon (J) and glass (K) fiber reinforcements.

In addition to dent depth, the impacted composite panels were examined optically to look for signs of external damage. Nearly all epoxy composites showed some form of delamination and/or fiber breakage. This is perhaps most evident in the carbon and Kevlar epoxy composites (Figures 4.6 A, D, C, F). By comparison, the urethane composites show no substantial external signs of damage (Figures 4.6 G-K). No delamination, fiber breakage, or void formation is observed through examining the panels edge-wise. Figure

4.7 shows top-down optical images of small angle helicoid and quasi-isotropic composite laminates after impact. Noticeable branching cracks emanating from the indented center are visible in the epoxy-matrix composites (Figures 4.7 A-F) whereas no external damage or cracking is visible in the urethane-matrix composite materials (Figures 4.7 G-K).

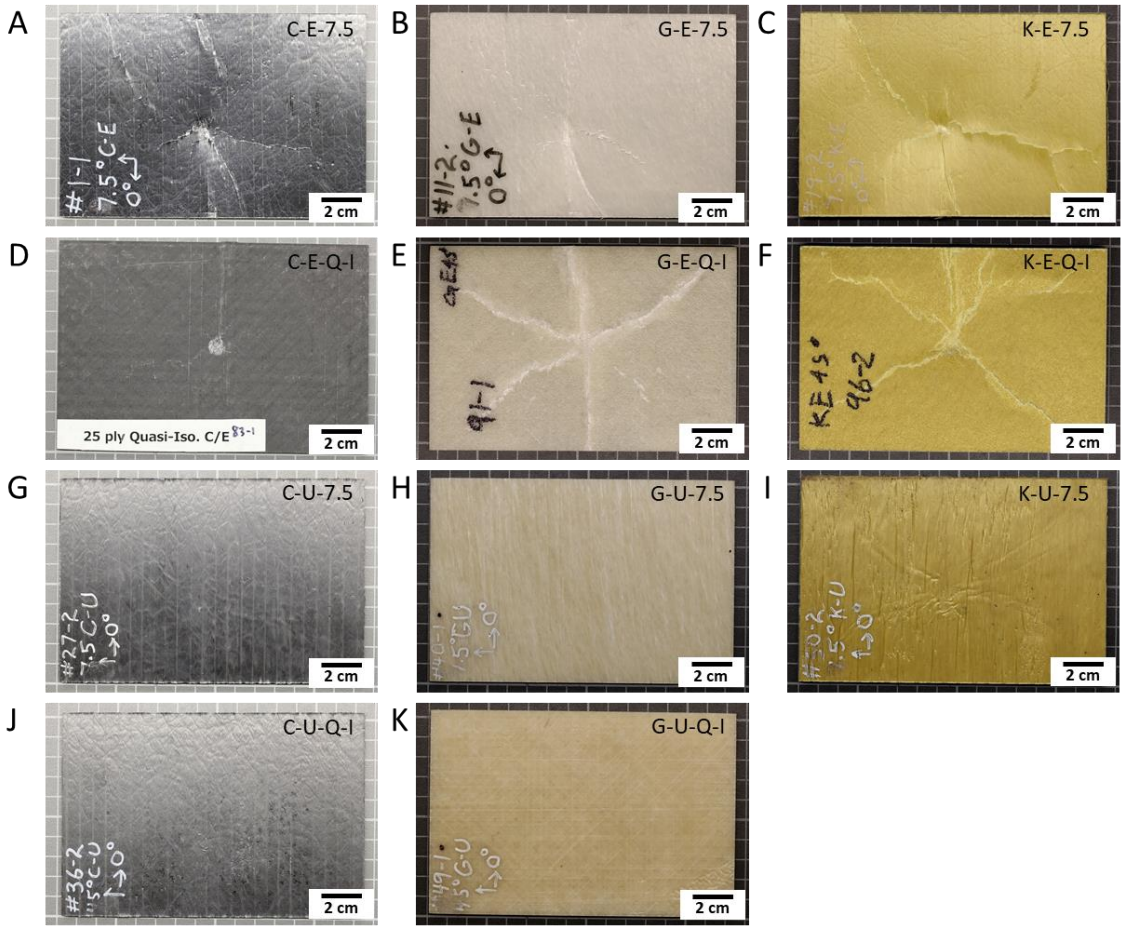

Figure 4.7. Top-down optical characterization of the post-impact composite panels. Small angle helicoidal epoxy-matrix composites with carbon (A), glass (B), and Kevlar (C) fiber reinforcements. Quasi-isotropic epoxy-matrix composites with carbon (D), glass (E), and Kevlar (F) fiber reinforcements. Small angle helicoidal urethane-matrix composites with carbon (G), glass (H), and Kevlar (I) fiber reinforcements. Quasi-isotropic urethane-matrix composites with carbon (J) and glass (K) fiber reinforcements.

Moreover, there appears to be more extensive cracking in the glass- and Kevlar-epoxy quasi-isotropic composites than in the small angle biomimetic helicoid panels. Micro-CT will be needed, however, to confirm this. Micro-CT measurements may be performed in future work.

4.4.4 Residual strength of impacted biomimetic helicoidal FRCs

The residual mechanical properties of the fabricated biomimetic and standard control composite laminates were assessed by performing compression after impact experiments. Samples were loaded end-on in a compression rig and tested to failure. Examination of the resulting load-displacement curves reveals differences in the response of the epoxy- versus urethane-matrix composites (Figure 4.8). The epoxy composites tend to fail catastrophically, as evident by the sharp drop in load following peak compressive stress (Figures 4.8 A, C, E). Some panels show a step-wise decrease in load, indicating multiple localized fracture events prior to failure. By comparison, the urethane-matrix composites show more gradual decrease in load following peak compressive stress (Figures 4.8 B, D, F). This is perhaps an indication of the composites buckling and the fibers and matrix bending as opposed to cracks forming and propagating through the volume. The inherently more brittle epoxy material is likely responsible for the cracking observed in the load-displacement curves of the epoxy-matrix composites. The sharp drops in load following the failure of the epoxy composites may also be caused by the breakage of fibers.

Examining the peak compressive stress data (Figure 4.9) reveals that the epoxy-matrix composites have the highest residual strength. This is expected due to the higher

Young's modulus of the matrix material. The epoxy-composites have average residual strengths ranging from approximately 17 to 49 MPa, with the highest residual strength observed in the large angle glass-epoxy helicoidal composite laminate (48.8 ± 3.9 MPa).

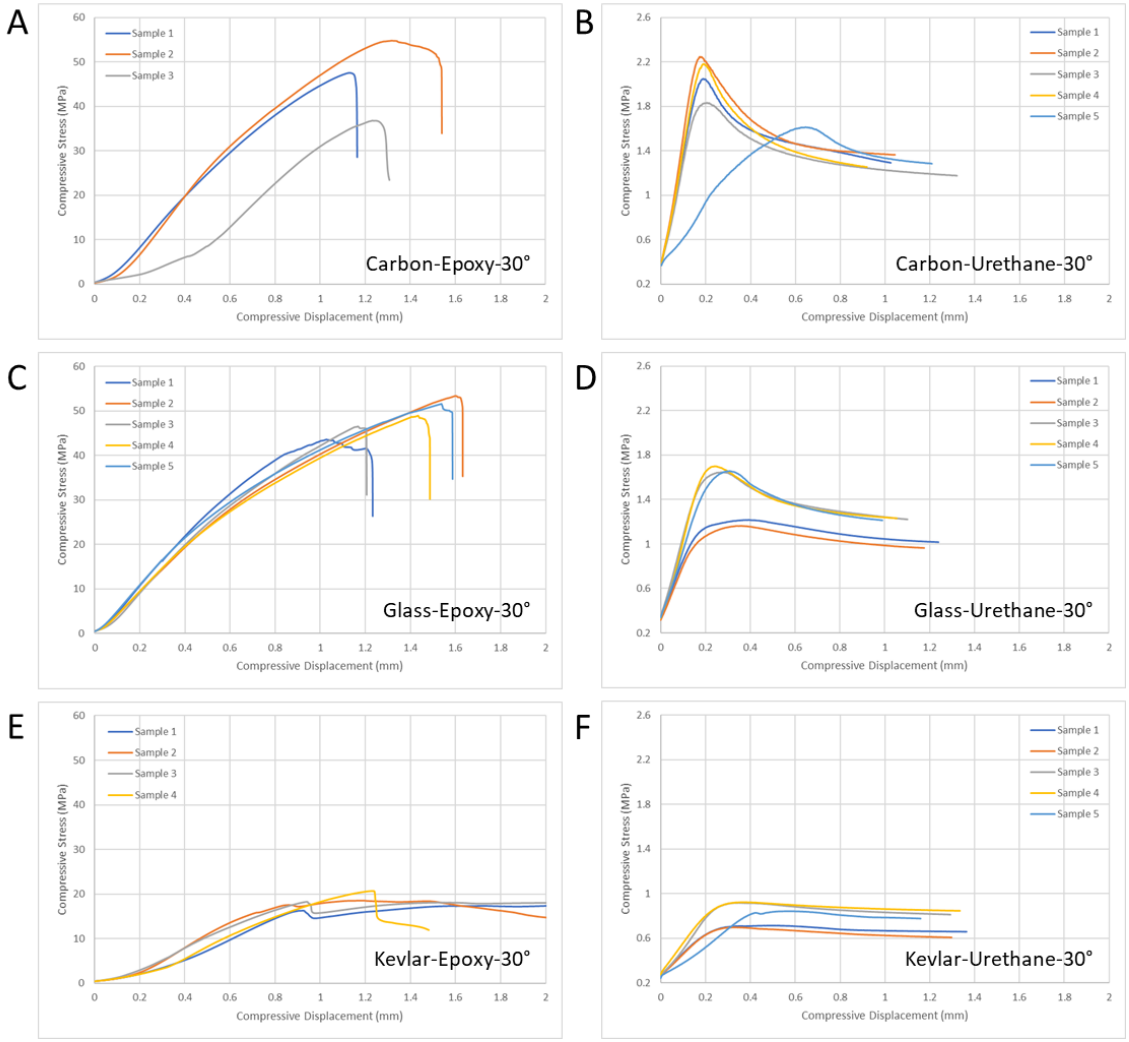

Figure 4.8. Compression after impact data for large angle helicoidal composites. Compressive stress versus displacement for large angle carbon-epoxy (A), carbon-urethane (B), glass-epoxy (C), glass-urethane (D), Kevlar-epoxy (E), and Kevlar-urethane (F) helicoidal composites.

Conversely the urethane-matrix composites have average residual strengths ranging from approximately 0.7 to 2 MPa. The quasi-isotropic carbon-urethane composite laminate reported the highest residual strength (2.86 ±0.34 MPa) among the urethane composites.

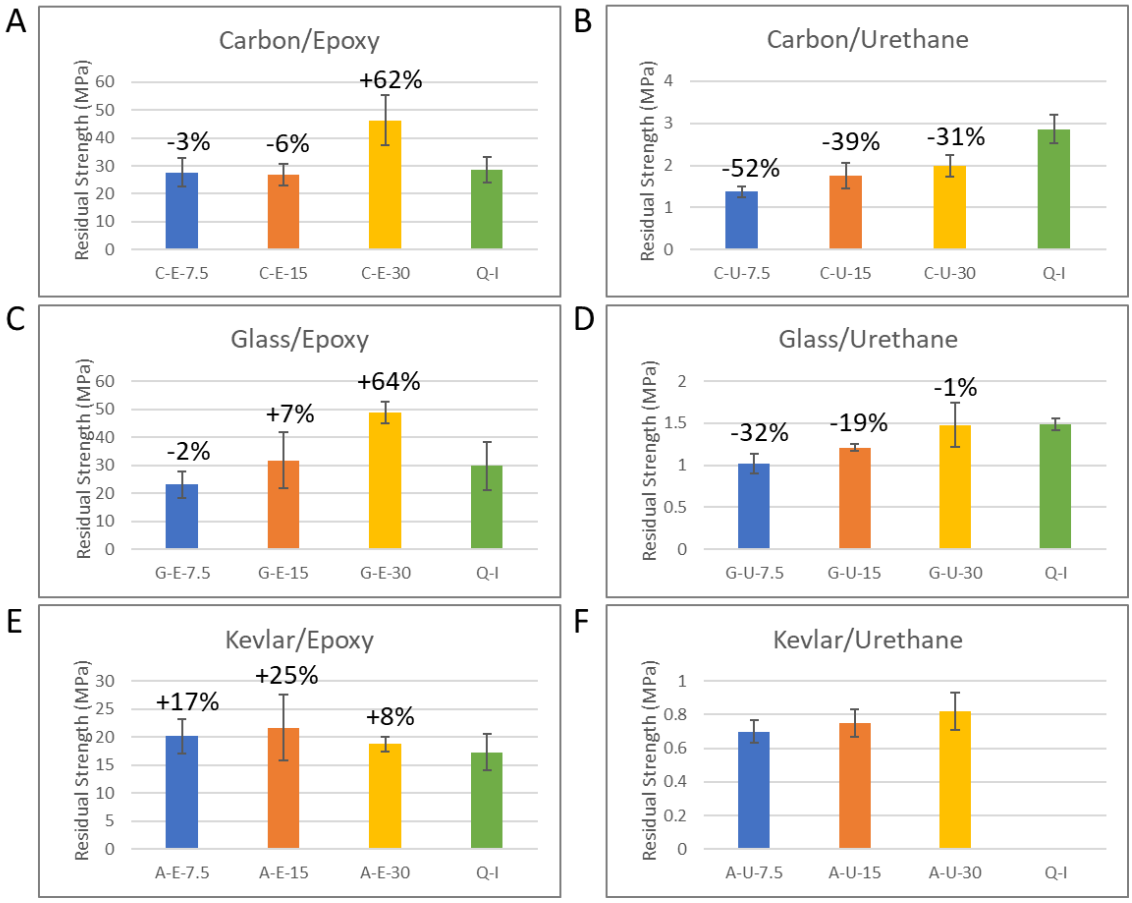

Figure 4.9. Residual strength of biomimetic and control composite laminates. Plots from compression after impact experiments showing average maximum compressive stress for carbon-epoxy (A), carbon-urethane (B), glass-epoxy (C), glass-urethane (D), Kevlar-epoxy (E), and Kevlar-urethane (F) composites. Different color bars denote small angle helicoid (blue), medium angle helicoid (orange), large angle helicoid (yellow), and quasi-isotropic (green) panels.

A most interesting result was observed when examining the performance of the helicoidal composite laminates compared to the quasi-isotropic control within each reinforcement-matrix subset. Within the epoxy-matrix composites, numerous helicoidal

panels showed an improvement in the residual compressive strength when compared to the quasi-isotropic design. For carbon- and glass-epoxy composites, the large angle helicoidal panels showed the greatest improvement over the quasi-isotropic (62% and 64%, respectively). These results are consistent with observations made by Grunenfelder et al., who showed that medium and large angle helicoidal designs showed the greatest improvement in residual strength compared to a quasi-isotropic design within carbon fiber-epoxy composite laminates (88). Within the Kevlar-epoxy composites, each of the small, medium, and large angle helicoidal geometries showed an improvement in residual strength compared to the quasi-isotropic control (17%, 25%, and 8%, respectively). Interestingly, none of the urethane-matrix biomimetic helicoidal composites showed an improvement in residual strength over the quasi-isotropic panels. The reason for these differences in performance likely relates back to the Young's modulus mismatch between reinforcement and matrix materials and the ability for cracks to deflect at the fiber-matrix interface. The modulus difference between the carbon, glass, and Kevlar reinforcements and the epoxy matrix may be sufficient to allow for crack deflection. Therefore, the helicoidal architecture may better facilitate the delocalization of damage within the epoxy composites. Conversely, since the urethane-matrix composites seem to not show any brittle behavior, it could be that there is minimal cracking within the matrix and so the effect of the helicoidal fibrous architecture on spreading damage may be less pronounced. Mechanical modeling will be useful to confirm these experimental results and will be conducted in future work.

4.4.5 Direct ink writing of helicoidal chitosan architectures

The ability to fabricate biomimetic helicoidal structures featuring more unique materials was investigated through direct ink write additive manufacturing. Chitosan was initially chosen as a feedstock material due to its similarity to the biopolymer, chitin, which is found in the mantis shrimp cuticle and exoskeletal structures of most arthropods. An ink formulation used by C.R. Almeida et al. was initially reproduced and tested (168). Direct extrusion of chitosan solution by hand into a coagulation bath was first attempted to see if continuous filamentous structures could be formed. A syringe pump was used to precisely control the shear rate and flow of the chitosan solution. The first experiment tested the extrusion of 1% (w/v) chitosan solution in 2% (v/v) acetic acid into a coagulation bath of 8% (w/v) sodium hydroxide in 70% ethanol in water solution. Approximately 1 mL of the chitosan solution was loaded into a 2 mL syringe capped with a conical tip attached to a piece of PFA tubing with inner diameter 0.762 mm. The tubing was fed into a 5 mL scintillation vial containing 2 mL of the 8% sodium hydroxide in 70% ethanol solution. The tubing was submerged into the coagulation bath such that once the chitosan exited the tubing, it would be extruded directly into the coagulation bath. Two flow rates were initially tested: 15 mL/hr and 30 mL/hr. Both experiments were unsuccessful resulting in the precipitation occurring too rapidly causing the chitosan to simply clog at the tubing exit (Figure 4.10 A, B). After some trial and error and modification of the testing parameters, the optimal concentration of the chitosan solution was determined to be 3%. The experiments were repeated with extrusion into the 8% sodium hydroxide in 70% ethanol bath at flow rates of 15 mL/hr and 30 mL/hr. This time, the experiments were successful

for both flow rates and formation of continuous gel-like chitosan filaments was achieved (Figures 4.10 C, D, E).

Next, the stability of the printed chitosan filaments under various drying/hydration conditions was examined to determine what post-processing would be required to maintain the 3D printed structure (Figure 4.11). Chitosan filaments were printed directly into an 8% sodium hydroxide in 70% ethanol coagulation bath and then immediately removed and

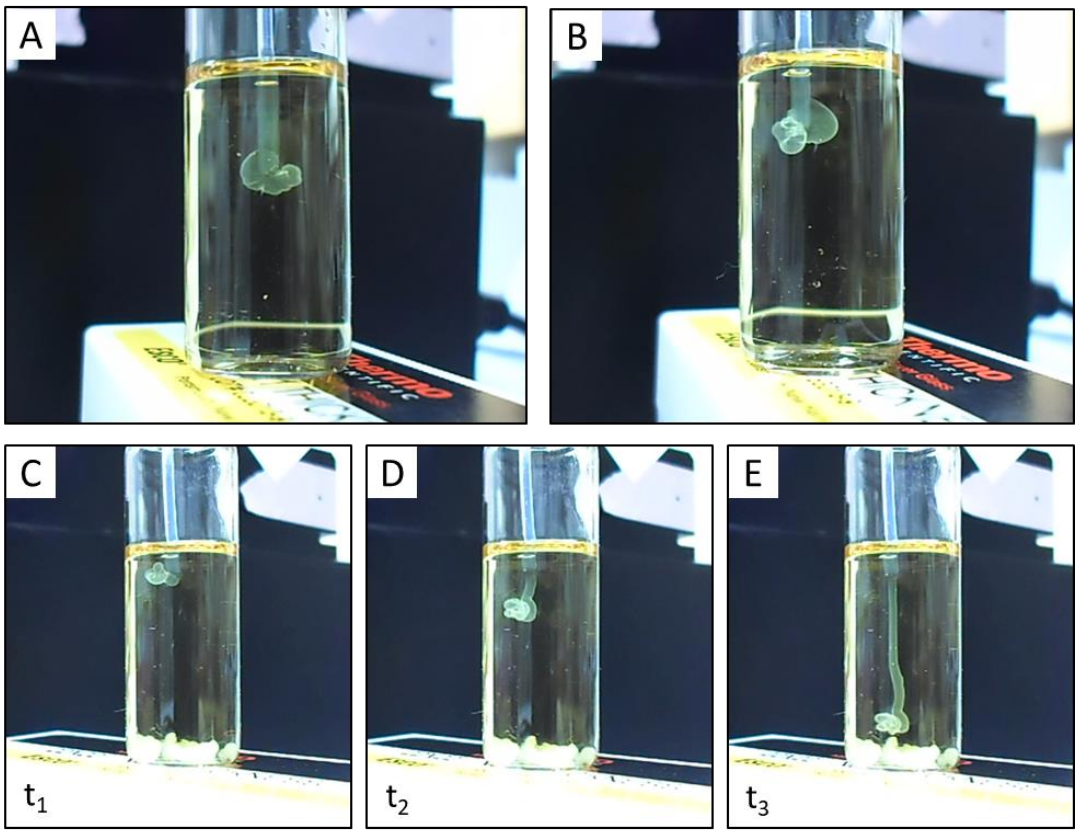

Figure 4.10. Test extrusions of chitosan into coagulation bath. (A, B) Optical images showing rapid precipitation of chitosan and clogging at the nozzle following extrusion of 1% (w/v) chitosan in 2% (v/v) acetic acid into a coagulation bath of 8% (w/v) sodium hydroxide in 70% ethanol using flow rates of 15 mL/hr (A) and 30 mL/hr (B). (C, D, E) Still-frame images at various time points showing successful extrusion of 3% chitosan into 8% sodium hydroxide in 70% ethanol solution and formation of a continuous chitosan filament.

incubated in air (Figures 4.11 A, D), 70% ethanol (Figures 4.11 B, E), and deionized water (Figures 4.11 C, F) for 36 hours. The chitosan dried in air no longer held its filamentous shape. The water evaporated, and a crystallized material was left on the glass slide. The filament stored in 70% ethanol showed some visible signs of dehydration and surface deformation. Meanwhile, the filament stored in deionized water appeared unchanged, preserved its cylindrical shape, and showed no signs of deformation.

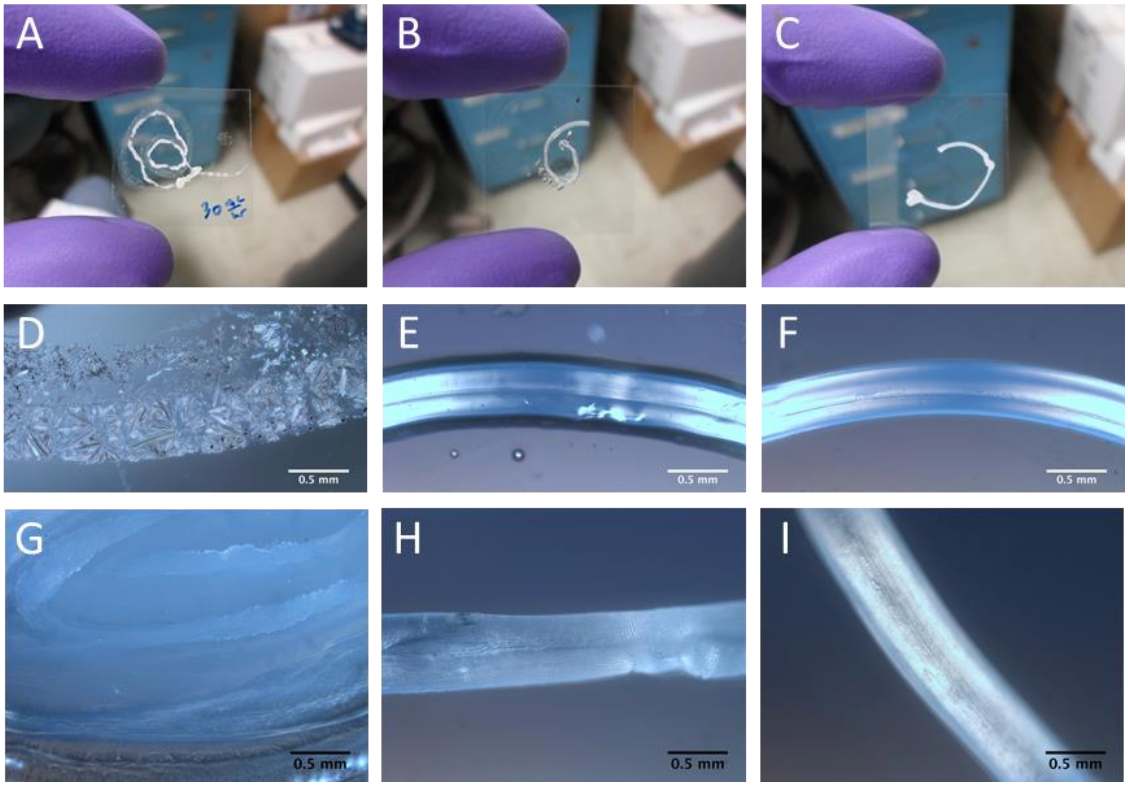

4.11. Incubation studies on chitosan filament stability. (A, B, C) Low magnification images showing chitosan printed filaments after 36 hours in air (A), 70% ethanol (B), and deionized water (C). (D, E, F) High magnification optical micrographs showing chitosan printed filaments after 36 hours in air (D), 70% ethanol (E), and deionized water (F). (G, H, I) High magnification optical micrographs of chitosan filaments coagulated and incubated for 10 minutes in 0.5% (G), 1% (H), and 1.5% (I) (w/v) sodium hydroxide in 100% ethanol solution.

In addition to examining the effect of storage medium on chitosan filament stability, the concentration of the coagulation bath medium was modified (reduced) to slow down the gelation process to further prevent clogging of chitosan solution at the nozzle exit. This was achieved by reducing the concentration of sodium hydroxide in the bath medium. Figures 4.11 G-I show the resulting chitosan filaments after printing and incubation for 10 minutes in solutions of 0.5% (Figure 4.11 G), 1% (Figure 4.11 H), and 1.5% (Figure 4.11 I) (w/v) sodium hydroxide in 100% ethanol. The filament printed in the 0.5% solution showed no remaining filamentous structure after incubation whereas the filament printed in the 1% solution became soft and "gummy", no longer maintaining a cylindrical shape.

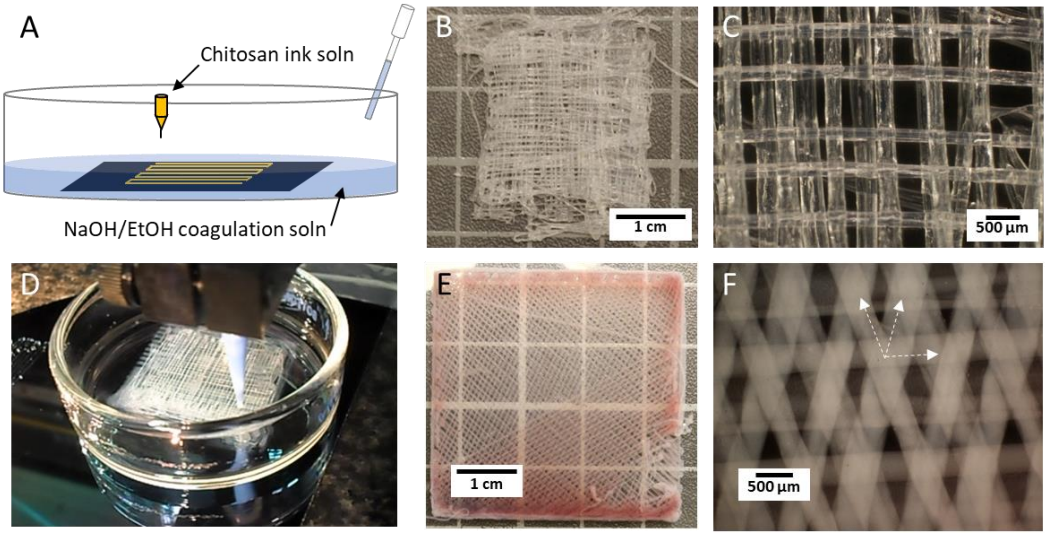

Figure 4.12. 3D printing of chitosan scaffolds. (A) schematic showing process for printing chitosan into a coagulation bath. (B) Image of a 3D printed 0°/90° chitosan scaffold. (C) High magnification optical micrograph of the printed 0°/90° chitosan scaffold. (D) Image of the chitosan direct ink write printing process where chitosan is extruded into a petri dish containing a bath of sodium hydroxide/ethanol coagulation solution. (E) Image of a 3D printed 60° helicoidal chitosan scaffold. (F) High magnification optical micrograph of the printed 60° helicoidal chitosan scaffold, arrows denoting 0°, 60°, and 120° fiber orientations.

The chitosan filament printed into the 1.5% sodium hydroxide in 100% ethanol solution maintained its cylindrical shape and had a noticeable stiffness, and stability after the incubation. Thus, the 1.5% bath solution was chosen for subsequent printing studies.

3D printing of the chitosan ink was then tested on a custom built direct ink write system (in collaboration with Lawrence Livermore National Laboratory) as well as on a modified delta style 3D printer. Figure 4.12 shows the results of successful 3D printing of multi-layered 0°/90° as well as 60° helicoidal structures. High magnification optical micrographs of the printed scaffolds show good control over the filament alignment, orientation, and overall scaffold architecture. The filaments also show consistent and uniform diameter and maintain a circular cross-section. Although additional improvements to the printing process can be made, these scaffolds provide a promising foundation for the fabrication of mantis-shrimp inspired helicoidal composite materials.

4.4.6 Direct ink writing of ceramic helicoidal structures

A critical component of many hard and tough biocomposite materials is the incorporation of inorganic biominerals. To mimic the hard-ceramic materials and their architectures, aluminum oxide ceramic 3D printable inks were investigated. Ink formulations for alumina were adapted and modified from work by Rao et al. (173). Mixtures of 40% (w/v) polyacrylic acid (aq.) were initially mixed with aluminum oxide powder in a 0.65 g: 1 g ratio, followed by planetary centrifugal mixing, and final additions of minor fractions of 10% (w/v) polyethylene glycol (aq.) solution and cellulose powder. Initially the ink appeared runny and a qualitative assessment was made that the viscosity

of the ink was too low. Manual test extrusions of the initial 60% (w/w) ceramic-loading ink onto glass slides showed that indeed the viscosity was too low. The printed filament did not maintain a cylindrical cross-section (Figures 4.13 A, B). Through incremental additions of additional alumina powder as well as polyethylene glycol (flocculant) and planetary centrifugal mixing, the ink obtained a peanut-butter like consistency suitable for direct ink write. The final formulation, consisting of approximately 70% (w/w) loading

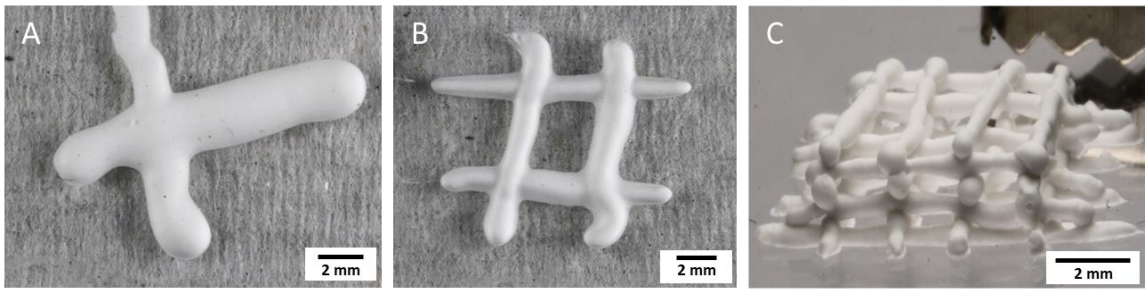

Figure 4.13. Preliminary extrusions of alumina ink. (A, B) Unsuccessful, low viscosity formulations showing liquid-like extrusions of the alumina ink. (C) Successful multi-layered manual 3D print of a 0°/90° structure when higher loading fraction of ceramic and higher concentration of polyethylene glycol flocculant are used. Notice the filaments are semi-cylindrical in shape and self-supporting.

fraction of aluminum oxide, was able to be successfully manually printed into a 3-dimensional structure (Figure 4.13 C). The ceramic filaments are capable of self-supporting and spanning distances of approximately 1 mm within the part without any noticeable sagging.

More complex parts were then printed manually using the ceramic ink formulation. Figure 4.14 A shows the resulting 3D printed 6-layer helicoidal structures with 30° inter-layer rotation. In addition to printing, the parts were post-annealed in air to 1300° C (Figure 4.14 B) to attempt to sinter the micro-scale alumina particles together to form a dense and

strong part. Investigation of the microstructures of the as-printed (Figure 4.14 D) and post-annealed (Figure 4.14 E) structures reveals the burn out of the polymer, which coated and bound the particles in the as-printed part. Moreover, SEM analysis seems to suggest that there were very few instances of sintering of the particles, likely due to their large particle size (approximately 5-10 μm in diameter) and thus high energy required to induce sintering. In addition, the ability to form a composite material was investigated by infiltrating an epoxy resin polymer into the void space between the ceramic fibers (Figure 4.14 C), thus more closely mimicking the composite nature of the dactyl club and telson.

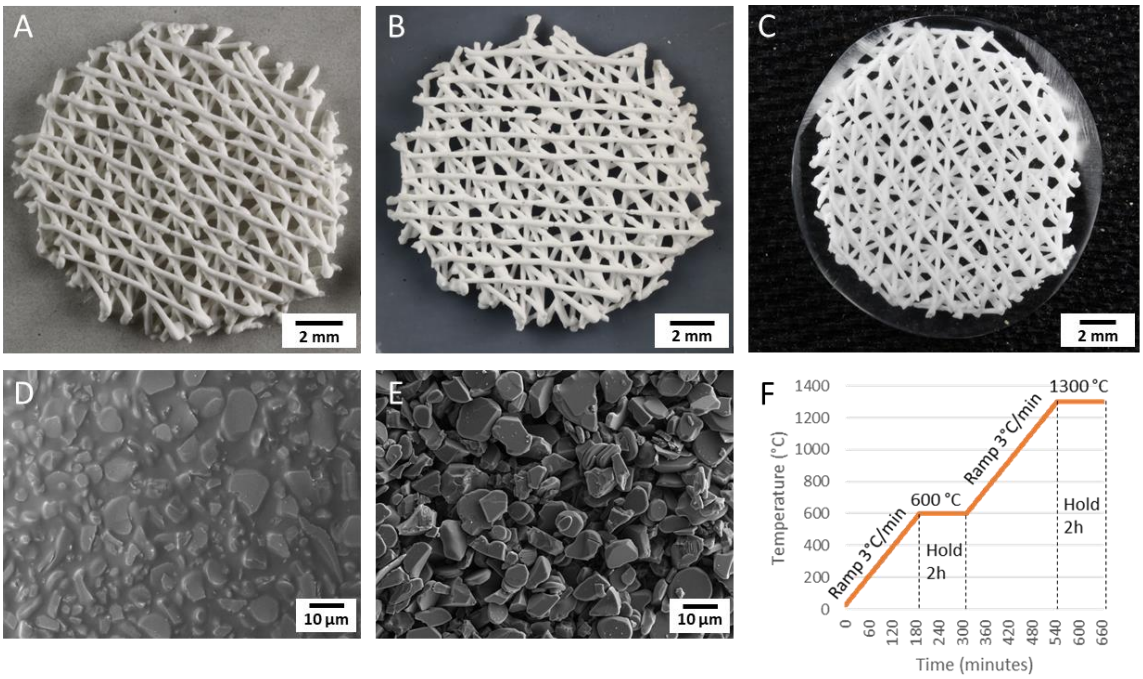

Figure 4.14. 3D printing, annealing, and composite fabrication of helicoidal alumina structures. (A) Optical image of the as-printed 6-layer 30° helicoidal structure. (B) Optical image of the same helicoidal structure after annealing to 1300° C. (C) Optical image of the epoxy-infiltrated helicoidal alumina composite structure. (D) SEM micrograph of the surface of the as-printed ceramic filament, corresponding to structure in (A). (E) SEM micrograph of the surface of the post-annealed ceramic filament, corresponding to the structure in (B). (F) Temperature versus time profile for the annealing process.

To facilitate the sintering of the alumina particles and improve the theoretical strength of the 3D printed ceramic parts, the alumina ink formulation was modified to incorporate silica, forming a mullite ($3Al_2O_3$:$2SiO_2$) phase. Mullite reportedly achieves a lower sintering temperature than pure alumina (174) and can therefore be a viable alternative to producing dense, stiff ceramic parts via 3D printing. Instead of a 0.65 g polyacrylic acid to 1 g alumina ratio, we used a 2 g polyacrylic acid to 1 g mullite (1.8 g alumina, 1.2 g silica). Figure 4.15 shows the resulting 3D printed helicoidal mullite part

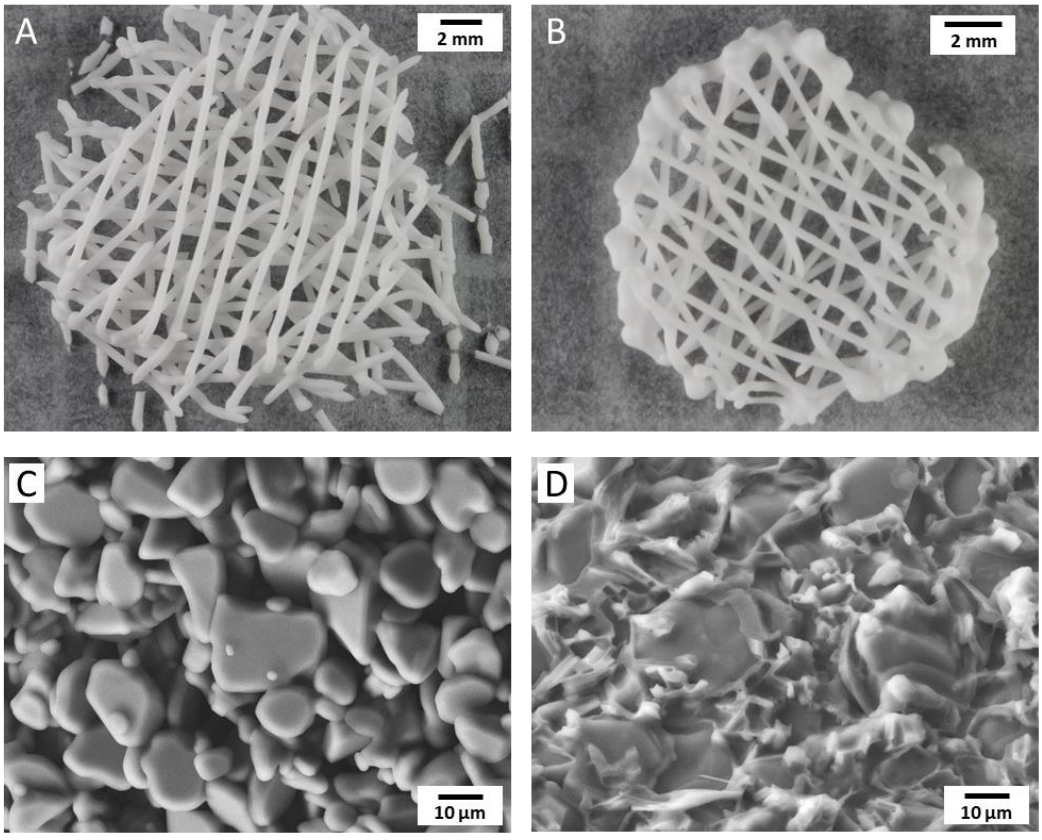

Figure 4.15. 3D printing of mullite parts and examination of particle sintering. (A) As-printed mullite layered helicoidal structure. (B) Mullite helicoidal structure after annealing in air to 1600° C. (C) SEM micrograph showing surface of alumina filament after annealing in air to 1700° C. Particles do not appear to be sintered and there are many voids. (D) SEM micrograph showing surface of mullite filament after annealing in air to 1600° C. Part appears dense and particles appear to be sintered together.

(Figure 4.15 A) as well as a mullite part that had been annealed in air to 1600° C (Figure 4.15 B). Comparing the microstructures of a pure alumina-based 3D printed part that had been sintered to 1700° C (Figure 4.15 C) and the mullite-based printed part sintered to 1600° C (Figure 4.15 D) shows a denser mullite part. The incorporation of fumed nanoparticles of silica into the mullite ink as well as the lower sintering temperature seems to suggest that the silica can effectively fuse the alumina particles together upon annealing to 1600°C. By comparison, even after annealing the pure alumina-ink part to 1700°C, there are still significant and noticeable voids between the particles, and while there may be small necks between the edges of alumina particles indicating sintering, the part overall is significantly less dense than the mullite part. In addition, while proper mechanical testing and comparison of the properties of the alumina and mullite parts has not yet been done (planned future work), these results provide promise for the fabrication of dense, strong ceramic 3D printable and bioinspired structures.

4.5 Conclusions

In this work, we examined the potential for fabricating biomimetic composite materials inspired by the helicoidal fibrous architectures observed within the mantis shrimp dactyl club and telson. We explored two different processing routes for this fabrication: traditional fiber reinforced composites processing and ink formulation and direct ink write additive manufacturing. Building off previous work investigating the potential for helicoidal architectures in composite laminates to improve damage-tolerance and impact-resistance, we looked at the effect of reinforcement and matrix material choice, in addition

to inter-ply rotation angle on the impact response, damage-resistance, and residual properties. Carbon fiber, glass fiber, and Kevlar fiber reinforcements were combined with epoxy and urethane matrices in four different layup geometries: a small, medium, and large angle biomimetic helicoidal design, and an industry standard quasi-isotropic design.

Epoxy-matrix composites tended to show the highest peak load on impact, an expected result due to the inherent stiffer nature of the material. Impacted epoxy-matrix composites showed larger degrees of external damage such as delamination and fiber breakage as compared to the urethane-based composites, which showed no external damage. Most importantly however, within the epoxy-matrix composites, all helicoidal panels, with the exception of carbon fiber reinforced ones, showed a significant reduction in dent depth as compared to the quasi-isotropic design, which is a measure of through-thickness damage following impact, with small angle panels showing the greatest reduction. Moreover, comparing residual compressive strength of the panels, a majority of the helicoidal epoxy-based composites show significant improvement compared to the quasi-isotropic design, with large-angle carbon-epoxy and glass-epoxy composites reporting over a 60% higher residual strength. While urethane-based composites seemed to not provide much improvement over the quasi-isotropic panels and epoxy-matrix composites, useful information can be gleaned regarding the role of modulus mismatch between reinforcement and matrix materials in driving crack deflection and providing a useful avenue for the helicoidal architecture in delocalizing damage and improving residual strength.

With respect to additive manufacturing, we have demonstrating the ability to develop useful new feedstock materials for a more accurate mimicry of the natural biological systems. Chitosan biopolymer- and alumina/mullite ceramic-based inks were put to the test and we demonstrated the successful ability to fabricate helicoidal laminated structures with excellent control over filament diameter, orientation, and spacing. Chitosan-based 3D printing would likely not yield the next generation of high strength or high toughness materials but could potentially be useful in templating crystallization and understanding biomineralization processes. Helicoidal organic scaffolds may be helpful for understanding the formation of complex fibrous architectures, such as the herringbone structure observed within the impact region of the dactyl club (1). Alumina and mullite 3D printing, especially when combined with a softer matrix phase to form a composite, could be useful for structural applications, given that dense void-free structures can be created. Future work will need to characterize the mechanical properties of the sintered alumina/mullite parts as well as their composites to understand the effect of annealing treatments. Moreover, mechanical testing of these helicoidal composite parts would be useful for determining whether similar toughening mechanisms as observed in the natural systems, such as crack deflection and crack twisting can be initiated in synthetic 3D printed helicoidal structures.

Chapter 5: Structural development of the dactyl club and a future outlook on biomimetic materials synthesis

5.1 Biomineralization of the dactyl club

It is well understood at this point that structural aspects of the mineral component of the dactyl club, namely the phase, crystallinity, orientation, and morphology, directly influence its mechanical function. Amorphous phases of mineral are responsible for the lower elastic modulus and hardness observed within the inner periodic region while graded concentrations of crystalline hydroxyapatite provide higher elastic modulus and hardness within the impact region, with maximum values at the club surface. The high degree of preferential c-axis alignment of apatite crystals normal to the surface of the club provides optimal anisotropic stiffness in the direction of loading and the presence of hard isotropic single crystalline particles provides a potential stress redistribution effect at the impact surface (1; 106). Questions remain as to how this multi-phasic mineral forms and what parameters (i.e. surface chemistry, local pH, ect.) influence nucleation and growth. For example, it has been suggested that magnesium plays a role in stabilizing amorphous calcium carbonate and calcium phosphate mineral, suggesting its potential function and reason for existing in higher concentrations within the periodic region of the dactyl club (115; 116). Does the mineral within a newly forming dactyl club initially exist as a hydrated amorphous phase, which subsequently crystallizes in the impact region forming crystalline and textured apatite? At what stage does this crystallization occur and what triggers this onset of mineralization? Additionally, does crystallization influence the architecture of

organic fibers? Perhaps a most interesting question is how and why does the unique herringbone structure observed within the impact region form? Could it be due to residual stresses that causes the helicoidal fibers to buckle, forming herringbone units, during the transition from a hydrated amorphous phase to a crystalline state?

Much literature in the biomineralization community has also confirmed and reinforced the role of proteins and peptides associated with the organic matrix on controlling crystallization. These biomacromolecules contain specific chemical functionalities and stereochemistries that have been found to either facilitate or inhibit crystal nucleation and growth, thus influencing the resultant phase, crystallinity, morphology, and orientation of mineral. For example, several phosphoproteins, called SIBLING proteins (small integrin-binding ligand, N-linked glycoprotein), associated with the extracellular matrix of bone have been studied for their role in the nucleation, growth, and inhibition of hydroxyapatite (175). Dentin phosphophoryn (DPP) is one such protein that has been found to be heavily involved in dentin and bone mineralization (175). DPP is an acidic protein rich in aspartic acid and serine, which has been linked to hydroxyapatite nucleation. Examination of DPP reveals the presence of certain repeat domains that have ribbon-like, twisted chain structure with repeating arrays of carboxylate and phosphate groups (175). It is proposed that this specific structure could interact well with calcium ion arrays along the surface of hydroxyapatite, facilitating nucleation. Phosphorylated osteopontin has acidic domains such as aspartic acid residues, resulting in a high number carboxylate as well as phosphate groups. It has been suggested that, once this protein has adsorbed on a crystal surface, these groups create a negative charge density that produces

an electrostatic repulsion of mineral phosphate ions (175). Thus, new atoms cannot be added to the lattice and further growth is arrested.

Numerous authors have also investigated biomineralization with respect to the nacre structure. Nudelman et al. mapped the distribution of organic matrix components and functional groups on the nacreous surfaces of the bivalve, *Atrina rigida*, and cephalopod, *Nautilus pompilius (62).* They examined the location of sulfates, carboxylates, and calcium-binding sites on the matrix surface upon decalcification of the aragonite tablets. The authors claimed that each of these components play a unique role in the nucleation, growth, and cessation of growth of mineral in nacre (62). Mapping revealed a carboxylate-rich central zone surrounded by sulfate groups. The carboxylate- and sulfate-rich groups arise from the aspartate side chains of acidic proteins and sulfated side chains of polysaccharide respectively (62). The authors maintained that the sulfated groups are able to effectively attract calcium ions, which aids in creating the supersaturation conditions necessary for nucleation and then the carboxylate groups can effectively bind the calcium in an ordered array (62).

5.2 An opportunity to study biomineralization through molting

Because of the rigid exoskeletons encompassing their soft tissue, arthropods must periodically shed (molt) their exoskeletal structure in order to grow (176). The molt cycle begins with apolysis, the onset of premolt, during which the hypodermis is separated from the cuticle through the work of secreted chitinase and other enzymes that dissolve the membraneous layer (176). The new epicuticle and exocuticle are next laid down beneath

the endocuticle of the old cuticle; however, they are not mineralized until the old cuticle is shed (176). Concurrently, mineral from the old cuticle is resorbed. Pore canal tubules provide transport pathways for the resorption of mineral (177). Amorphous mineral is advantageous in its ability to be easily resorbed and stored in structures such as gastroliths during molting (178). The crystalline mineral, which is usually less soluble, cannot be resorbed and is thus shed with the old exoskeleton. The molt stage follows, in which the old cuticle is shed from the body. The post-molt follows, during which the exocuticle is tanned/sclerotized (cross-linked with protein), and mineralization begins within the outermost regions of the epicuticle and the exocuticle (176). Transport of mineral ions is again achieved through the pore canal network (177). The deposition of the endocuticle follows, and the endocuticle becomes mineralized as the organic layers are being deposited. It is here that we expect formation of the endocuticle to take on a chiral nematic ordered structure by the cholesteric self-assembly of chitin-protein fibrils. The exocuticle additionally becomes further mineralized; the end of the post-molt occurs when the membranous layer is deposited and new mineralization is ceased (176).

Based on this information, extracting and characterizing the dactyl club during various stages of the molt cycle could provide insight to the different stages of chitin fiber assembly as well as mineralization. Proposed future work would investigate the formation of the organic matrix and the crystallization of biomineral within the stomatopod dactyl club. Dactyl club specimens would be carefully extracted from the mantis shrimp during various stages of the molt cycle: freshly molted and nonmineralized, partially mineralized, and fully mineralized. The club specimens would be immediately fractured, lyophilized,

and characterized by optical microscopy and SEM. Examination of the ultrastructure would provide insight to the assembly mechanisms of fibers, the structural development of different regions and subdomains within the dactyl club, and the nucleation and growth of mineral. A combination of powder x-ray diffraction, SEM, high resolution TEM, and selected area electron diffraction could be used to determine the phase, crystallinity, and orientation of mineral.

5.3 Preliminary mineralization experiments

Given the potential difficulty of inducing molting in the live organisms, concurrent ex-situ and/or in-situ study of the biomineralization process would be performed via demineralization-remineralization and overgrowth experiments on the dactyl club. Fully mineralized club specimens could be demineralized using a variety of etching solutions (e.g., hydrochloric acid, acetic acid, citric acid, ethylenediaminetetraacetic acid) for various amounts of time. EDS or Raman spectroscopy would be used to confirm that the mineral is fully removed. Subsequent remineralization would be performed via a double diffusion process through Agar gel containing embedded dactyl scaffolds or by simply placing the dactyl scaffolds in a supersaturated precursor solution containing low concentration calcium and phosphate ion species. The scaffolds would be mineralized for various periods of time after which the surface and nucleated mineral structure would be characterized via a combination of SEM and TEM. Parameters such as precursor concentration, temperature, and reaction time could also be carefully monitored to assess their effect on the resulting crystal phase, orientation, and morphology.

Preliminary mineralization experiments on intact, demineralized, and demineralized/deproteinated dactyl club samples have been conducted to examine nucleation and growth. A double diffusion technique was used to observe heterogeneous nucleation of calcium phosphate on the various treated and untreated surfaces of dactyl club. A sagittal cross-section of the dactyl club was first obtained and polished down to 50 nm surface roughness. Three one-millimeter-thick by one-millimeter-wide regions of the section, containing both impact and periodic regions, were cut for the crystallization study. Two specimens were demineralized in 0.5 M ethylenediaminetetraacetic acid, replaced twice daily, for 48 hours. One of the demineralized samples underwent further treatment:

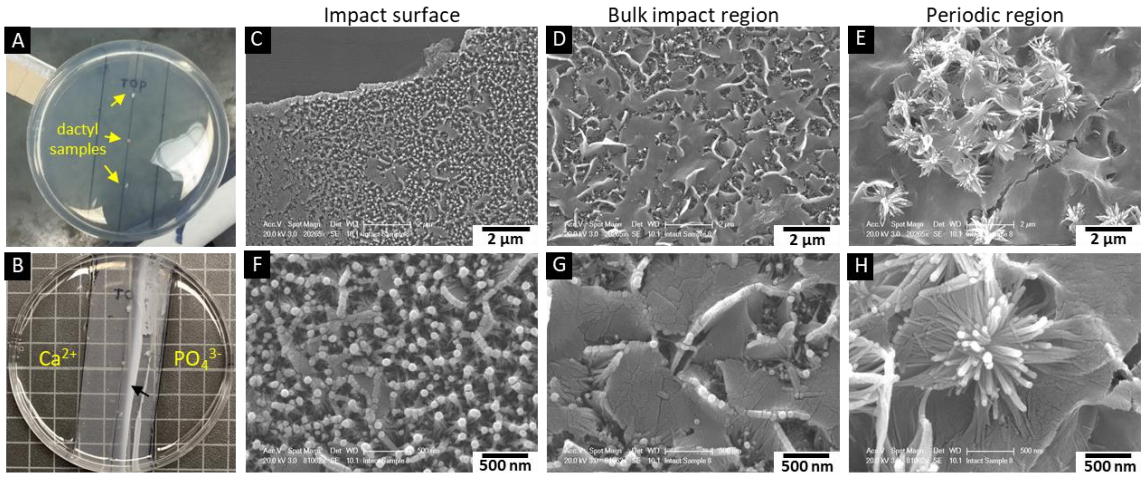

Figure 5.1. Preliminary biomineralization experiments on the dactyl. (A) Agarose gel containing demineralized as well as intact sections of the dactyl club. (B) Four days following double diffusion of calcium and phosphate precursor solutions into the agar gel. Black arrow corresponds to precipitation of calcium and phosphate precursors. (C, F) Low magnification (C) and high magnification (F) SEM micrographs of the impact surface region following heterogeneous double diffusion crystallization experiment showing particle-like morphology of crystals on the surface. (D, G) Low magnification (D) and high magnification (G) SEM micrographs of the bulk impact region showing plate-like crystal growth. (E, H) Low magnification (E) and high magnification (H) SEM micrographs of the periodic region showing spherulitic growth of crystals at the surface.

deproteination in 1 M sodium hydroxide for 24 hours. The third sample did not undergo any treatment. Each of the three samples were then rinsed 3 times in fresh Milli-Q water. The dactyl specimens were then embedded in Agarose gel (1 wt%) (Figure 5.1 A).

Wells to contain precursor solution for double diffusion were prepared by cutting away the Agarose gel on either side of the petri dish, equidistant from the dactyl samples, using a razor blade. This created a 3 cm path length for double diffusion to occur. Precursor solutions of 100 mM calcium chloride and 60 mM sodium dihydrogen phosphate (pH 7.4) were poured into either side of the well and left to react at room temperature. After 4 days, a white crystallization front was observed within the gel covering the dactyl specimens (Figure 5.1 B). The gel was then dissolved from the dactyl specimens by washing in QG buffer. Dactyl specimens were subsequently washed in fresh Milli-Q water 3-5 times, dried on filter paper, and then mounted on a carbon tape-coated aluminum stub for SEM observation.

SEM was then performed on the dactyl surfaces to determine if any new mineral had formed and characterize the morphology of new crystals. First examining the intact, non-treated club specimen, low magnification SEM immediately revealed that new crystals had nucleated, with apparent coverage across the entire surface of the sample. High magnification imaging was used to characterize the mineral within different regions of the club. Interestingly, the nucleated crystals appear to take on different morphologies within each of the surface, bulk impact, and periodic regions. Although crystallization did not appear to occur all the way through to the club surface, a film of crystals with apparent nanoparticle morphology was observed within areas approximately 20-50 μm from the

surface, but still within the impact surface region (Figure 5.1 C, F). In some areas, the particles appear to have aggregated or assembled forming rod-like or fibrous structures (Figure 5.1 F). Within the bulk of the impact region, we observe a film with plate-like as well as some nanoparticulate morphology (Figures 5.1 D, G). Finally, spherulitic, needle-like crystals are observed within the periodic region, with the highest concentration of these particles existing within the inner-most areas of the periodic region, furthest away from the club surface (Figures 5.1 E, H). EDS spectra, acquired in each area, showed the presence of calcium and phosphorus; however, since the club was untreated and fully mineralized prior to doing the crystallization experiment, we are unable to distinguish elemental contribution of the newly for crystals from the native mineral. XRD as well as TEM characterization will need to be done in the future to determine the composition and crystal structure of the nucleated crystals. SEM was then performed on the demineralized as well as demineralized and deproteinated dactyl specimens. Interestingly, both the demineralized and demineralized/deproteinated surfaces show little-no newly formed crystals (data not shown here). Examination of the impact region, impact surface, and periodic regions show nearly no new mineral. In addition, EDS point spectra obtain from different areas of both samples show no calcium or phosphorus, only carbon, nitrogen, and oxygen. This is important because it suggest that proteins and/or other organics play a key role in controlling and facilitating biomineralization of the dactyl club. The results also suggest that our demineralization procedure may be removing proteins and peptides associated with organic matrix. Otherwise, I suspect that we would observe new mineral forming in the demineralized sample, assuming only mineral was removed from the tissue.

5.4 Perspectives and outlook on biomimetic materials synthesis

The field of biomimetic engineering has been fruitful over the past decade. Numerous synthetic biomimetic structures that have been able to achieve microstructural, nanostructural, and crystallographic control with features that are nearly indistinguishable from the natural systems. By designing these materials with well-defined micro- and nanostructures, as well as incorporating engineering materials such as alumina ceramic and extensible polymers as constituent building blocks, the resultant composite materials have the potential to exceed the mechanical properties of the native biological composite.

The arthropod cuticle has recently become a biological material of biomimetic interest for structural applications. Great progress has been made in mimicking its helicoidal structure and achieving the fracture-tolerant properties that this structure affords. Biomimetic helicoidal carbon fiber/epoxy composites fabricated using modern prepreg materials and industrial processing techniques have already demonstrated the ability to surpass the performance of current aerospace and automotive design standards under impact loading.

Fiber-reinforced composite processing is advantageous in that it allows for the production of large-scale bulk materials that exhibit an adequate combination of strength and toughness; however, the process of mimicking the helicoidal architecture within the arthropod cuticle requires labor- and time-intensive processing. With the help of current technology, the cutting, alignment, and stacking of fiber layers (plies) could be automated to reduce processing time and the possibility of human induced error, such as ply misalignment. This suggests the need for new assembly methods. The cuticle-mimetic

structures produced by the cholesteric self-assembly of nanocrystalline materials achieve highly controlled micro- and nanostructure reminiscent of natural cuticle and could provide means to scalable production (89; 90; 179; 180).

In addition, most commercial prepreg materials are expensive and only feature reinforcements with fiber diameters on the microscale, therefore demonstrating a need for alternative materials and for a reduction in size, which will reduce weight. Chitin fibers within most arthropod cuticle have diameters on the order of tens of nanometers. Thus, to achieve a mimetic structure that is more representative of the natural system, there is a current demand for a 100– 1,000-fold reduction in the diameter of commercially available fiber prepregs. Electrospinning is a popular current technique to produce nanofibers; however, achieving a high degree of fiber alignment, orientation, and packing density while incorporating a laminated helicoidal architecture remains a challenge. In addition, the tensile strength of fibers that are synthesized using electrospinning falls short of the strength of fibers synthesized using current high-temperature processing. Addressing this by looking at methods by which nature produces its fibers may yield new insights into processing strong fibers.

Another challenge in mimicking arthropod cuticle is incorporating pore canal tubule fibers. It has been well established in natural systems that interpenetrating pore canal tubule fibers provide enhanced out-of-plane properties such as tensile and compressive strength. Few biomimetic reports have successfully incorporated these tubule structures into helicoidal architected materials. Z-pinning, which involves inserting reinforcing fibers

through the thickness (in the z-direction) of the composite laminate, is one potentially successful option for incorporating these structural features (151; 181).

There are many widespread challenges across the field of biomimetics, including lack of control of micro- and nanostructural features and interfaces across large areas and lack of manufacturing speed and scalability. For example, in order to scale up, well-defined micro- and nano-architectures need to be maintained and uniform across the entire volume of the part to avoid localized defects and to provide predictable function. Rapid processing methods for these materials need to be addressed. Many of the current methods, such as layer-by-layer techniques, are time-consuming and labor-intensive. 3D printing methods continue to push this boundary, but length scale is still an issue. Moreover, control over the interfacial properties is a major challenge. Many biological materials control the strength of hard–soft interfaces through smooth compositional and mechanical gradients, which reduce stress concentration and delamination. Incorporating mechanical gradients into biomimetic materials will be beneficial for many structural applications.

Finally, more attention needs to be paid to taking advantage of the multifunctional nature of many biological systems, which not only are mechanically robust, but also incorporate aspects such as self-healing, nutrient transport, and actuation/shape-change. If these aspects can be appropriately addressed, the next generation of high-performance multifunctional materials will certainly be inspired by biology.

References

1. Yaraghi NA, Guarin-Zapata N, Grunenfelder LK, Hintsala E, Bhowmick S, et al. 2016. A Sinusoidally Architected Helicoidal Biocomposite. *Adv Mater* 28:6835-44

2. Yaraghi NA, Kisailus D. 2018. Biomimetic Structural Materials: Inspiration from Design and Assembly. *Annu Rev Phys Chem* 69:23-57

3. Ritchie RO. 2011. The conflicts between strength and toughness. *Nat Mater* 10:817-22

4. Boeing. 2018. *787 Dreamliner by Design*. https://www.boeing.com/commercial/787/by-design/#/featured

5. Autoevolution. 2013. *BMW i3 Might Be Cheaper to Live with Due to Carbon Fiber Construction*. https://www.autoevolution.com/news/bmw-i3-might-be-cheaper-to-live-with-due-to-carbon-fiber-construction-73054.html#

6. Elon M. 2018. Making Life Multi-Planetary. *New Space* 6:2-11

7. Mitchell R. 2014. *Brembo Brake Disc Failures Have Happened To Other Teams and Mercedes In Pre-Season Testing* http://f1weekends.com/brembo-brake-disc-failures-have-happened-to-other-teams-and-mercedes-in-pre-season-testing/

8. GEAviation. 2018. *GE9X Commercial Aircraft Engine*. https://www.geaviation.com/commercial/engines/ge9x-commercial-aircraft-engine

9. Holmes M. 2014. Global carbon fibre market remains on upward trend. *Reinforced Plastics* 58:38-45

10. Dunlop JWC, Fratzl P. 2010. Biological Composites. *Annual Review of Materials Research* 40:1-24

11. Patek SN, Caldwell RL. 2005. Extreme impact and cavitation forces of a biological hammer: strike forces of the peacock mantis shrimp Odontodactylus scyllarus. *J Exp Biol* 208:3655-64

12. Green PA, Patek SN. 2015. Contests with deadly weapons: telson sparring in mantis shrimp (Stomatopoda). *Biol Lett* 11:20150558

13. Milliron G. 2012. Lightweight Impact-Resistant Composite Materials: Lessons from Mantis Shrimp.

14. Weaver JC, Milliron GW, Miserez A, Evans-Lutterodt K, Herrera S, et al. 2012. The stomatopod dactyl club: a formidable damage-tolerant biological hammer. *Science* 336:1275-80

15. Roco MC. 2011. The long view of nanotechnology development: the National Nanotechnology Initiative at 10 years. *Journal of Nanoparticle Research* 13:427-45

16. Holdren JP. 2011. Materials genome initiative for global competitiveness. *National Science and Technology Council OSTP. Washington, USA*

17. Wegst UG, Bai H, Saiz E, Tomsia AP, Ritchie RO. 2015. Bioinspired structural materials. *Nat Mater* 14:23-36

18. Mayyas A, Omar M, Hayajneh M, Mayyas AR. 2017. Vehicle's lightweight design vs. electrification from life cycle assessment perspective. *Journal of Cleaner Production* 167:687-701

19. Kim HJ, Keoleian GA, Skerlos SJ. 2011. Economic Assessment of Greenhouse Gas Emissions Reduction by Vehicle Lightweighting Using Aluminum and High-Strength Steel. *Journal of Industrial Ecology* 15:64-80

20. Fink BK. 2000. Performance metrics for composite integral armor. *Journal of thermoplastic composite materials* 13:417-31

21. David NV, Gao XL, Zheng JQ. 2009. Ballistic Resistant Body Armor: Contemporary and Prospective Materials and Related Protection Mechanisms. *Applied Mechanics Reviews* 62:050802--20

22. Mukasey M, Sedgwick J, Hagy D. 2008. Ballistic Resistance of Body Armor, NIJ Standard-0101.06. *US Department of Justice (www. ojp. usdoj. gov/nij)*

23. BMW. 2018. *The BMW i3 and All-New BMW i3s*. https://www.bmwusa.com/vehicles/bmwi/bmw-i3.html

24. Brembo. 2018. *F1 Infographics*. http://www.brembo.com/en/car/formula-1/f1-infographics

25. Heuss R, Müller N, van Sintern W, Starke A, Tschiesner A. 2012. Lightweight, heavy impact. *Hg. v. McKinsey. McKinsey*

26. Zoltek. 2018. *How is Carbon Fiber Made?* http://zoltek.com/carbon-fiber/how-is-carbon-fiber-made/

27. Edie DD. 1998. The effect of processing on the structure and properties of carbon fibers. *Carbon* 36:345-62

28. Naleway SE, Porter MM, McKittrick J, Meyers MA. 2015. Structural Design Elements in Biological Materials: Application to Bioinspiration. *Advanced Materials* 27:5455-76

29. Meyers MA, McKittrick J, Chen P-Y. 2013. Structural Biological Materials: Critical Mechanics-Materials Connections. *Science* 339:773-9

30. Chen P-Y, McKittrick J, Meyers MA. 2012. Biological materials: Functional adaptations and bioinspired designs. *Progress in Materials Science* 57:1492-704

31. Meyers MA, Chen P-Y, Lin AY-M, Seki Y. 2008. Biological materials: Structure and mechanical properties. *Progress in Materials Science* 53:1-206

32. Fratzl P, Weinkamer R. 2007. Nature's hierarchical materials. *Progress in Materials Science* 52:1263-334

33. Jackson AP, Vincent JFV, Turner RM. 1988. The Mechanical Design of Nacre. *Proceedings of the Royal Society Series B-Biological Sciences* 234:415-+

34. Currey JD, Taylor JD. 1974. The mechanical behaviour of some molluscan hard tissues. *Journal of Zoology* 173:395-406

35. Song F, Soh AK, Bai YL. 2003. Structural and mechanical properties of the organic matrix layers of nacre. *Biomaterials* 24:3623-31

36. Wang RZ, Suo Z, Evans AG, Yao N, Aksay IA. 2001. Deformation mechanisms in nacre. *Journal of Materials Research* 16:2485-93

37. Wang RZ, Wen HB, Cui FZ, Zhang HB, Li HD. 1995. Observations of damage morphologies in nacre during deformation and fracture. *J. Mater. Sci.* 30:2299-304

38. Meyers MA, Lin AY, Chen PY, Muyco J. 2008. Mechanical strength of abalone nacre: role of the soft organic layer. *J Mech Behav Biomed Mater* 1:76-85

39. Barthelat F, Espinosa HD. 2007. An Experimental Investigation of Deformation and Fracture of Nacre–Mother of Pearl. *Experimental Mechanics* 47:311-24

40. Wang R, Gupta HS. 2011. Deformation and Fracture Mechanisms of Bone and Nacre. *Annual Review of Materials Research* 41:41-73

41. Espinosa HD, Juster AL, Latourte FJ, Loh OY, Gregoire D, Zavattieri PD. 2011. Tablet-level origin of toughening in abalone shells and translation to synthetic composite materials. *Nature Communications* 2:173-

42. Barthelat F, Li C-M, Comi C, Espinosa HD. 2006. Mechanical properties of nacre constituents and their impact on mechanical performance. *Journal of Materials Research* 21:1977-86

43. Sarikaya M, Gunnison K, Yasrebi M, Aksay I. Mechanical property-microstructural relationships in abalone shell. *Proc. MRS proceedings, 1989*, 174:109: Cambridge Univ Press

44. Jackson A, Vincent J, Turner R. 1990. Comparison of nacre with other ceramic composites. *J. Mater. Sci.* 25:3173-8

45. Barthelat F, Li C-M, Comi C, Espinosa HD. 2011. Mechanical properties of nacre constituents and their impact on mechanical performance. *Journal of Materials Research* 21:1977-86

46. Hendley CTI, Tao J, Kunitake JAMR, De Yoreo JJ, Estroff LA. 2015. Microscopy techniques for investigating the control of organic constituents on biomineralization. *MRS Bulletin* 40:480-9

47. Rao A, Cölfen H. 2016. Mineralization and non-ideality: on nature's foundry. *Biophysical Reviews* 8:309-29

48. Ehrlich H. 2010. Chitin and collagen as universal and alternative templates in biomineralization. *International Geology Review* 52:661-99

49. Addadi L, Weiner S. 1985. Interactions between acidic proteins and crystals: stereochemical requirements in biomineralization. *Proceedings of the National Academy of Sciences* 82:4110-4

50. Belcher AM, Wu XH, Christensen RJ, Hansma PK, Stucky GD, Morse DE. 1996. Control of crystal phase switching and orientation by soluble mollusc-shell proteins. *Nature* 381:56-8

51. Weiner S, Addadi L. 2011. Crystallization Pathways in Biomineralization. *Annual Review of Materials Research* 41:21-40

52. Lawson MA, Xia Z, Barnett BL, Triffitt JT, Phipps RJ, et al. 2010. Differences between bisphosphonates in binding affinities for hydroxyapatite. *J Biomed Mater Res B Appl Biomater* 92:149-55

53. Gower LB. 2008. Biomimetic Model Systems for Investigating the Amorphous Precursor Pathway and Its Role in Biomineralization. *Chem. Rev.* 108:4551-627

54. Addadi L, Weiner S. 1992. Control and Design Principles in Biological Mineralization. *Angewandte Chemie International Edition in English* 31:153-69

55. Aizenberg J, Hanson J, Koetzle TF, Weiner S, Addadi L. 1997. Control of Macromolecule Distribution within Synthetic and Biogenic Single Calcite Crystals. *Journal of the American Chemical Society* 119:881-6

56. George A, Sabsay B, Simonian PA, Veis A. 1993. Characterization of a novel dentin matrix acidic phosphoprotein. Implications for induction of biomineralization. *Journal of Biological Chemistry* 268:12624-30

57. Levi Y, Albeck S, Brack A, Weiner S, Addadi L. 1998. Control Over Aragonite Crystal Nucleation and Growth: An In Vitro Study of Biomineralization. *Chemistry – A European Journal* 4:389-96

58. Weiner S, Traub W, Parker SB. 1984. Macromolecules in Mollusc Shells and Their Functions in Biomineralization [and Discussion]. *Philosophical Transactions of the Royal Society of London. B, Biological Sciences* 304:425-34

59. Gajjeraman S, Narayanan K, Hao J, Qin C, George A. 2007. Matrix Macromolecules in Hard Tissues Control the Nucleation and Hierarchical Assembly of Hydroxyapatite. *Journal of Biological Chemistry* 282:1193-204

60. Tavafoghi M, Cerruti M. 2016. The role of amino acids in hydroxyapatite mineralization. *Journal of The Royal Society Interface* 13

61. Ibsen CJS, Gebauer D, Birkedal H. 2016. Osteopontin Stabilizes Metastable States Prior to Nucleation during Apatite Formation. *Chemistry of Materials* 28:8550-5

62. Nudelman F, Gotliv BA, Addadi L, Weiner S. 2006. Mollusk shell formation: mapping the distribution of organic matrix components underlying a single aragonitic tablet in nacre. *Journal of Structural Biology* 153:176-87

63. Lin AY-M, Chen P-Y, Meyers MA. 2008. The growth of nacre in the abalone shell. *Acta Biomaterialia* 4:131-8

64. Cartwright JH, Checa AG. 2007. The dynamics of nacre self-assembly. *Journal of the Royal Society Interface* 4:491-504

65. Addadi L, Joester D, Nudelman F, Weiner S. 2006. Mollusk Shell Formation: A Source of New Concepts for Understanding Biomineralization Processes. *Chemistry – A European Journal* 12:980-7

66. Heinemann F, Launspach M, Gries K, Fritz M. 2011. Gastropod nacre: Structure, properties and growth — Biological, chemical and physical basics. *Biophysical Chemistry* 153:126-53

67. Nudelman F. 2015. Nacre biomineralisation: A review on the mechanisms of crystal nucleation. *Semin Cell Dev Biol* 46:2-10

68. Xia Z. 2016. Biomineralization and Biomimetic Materials Processing. In *Biomimetic Principles and Design of Advanced Engineering Materials*:271-97: John Wiley & Sons, Ltd. Number of 271-97 pp.

69. Zan G, Wu Q. 2016. Biomimetic and Bioinspired Synthesis of Nanomaterials/Nanostructures. *Adv Mater* 28:2099-147

70. Grunenfelder LK, Herrera S, Kisailus D. 2014. Crustacean-Derived Biomimetic Components and Nanostructured Composites. *Small* 10:3207-32

71. Kisailus D, Choi JH, Weaver JC, Yang W, Morse DE. 2005. Enzymatic synthesis and nanostructural control of gallium oxide at low temperature. *Advanced Materials* 17:314-8

72. Johnson JM, Kinsinger N, Sun C, Li D, Kisailus D. 2012. Urease-mediated room-temperature synthesis of nanocrystalline titanium dioxide. *Journal of the American Chemical Society* 134:13974-7

73. Kisailus D, Najarian M, Weaver JC, Morse DE. 2005. Functionalized Gold Nanoparticles Mimic Catalytic Activity of a Polysiloxane-Synthesizing Enzyme. *Advanced Materials* 17:1234-9

74. Kisailus D, Truong Q, Amemiya Y, Weaver JC, Morse DE. 2006. Self-assembled bifunctional surface mimics an enzymatic and templating protein for the synthesis of a metal oxide semiconductor. *Proceedings of the National Academy of Sciences* 103:5652-7

75. Yu K, Fan T, Lou S, Zhang D. 2013. Biomimetic optical materials: Integration of nature's design for manipulation of light. *Progress in Materials Science* 58:825-73

76. Finnemore A, Cunha P, Shean T, Vignolini S, Guldin S, et al. 2012. Biomimetic layer-by-layer assembly of artificial nacre. *Nature Communications* 3:966

77. Xu M, Gratson GM, Duoss EB, Shepherd RF, Lewis JA. 2006. Biomimetic silicification of 3D polyamine-rich scaffolds assembled by direct ink writing. *Soft Matter* 2:205-9

78. Chen J, Huang Y, Su M, Cheng K, Zhao Y. 2016. Biomimetic synthesis of oriented aragonite crystals and nacre-like composite material by controlling the fluid type. *Powder Technology* 302:455-61

79. Sydney Gladman A, Matsumoto EA, Nuzzo RG, Mahadevan L, Lewis JA. 2016. Biomimetic 4D printing. *Nat Mater* 15:413-8

80. Heidebrecht A, Eisoldt L, Diehl J, Schmidt A, Geffers M, et al. 2015. Biomimetic Fibers Made of Recombinant Spidroins with the Same Toughness as Natural Spider Silk. *Advanced Materials* 27:2189-94

81. Wang J, Qiao J, Wang J, Zhu Y, Jiang L. 2015. Bioinspired Hierarchical Alumina–Graphene Oxide–Poly(vinyl alcohol) Artificial Nacre with Optimized Strength and Toughness. *ACS Applied Materials & Interfaces* 7:9281-6

82. Deville S. 2008. Freeze-Casting of Porous Ceramics: A Review of Current Achievements and Issues. *Advanced Engineering Materials* 10:155-69

83. Martin JJ, Fiore BE, Erb RM. 2015. Designing bioinspired composite reinforcement architectures via 3D magnetic printing. *Nat Commun* 6

84. Wang J, Cheng Q, Tang Z. 2012. Layered nanocomposites inspired by the structure and mechanical properties of nacre. *Chemical Society Reviews* 41:1111-29

85. Bouville F, Maire E, Meille S, Van de Moortèle B, Stevenson AJ, Deville S. 2014. Strong, tough and stiff bioinspired ceramics from brittle constituents. *Nat Mater* 13:508-14

86. Dwivedi G, Flynn K, Resnick M, Sampath S, Gouldstone A. 2015. Bioinspired Hybrid Materials from Spray-Formed Ceramic Templates. *Advanced Materials* 27:3073-8

87. Le Ferrand H, Bouville F, Niebel TP, Studart AR. 2015. Magnetically assisted slip casting of bioinspired heterogeneous composites. *Nature materials* 14:1172-9

88. Grunenfelder LK, Suksangpanya N, Salinas C, Milliron G, Yaraghi N, et al. 2014. Bio-inspired impact-resistant composites. *Acta Biomaterialia* 10:3997-4008

89. Wang B, Walther A. 2015. Self-Assembled, Iridescent, Crustacean-Mimetic Nanocomposites with Tailored Periodicity and Layered Cuticular Structure. *ACS Nano* 9:10637-46

90. Matsumura S, Kajiyama S, Nishimura T, Kato T. 2015. Formation of Helically Structured Chitin/CaCO3 Hybrids through an Approach Inspired by the Biomineralization Processes of Crustacean Cuticles. *Small* 11:5127-33

91. Deville S, Saiz E, Nalla RK, Tomsia AP. 2006. Freezing as a path to build complex composites. *Science* 311:515-8

92. Jung JY, Naleway SE, Yaraghi NA, Herrera S, Sherman VR, et al. 2016. Structural analysis of the tongue and hyoid apparatus in a woodpecker. *Acta Biomater* 37:1-13

93. Tombolato L, Novitskaya EE, Chen PY, Sheppard FA, McKittrick J. 2010. Microstructure, elastic properties and deformation mechanisms of horn keratin. *Acta Biomater* 6:319-30

94. Li BW, Zhao HP, Feng XQ, Guo WW, Shan SC. 2010. Experimental study on the mechanical properties of the horn sheaths from cattle. *J Exp Biol* 213:479-86

95. Kitchener A. 1988. An Analysis of the Forces of Fighting of the Blackbuck (Antilope-Cervicapra) and the Bighorn Sheep (Ovis-Canadensis) and the Mechanical Design of the Horns of Bovids. *Journal of Zoology* 214:1-20

96. Kasapi MA, Gosline JM. 1997. Design complexity and fracture control in the equine hoof wall. *Journal of Experimental Biology* 200:1639-59

97. Caldwell RL, Dingle H. 1975. Ecology and Evolution of Agonistic Behavior in Stomatopods. *Naturwissenschaften* 62:214-22

98. Caldwell RL. 1979. Cavity Occupation and Defensive Behavior in the Stomatopod Gonodactylus-Festai - Evidence for Chemically Mediated Individual Recognition. *Animal Behaviour* 27:194-201

99. Taylor JR, Patek SN. 2010. Ritualized fighting and biological armor: the impact mechanics of the mantis shrimp's telson. *J Exp Biol* 213:3496-504

100. Patek SN, Korff WL, Caldwell RL. 2004. Biomechanics: deadly strike mechanism of a mantis shrimp. *Nature* 428:819-20

101. Addadi L, Gal A, Faivre D, Scheffel A, Weiner S. 2015. Control of Biogenic Nanocrystal Formation in Biomineralization. *Israel Journal of Chemistry*:n/a-n/a

102. Currey JD, Nash A, Bonfield W. 1982. Calcified Cuticle in the Stomatopod Smashing Limb. *J. Mater. Sci.* 17:1939-44

103. Suksangpanya N, Yaraghi NA, Kisailus D, Zavattieri P. 2017. Twisting cracks in Bouligand structures. *J Mech Behav Biomed Mater* 76:38-57

104. Guarin-Zapata N, Gomez J, Yaraghi N, Kisailus D, Zavattieri PD. 2015. Shear wave filtering in naturally-occurring Bouligand structures. *Acta Biomater* 23:11-20

105. Amini S, Masic A, Bertinetti L, Teguh JS, Herrin JS, et al. 2014. Textured fluorapatite bonded to calcium sulphate strengthen stomatopod raptorial appendages. *Nat Commun* 5:3187

106. Amini S, Tadayon M, Idapalapati S, Miserez A. 2015. The role of quasi-plasticity in the extreme contact damage tolerance of the stomatopod dactyl club. *Nat Mater* 14:943-50

107. Romano P, Fabritius H, Raabe D. 2007. The exoskeleton of the lobster Homarus americanus as an example of a smart anisotropic biological material. *Acta Biomater* 3:301-9

108. Bouligand Y. 1972. Twisted fibrous arrangements in biological materials and cholesteric mesophases. *Tissue Cell* 4:189-217

109. Sachs C, Fabritius H, Raabe D. 2008. Influence of microstructure on deformation anisotropy of mineralized cuticle from the lobster Homarus americanus. *J Struct Biol* 161:120-32

110. Sachs C, Fabritius H, Raabe D. 2006. Hardness and elastic properties of dehydrated cuticle from the lobster Homarus americanus obtained by nanoindentation. *Journal of materials research* 21:1987-95

111. Wilts BD, Whitney HM, Glover BJ, Steiner U, Vignolini S. 2014. Natural Helicoidal Structures: Morphology, Self-assembly and Optical Properties. *Materials Today: Proceedings* 1:177-85

112. Oliver WC, Pharr GM. 2004. Measurement of hardness and elastic modulus by instrumented indentation: Advances in understanding and refinements to methodology. *Journal of Materials Research* 19:3-20

113. Moran K, Wuhrer R. 2006. X-Ray Mapping and Interpretation of Scatter Diagrams. *Microchimica Acta* 155:209-17

114. Abaqus A. 2012. Standard: user's manual version 6.12. *Simulia, USA*

115. Loste E, Wilson RM, Seshadri R, Meldrum FC. 2003. The role of magnesium in stabilising amorphous calcium carbonate and controlling calcite morphologies. *Journal of Crystal Growth* 254:206-18

116. Politi Y, Batchelor DR, Zaslansky P, Chmelka BF, Weaver JC, et al. 2009. Role of magnesium ion in the stabilization of biogenic amorphous calcium carbonate: A structure− function investigation. *Chemistry of Materials* 22:161-6

117. Chen PY, Lin AY, McKittrick J, Meyers MA. 2008. Structure and mechanical properties of crab exoskeletons. *Acta Biomater* 4:587-96

118. Compère P, Goffinet G. 1987. Elaboration and ultrastructural changes in the pore canal system of the mineralized cuticle of Carcinus maenas during the moulting cycle. *Tissue and Cell* 19:859-75

119. McKittrick J, Chen PY, Tombolato L, Novitskaya EE, Trim MW, et al. 2010. Energy absorbent natural materials and bioinspired design strategies: A review. *Mat Sci Eng C-Mater* 30:331-42

120. Zimmermann EA, Ritchie RO. 2015. Bone as a Structural Material. *Advanced Healthcare Materials* 4:1287-304

121. Viswanath B, Raghavan R, Ramamurty U, Ravishankar N. 2007. Mechanical properties and anisotropy in hydroxyapatite single crystals. *Scripta Materialia* 57:361-4

122. Fabritius H, Sachs C, Raabe D, Nikolov S, Friák M, Neugebauer J. 2011. Chitin in the Exoskeletons of Arthropoda: From Ancient Design to Novel Materials Science. In *Chitin*, ed. NS Gupta, 34:35-60: Springer Netherlands. Number of 35-60 pp.

123. Weiner S, Traub W, Wagner HD. 1999. Lamellar Bone: Structure–Function Relations. *Journal of Structural Biology* 126:241-55

124. Wagermaier W, Gupta HS, Gourrier A, Burghammer M, Roschger P, Fratzl P. 2006. Spiral twisting of fiber orientation inside bone lamellae. *Biointerphases* 1:1

125. Lichtenegger H, Muller M, Paris O, Riekel C, Fratzl P. 1999. Imaging of the helical arrangement of cellulose fibrils in wood by synchrotron X-ray microdiffraction. *Journal of Applied Crystallography* 32:1127-33

126. Zimmermann EA, Gludovatz B, Schaible E, Dave NK, Yang W, et al. 2013. Mechanical adaptability of the Bouligand-type structure in natural dermal armour. *Nat Commun* 4:2634

127. Fratzl P, Gupta HS, Fischer FD, Kolednik O. 2007. Hindered Crack Propagation in Materials with Periodically Varying Young's Modulus—Lessons from Biological Materials. *Advanced Materials* 19:2657-61

128. Kolednik O, Predan J, Fischer FD, Fratzl P. 2011. Bioinspired Design Criteria for Damage-Resistant Materials with Periodically Varying Microstructure. *Advanced Functional Materials* 21:3634-41

129. Ming-Yuan H, Hutchinson JW. 1989. Crack deflection at an interface between dissimilar elastic materials. *International Journal of Solids and Structures* 25:1053-67

130. Ritchie RO, Kinney JH, Kruzic JJ, Nalla RK. 2005. A fracture mechanics and mechanistic approach to the failure of cortical bone. *Fatigue & Fracture of Engineering Materials & Structures* 28:345-71

131. Zavattieri PD, Hector LG, Bower AF. 2007. Determination of the effective mode-I toughness of a sinusoidal interface between two elastic solids. *International Journal of Fracture* 145:167-80

132. Cordisco FA, Zavattieri PD, Hector LG, Carlson BE. 2016. Mode I fracture along adhesively bonded sinusoidal interfaces. *International Journal of Solids and Structures* 83:45-64

133. Grunenfelder LK, de Obaldia EE, Wang Q, Li D, Weden B, et al. 2014. Stress and Damage Mitigation from Oriented Nanostructures within the Radular Teeth ofCryptochiton stelleri. *Advanced Functional Materials* 24:6093-104

134. Hsieh TH, Kinloch AJ, Masania K, Taylor AC, Sprenger S. 2010. The mechanisms and mechanics of the toughening of epoxy polymers modified with silica nanoparticles. *Polymer* 51:6284-94

135. Johnsen B, Kinloch A, Mohammed R, Taylor A, Sprenger S. 2007. Toughening mechanisms of nanoparticle-modified epoxy polymers. *Polymer* 48:530-41

136. Dittanet P, Pearson RA. 2012. Effect of silica nanoparticle size on toughening mechanisms of filled epoxy. *Polymer* 53:1890-905

137. Dvorak GJ. 2013. Tensor Component and Matrix Notations. In *Micromechanics of Composite Materials*:1-9: Springer. Number of 1-9 pp.

138. Ahyong ST. 2016. Results of the Comprehensive Marine Biodiversity Survey International Workshops 2012 and 2013: Stomatopod Crustacea. *Raffles B Zool*:455-69

139. Heitler WJ, Fraser K, Ferrero EA. 2000. Escape behaviour in the stomatopod crustacean Squilla mantis, and the evolution of the caridoid escape reaction. *J Exp Biol* 203:183-92

140. Dahl E. 1983. Malacostracan phylogeny and evolution. *Crustacean Phylogeny. Crustacean*:189-212

141. Hessler RR. 1983. A defense of the caridoid facies; wherein the early evolution of the Eumalacostraca is discussed. *Crustacean issues* 1:145-64

142. Zhang Y, Paris O, Terrill NJ, Gupta HS. 2016. Uncovering three-dimensional gradients in fibrillar orientation in an impact-resistant biological armour. *Sci Rep* 6:26249

143. Raabe D, Sachs C, Romano P. 2005. The crustacean exoskeleton as an example of a structurally and mechanically graded biological nanocomposite material. *Acta Materialia* 53:4281-92

144. Paris O, Hartmann MA, Fritz-Popovski G. 2013. CHAPTER 8 The Mineralized Crustacean Cuticle: Hierarchical Structure and Mechanical Properties. In *Materials Design Inspired by Nature: Function Through Inner Architecture*:180-96: The Royal Society of Chemistry. Number of 180-96 pp.

145. Bentov S, Abehsera S, Sagi A. 2016. The Mineralized Exoskeletons of Crustaceans. In *Extracellular Composite Matrices in Arthropods*:137-63: Springer. Number of 137-63 pp.

146. Launey ME, Buehler MJ, Ritchie RO. 2010. On the Mechanistic Origins of Toughness in Bone. In *Annual Review of Materials Research, Vol 40*, ed. DR Clarke, M Ruhle, F Zok, 40:25-53. Palo Alto: Annual Reviews. Number of 25-53 pp.

147. Dayyani I, Shaw AD, Flores ELS, Friswell MI. 2015. The mechanics of composite corrugated structures: A review with applications in morphing aircraft. *Composite Structures* 133:358-80

148. Weinkamer R, Fratzl P. 2011. Mechanical adaptation of biological materials — The examples of bone and wood. *Materials Science and Engineering: C* 31:1164-73

149. Nikolov S, Petrov M, Lymperakis L, Friak M, Sachs C, et al. 2010. Revealing the design principles of high-performance biological composites using ab initio and multiscale simulations: the example of lobster cuticle. *Adv Mater* 22:519-26

150. Gupta H, Stachewicz U, Wagermaier W, Roschger P, Wagner H, Fratzl P. 2006. Mechanical modulation at the lamellar level in osteonal bone. *Journal of materials research* 21:1913-21

151. Mouritz AP. 2007. Review of z-pinned composite laminates. *Composites Part A: Applied Science and Manufacturing* 38:2383-97

152. Cheng L, Thomas A, Glancey JL, Karlsson AM. 2011. Mechanical behavior of bio-inspired laminated composites. *Composites Part A: Applied Science and Manufacturing* 42:211-20

153. Zheng X, Lee H, Weisgraber TH, Shusteff M, DeOtte J, et al. 2014. Ultralight, ultrastiff mechanical metamaterials. *Science* 344:1373-7

154. Hardin JO, Ober TJ, Valentine AD, Lewis JA. 2015. Microfluidic Printheads for Multimaterial 3D Printing of Viscoelastic Inks. *Advanced Materials* 27:3279-84

155. Zhu C, Han TY, Duoss EB, Golobic AM, Kuntz JD, et al. 2015. Highly compressible 3D periodic graphene aerogel microlattices. *Nat Commun* 6:6962

156. Studart AR. 2016. Additive manufacturing of biologically-inspired materials. *Chemical Society Reviews* 45:359-76

157. Eckel ZC, Zhou C, Martin JH, Jacobsen AJ, Carter WB, Schaedler TA. 2016. Additive manufacturing of polymer-derived ceramics. *Science* 351:58-62

158. Qin Z, Compton BG, Lewis JA, Buehler MJ. 2015. Structural optimization of 3D-printed synthetic spider webs for high strength. *Nat Commun* 6

159. Wehner M, Truby RL, Fitzgerald DJ, Mosadegh B, Whitesides GM, et al. 2016. An integrated design and fabrication strategy for entirely soft, autonomous robots. *Nature* 536:451-5

160. Gratson GM, Xu M, Lewis JA. 2004. Microperiodic structures: Direct writing of three-dimensional webs. *Nature* 428:386-

161. Truby RL, Lewis JA. 2016. Printing soft matter in three dimensions. *Nature* 540:371-8

162. Lewis JA, Gratson GM. 2004. Direct writing in three dimensions. *Materials Today* 7:32-9

163. Michna S, Wu W, Lewis JA. 2005. Concentrated hydroxyapatite inks for direct-write assembly of 3-D periodic scaffolds. *Biomaterials* 26:5632-9

164. Guo SZ, Gosselin F, Guerin N, Lanouette AM, Heuzey MC, Therriault D. 2013. Solvent-Cast Three-Dimensional Printing of Multifunctional Microsystems. *Small* 9:4118-22

165. Guo S-Z, Heuzey M-C, Therriault D. 2014. Properties of Polylactide Inks for Solvent-Cast Printing of Three-Dimensional Freeform Microstructures. *Langmuir* 30:1142-50

166. Croisier F, Jérôme C. 2013. Chitosan-based biomaterials for tissue engineering. *European Polymer Journal* 49:780-92

167. Ang TH, Sultana FSA, Hutmacher DW, Wong YS, Fuh JYH, et al. 2002. Fabrication of 3D chitosan–hydroxyapatite scaffolds using a robotic dispensing system. *Materials Science and Engineering: C* 20:35-42

168. Almeida CR, Serra T, Oliveira MI, Planell JA, Barbosa MA, Navarro M. 2014. Impact of 3-D printed PLA-and chitosan-based scaffolds on human monocyte/macrophage responses: unraveling the effect of 3-D structures on inflammation. *Acta biomaterialia* 10:613-22

169. Apichattrabrut T, Ravi-Chandar K. 2006. Helicoidal composites. *Mechanics of Advanced Materials and Structures* 13:61-76

170. ASTM. D7136/D7136M. Standard Test Method for Measuring the Damage Resistance of a Fiber-Reinforced Polymer Matrix Composite to a Drop-Weight Impact Event.

171. ASTM. D7137/D7137M. Standard Test Method for Compressive Residual Strength Properties of Damaged Polymer Matrix Composite Plates.

172. Geng L, Feng W, Hutmacher DW, San Wong Y, Tong Loh H, Fuh JY. 2005. Direct writing of chitosan scaffolds using a robotic system. *Rapid Prototyping Journal* 11:90-7

173. Rao RB, Krafcik KL, Morales AM, Lewis JA. 2005. Microfabricated Deposition Nozzles for Direct-Write Assembly of Three-Dimensional Periodic Structures. *Advanced Materials* 17:289-93

174. Marion B, Bilge S, Martin S, Hartmut S. 1999. Novel Low-Temperature Processing Route of Dense Mullite Ceramics by Reaction Sintering of Amorphous SiO2-Coated γ-Al2O3 Particle Nanocomposites. *Journal of the American Ceramic Society* 82:1388-92

175. George A, Veis A. 2008. Phosphorylated Proteins and Control over Apatite Nucleation, Crystal Growth, and Inhibition. *Chem. Rev.* 108:4670-93

176. Roer R, Dillaman R. 1984. The structure and calcification of the crustacean cuticle. *American Zoologist* 24:893-909

177. Chockalingam S. 1971. Studies on enzymes associated with calcification of the cuticle of the hermit crab Clibanarius olivaceous. *Marine Biology* 10:169-82

178. Luquet G, Dauphin Y, Percot A, Salomé M, Ziegler A, et al. 2016. Calcium Deposits in the Crayfish, Cherax quadricarinatus: Microstructure Versus Elemental Distribution. *Microscopy and Microanalysis* 22:22-38

179. Shopsowitz KE, Qi H, Hamad WY, MacLachlan MJ. 2010. Free-standing mesoporous silica films with tunable chiral nematic structures. *Nature* 468:422-5

180. Majoinen J, Kontturi E, Ikkala O, Gray DG. 2012. SEM imaging of chiral nematic films cast from cellulose nanocrystal suspensions. *Cellulose* 19:1599-605

181. Ladani RB, Ravindran AR, Wu S, Pingkarawat K, Kinloch AJ, et al. 2016. Multi-scale toughening of fibre composites using carbon nanofibres and z-pins. *Composites Science and Technology* 131:98-109